Liquid Metal Embrittlement in Resistance Spot Welding: The Thermomechanical Origin and Embrittler Transport Mechanism

by

Christopher DiGiovanni

A thesis
presented to the University of Waterloo
in fulfillment of the
thesis requirement for the degree of
Doctor of Philosophy
in
Mechanical and Mechatronics Engineering

Waterloo, Ontario, Canada, 2021

Examining Committee Membership

The following served on the Examining Committee for this thesis. The decision of the Examining Committee is given by majority vote.

External Examiner:	Professor Jeff Wood Mechanical and Materials Engineering University of Western Ontario, Canada
Supervisor(s):	Professor Norman Y. Zhou and Professor Elliot Biro Mechanical and Mechatronics Engineering University of Waterloo, Canada
Internal Member:	Professor Adrian Gerlich, Mechanical and Mechatronics Engineering University of Waterloo, Canada
Internal Member:	Professor Kyle Daun Mechanical and Mechatronics Engineering University of Waterloo, Canada
Other Member(s):	Professor Robert Gracie Civil and Environmental Engineering University of Waterloo, Canada

Author's Declaration

This thesis consists of material all of which the candidate authored or co-authored: see Statement of Contributions included in the thesis. This is a true copy of the thesis, including any required final revisions, as accepted by my examiners.

I understand that my thesis may be made electronically available to the public

Statement of Contributions

This thesis consists of six chapters: introduction and literature review (Chapters 1 and 2) which represents original work and a published review paper that the candidate co-authored, and a series of three data chapters starting from Chapter 3 to 5 including published or under review manuscripts the candidate authored. The manuscripts have been modified to fit the style of the thesis. The candidate is the primary author of all data chapter manuscripts. The following co-authors have contributed to the current work as outlined below:

Professor Norman Zhou supervised the research progress, advised on research direction, reviewed manuscripts, and had technical discussions. Professor Elliot Biro oversaw research progress, reviewed manuscripts, and had technical discussions.

Dr. Frank Goodwin from the International Zinc Association (IZA), Durham, USA acted as an industrial supervisor, provided material, financial support, feedback on research direction and edited manuscripts.

Chapter 2

Razmpoosh MH, DiGiovanni C, Biro E, Zhou NY. *"Pathway to Understand Liquid Metal Embrittlement: From Fundamentals to Application"*. Prog. Mater. Sci. 2021 Published Online

The candidate is the secondary author of this published review paper. The candidate composed the following sections in the review paper: role of process parameters on LME, and the effects of LME on mechanical properties. Only sections composed by the candidate were include while the rest of the chapter represents original work. M. Hadi Razmpoosh composed the other sections of the review paper, which are excluded from Chapter 2. Prof. Zhou and Prof. Biro's role were as described above.

Chapter 3

DiGiovanni C, Biro E, Zhou NY. *"Impact of liquid metal embrittlement cracks on resistance spot weld static strength"*. Sci. Technol. Weld. 2019, 24(3) 218-224

The candidate carried out the experimental work, analysed the data and prepared the manuscript and all associated figures. The role of Prof. Zhou and Prof. Biro were as described above.

DiGiovanni C, Han X, Powell A, Biro E, Zhou NY. *"Experimental and Numerical Analysis of Liquid Metal Embrittlement Crack Location."* J. Mat. Eng. Perm. 2019 28(4):2045-2052.

The candidate carried out the experimental work, constructed the Abaqus model, analysed the data and prepared the manuscript and all associated figures. Xu Han completed the machining of the customized electrode used for welding. Adam Powell assisted in the mechanical testing. The role of Prof. Zhou and Prof. Biro's role were as described above.

Chapter 4

DiGiovanni C, Bag S, Mehling C, Choi KW, Macwan A, Biro E, Zhou NY. *"Reduction of liquid metal embrittlement cracking using weld current ramping".* Weld. World. 2019 63(6):1583-1591.

The candidate carried out the experimental work, analysed the data and prepared the manuscript and all associated figures. Prof. Swarup Bag completed the FEM model construction, which has been omitted from this thesis. Connor Mehling assisted in metallographic sample preparation. James Choi assisted in programming of the robotic welder for the ramp down current sample. Dr. Andrew Macwan provided revisions and edits to the manuscript. Prof. Zhou and Prof. Biro's role were as described above.

DiGiovanni C, He L, Pistek U, Goodwin F, Biro E, Zhou NY. *"Role of spot weld electrode geometry on liquid metal embrittlement crack development".* J. Manuf. Proc. 2020 49:1-9

The candidate carried out the experimental work, analysed the data, operated the ESI Sysweld simulation software, and prepared the manuscript and all associated figures. Josh (Liu) He assisted in developing the weld schedules. Urban Pistek assisted in metallographic sample preparation and LME crack measurements. Dr. Goodwin, Prof. Zhou and Prof. Biro's role were as described above

DiGiovanni C, Ghatei Kalashami A, Goodwin F, Biro E, Zhou NY. *"Occurrence of Sub-Critical Heat Affected Zone Liquid Metal Embrittlement in Joining of Advanced High Strength Steel".* J. Mater. Process. Tech. 2021 288:116917

The candidate carried out the experimental work, analysed the data and prepared the manuscript and all associated figures. Ali Ghatei Kalashami completed the EBSD analysis, which as been omitted from the thesis. Dr. Goodwin, Prof. Zhou, and Prof. Biro's role were as described above.

Chapter 5

DiGiovanni C, Ghatei Kalashami A, Biro E, Zhou NY. *"Liquid Metal Embrittlement Transport Mechanism in the Fe/Zn System: Stress-assisted Diffusion"*. Materialia. 2021 18:101153

The candidate carried out the experimental work, constructed the FDM numerical model, analysed the data and prepared the manuscript and all associated figures. Ali Ghatei Kalashami assisted in metallographic sample preparation. Prof. Zhou and Prof. Biro's role were as described above.

Abstract

To increase fuel economy, demand for lighter vehicles by way of thinner parts has risen in recent years. As parts become thinner the vehicle safety cannot be comprised, leading to the development of advanced high strength steels (AHSS) which exhibit excellent strength and ductility. AHSS are often coated with zinc (Zn) to prevent corrosion, however the coating can lead to several complications, such as liquid metal embrittlement (LME). Resistance spot welding (RSW), a common automotive process, has been observed to accentuate LME cracking. During RSW, the heat buildup at the weld surface is sufficient to melt the Zn coating, leading to LME. Presently, LME cracks that are detrimental to joint integrity are undefined and thus hard to target for mitigation. Furthermore, the exact sources of stress (a prerequisite for LME) during the RSW process leading to detrimental crack formation, remains unclear. Hence, a comprehensive understanding of LME occurrence calls for an in-depth analysis of the thermomechanical aspects of the RSW process and the fundamental mechanisms leading to the onset of LME.

This research aims to define, mitigate, and explain the occurrence of LME cracks during RSW. Lap shear static strength testing was used to determine the effect of LME cracks on joint performance. Detrimental cracks were defined according to their size and location. RSW process adjustments were carried out to mitigate detrimental LME cracks. It was determined that the mechanism of formation varies depending on the region the crack is located. Furthermore, it was found that the occurrence of LME in all cases was largely driven by the presence of stress. To isolate the effects of stress and temperature on the occurrence of LME, elevated temperature tensile testing was carried out using conditions that best replicate the RSW process. A co-dependence of temperature and stress for the onset of LME was observed, showing the temperature range for LME is not static as previously thought. Using interrupted testing, the onset of LME was observed in detail. Zn penetration to the AHSS grain boundaries was observed to increase with increasing applied stress until LME crack formation. A diffusion analysis revealed the fundamental LME transport mechanism to be stress-assisted grain boundary diffusion. This mechanism reconciles the observations of LME in RSW, which showed the occurrence of LME to be highly dependent on both temperature and stress.

Keywords: Liquid Metal Embrittlement; Resistance Spot Welding; Thermomechanical Processing; Diffusion; Advanced High Strength Steel

Acknowledgements

First, I would like to acknowledge and express my appreciation to my supervisors Prof. Norman Y. Zhou and Prof. Elliot Biro. I would like to thank Prof. Zhou for providing me the freedom to pursue my research interests and cultivating my curiosity. In addition to his academic supervision, he also gave me the opportunity to grow my leadership skills and learn to interface with industrial partners. On numerous occasions Prof. Zhou and I met to discuss the research direction and management of our spot welding group. I always felt inspired leaving his office and was eager to return to the lab to push the boundaries of our field. I would like to thank Prof. Biro for the in-depth technical discussions during our meetings and for teaching me the value of asking detailed questions. His guidance not only improved my critical thinking but allowed me to become a better overall researcher.

I want to express my gratitude to towards the industrial sponsors of this project, Dr. Frank Goodwin of the International Zinc Association and Dr. Andrew Macwan of ArcelorMittal Dofasco. Dr. Goodwin often provided direction for the research project. He always encouraged us to pursue the depths of our research topic while also providing applicable solutions to industry.

I would like to thank all my colleagues in the spot welding research group that made my PhD successful including: Erica Wintjes, Xu Han, Josh He, Ali Ghatei, and Pablo Enrique. I am glad that I was able to work with such inspiring and detected graduate students. I am also thankful for the many memories we shared beyond academics while traveling to conferences, socializing outside of the lab, and the many lunch time discussions. I would also like to thank the students of CAMJ at large for being part of my PhD work environment and for motivating me to work hard as well as creating an excellent atmosphere to conduct research.

I would like to acknowledge my family which has always supported me throughout my academic journey. I would like to thank my fiancée Stefanie Bothwell for her encouragement during my PhD studies. Her steadfast support during the ups and downs associated with academic research helped me persevere through the frustrations. Lastly, I would like to acknowledge my parents, Aldo DiGiovanni, and Angela DiGiovanni. From an early age my parents taught me the value of education and work ethic. The home environment they constructed to foster curiosity and discovery has been instrumental to my development and I am eternally grateful for their support.

Table of Contents

List of Figures

List of Tables

List of Publications

J1. **DiGiovanni C**, Ghatei Kalashami A, Biro E, Zhou NY. Liquid Metal Embrittlement Transport Mechanism in the Fe/Zn System: Stress-assisted Diffusion. Materialia. 2021 18:101153

J2. **DiGiovanni C**, He L, Hawkins C, Zhou NY, Biro E. Significance of cutting plane in liquid metal embrittlement severity quantification. SN. Appl. Sci. 2021 3(6):1-8

J3. Enrique PD, **DiGiovanni C**, Mao N, Liang R, Peterkin S, Zhou NY. Resistance is not futile: The use of projections for resistance joining of metal additively and conventionally manufactured parts. J. Manuf. Proc. 2021 66:424-434

J4. Razmpoosh MH, **DiGiovanni C**, Zhou YN, Biro E. Pathway to understand liquid metal embrittlement (LME) in Fe-Zn couple: From fundamentals toward application. Prog. Mater. Sci. 2021 Published Online

J5. Ghatei Kalashami A, Ghassemali E, **DiGiovanni C**, Goodwin F, Zhou NY. Occurrence of liquid metal embrittlement in a fully ferritic microstructure. Materialia. 2021 15:101036

J6. **DiGiovanni C**, Biro E. Review of Current LME Test Methods and Suggestions for Developing a Standardized Test Procedure. Weld. World. 2021 65:865-884

J7. **DiGiovanni C**, Ghatei Kalashami A, Goodwin F, Biro E, Zhou NY. Occurrence of Sub-Critical Heat Affected Zone Liquid Metal Embrittlement in Joining of Advanced High Strength Steel. J. Mater. Process. Tech. 2020 288:116917

J8. Zhang S, **DiGiovanni C**, He L, Zhou NY. Effect of Liquid Metal Embrittlement Crack on Resistance Spot Weld Static Strength under Different Hardness Ratio. Sci. Technol. Weld. 2020, 26(1): 58-67

J9. Ghatei Kalashami A, **DiGiovanni C**, Razmpoosh MH, Goodwin F, Zhou NY. The effect of silicon content on liquid-metal-embrittlement susceptibility in resistance spot welding of galvanized dual-phase steel. J. Manuf. Proc. 2020 57:370-379

J10. Enrique PD, Li C, **DiGiovanni C**, Peterkin S, Zhou NY. Electrospark deposition interlayers for dissimilar resistance welding of steel to aluminum. Manuf. Let. 2020 24: 123-126

J11. Ghatei Kalashami A, **DiGiovanni C**, Razmpoosh MH, Goodwin F, Zhou NY. The Role of Internal Oxides on Liquid Metal Embrittlement Cracking During Resistance Spot Welding. Met. Trans A. 2020 51:2180-2191

J12. Bag S, **DiGovanni C**, Han X, Zhou NY. A phenomenological model of resistance spot welding on liquid metal embrittlement severity using dynamic resistance measurement. J. Manuf. Sci. Eng. 2020 142(3)

J13. **DiGiovanni C**, He L, Pistek U, Goodwin F, Biro E, Zhou NY. Role of spot weld electrode geometry on liquid metal embrittlement crack development. J. Manuf. Proc. 2019 49:1-9

J14. Han X, **DiGiovanni C**, McDermid JR, Biro E, Zhou NY. Effect of Internal Oxides on Weldability of CMnSi Steels. Weld. World. 2019 63(6): 1633-1639

J15. **DiGiovanni C**, Bag S, Mehling C, Choi KW, Macwan A, Biro E, Zhou NY. Reduction of liquid metal embrittlement cracking using weld current ramping. Weld. World. 2019 63(6):1583-1591.

J16. Enrique PD, Al Momani H, **DiGiovanni C**, Jiao Z, Chan KR, Zhou NY. Evaluation of electrode degradation and projection weld strength in the joining of steel nuts to galvanized advanced high strength steel. J. Manuf. Sci. Eng. 2019; 141(10)

J17. Wintjes E, **DiGiovanni C**, He L, Bag S, Goodwin F, Biro E, Zhou NY. Effect of Multiple Pulse Resistance Spot Welding Schedules on Liquid Metal Embrittlement Severity. J. Manuf. Sci. Eng. 2019; 141(10)

J18. **DiGiovanni C**, Han X, Powell A, Biro E, Zhou NY. Experimental and Numerical Analysis of Liquid Metal Embrittlement Crack Location. J. Mat. Eng. Perm. 2019 28(4):2045-2052.

J19. Wintjes E, **DiGiovanni C**, He L, Biro E, Zhou NY. Quantifying the Link Between Crack Distributions and Strength Loss in Liquid Metal Embrittlement Susceptible Steels. Weld. World. 2019 63(3):807-814;

J20. He, L, **DiGiovanni C**, Han X, Mehling C, Wintjes E, Biro E, Zhou NY. Suppression of liquid metal embrittlement in resistance spot welding of TRIP steel. Sci. Technol. Weld. 2019, 24(6), 579-586

J21. **DiGiovanni C**, Biro E, Zhou NY. Impact of liquid metal embrittlement cracks on resistance spot weld static strength. Sci. Technol. Weld. 2019, 24(3) 218-224

Chapter 1

Introduction

1.1 Background

The ever-growing demand for increased vehicle fuel efficiency has made vehicle weight reduction a primary concern for automotive manufacturers. Weight reduction can be achieved by reducing the sheet thickness of automotive assembly parts, however the structural integrity and vehicle safety cannot be compromised. Use of advanced high strength steels (AHSS) allow automotive manufactures to reduce steel thickness used in components without sacrificing crashworthiness of the vehicle [1,2]. The 1st-generation AHSSs comprised different families of steels with ultimate tensile strength levels limited to 800 MPa, such as transformation-induced plasticity (TRIP) and dual phase (DP) steels [3,4]. The need for higher tensile strengths and elongation in automobile structural components resulted in the development of 2nd-generation of AHSSs known as high-Mn twinning-induced plasticity (TWIP) steels [5–8]. However, due to high alloying levels, cost effectiveness, and weldability issues, industrial processing of austenitic TWIP steels was challenging and hindered their further development. Among various developed steels and processes, medium-Mn TRIP (MMn-TRIP) and quench and partitioned (Q&P) steels known as the 3rd-generation AHSSs and press-hardening steel (PHS) with strength levels up to 1 GPa and 30% elongation attracted much attention [9–12]. A graphical summary of AHSS is shown in Fig. 1-1 which identifies both their strength and ductility.

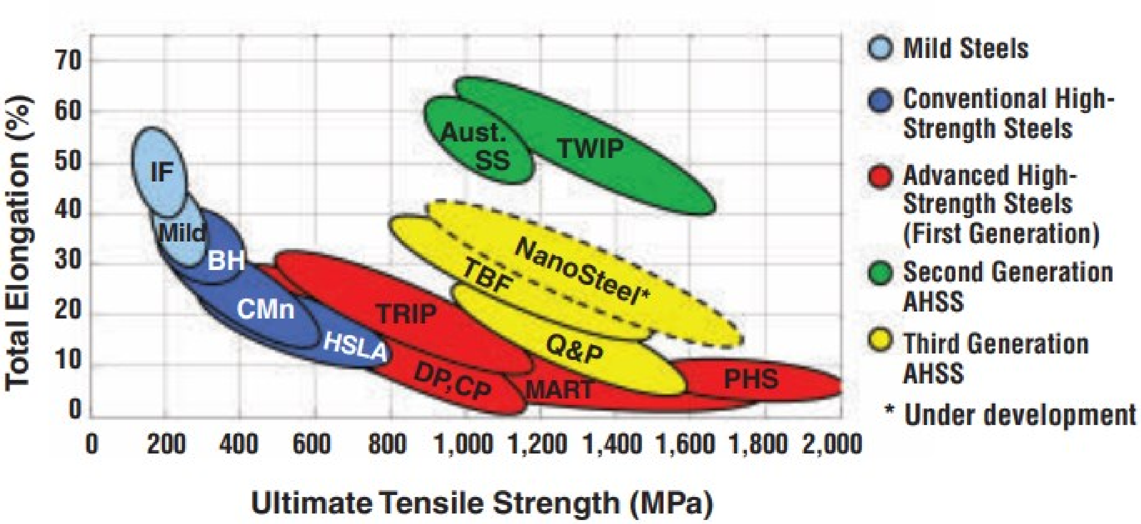

Figure 1-1 *Overview of tensile strength and total elongation combinations for various classes of conventional and advanced high strength steels [13]*

Automotive structures are joined together using several welding processes, but the most widely used process is resistance spot welding (RSW). The RSW process operates by clamping steel sheets in a lap configuration with copper electrodes and passing a large current through the system. However, factors such as the corrosion protective zinc (Zn) coating used on AHSS can add complexities during welding, particularly liquid metal embrittlement (LME). During the RSW process, heat generation is mostly located at the sheet-sheet interface, which creates a lap joint. However, at the sheet surface there is enough heat to melt the Zn coating while the steel remains in a solid phase [14–16]. The interaction between the liquid Zn and solid steel in conjunction with tensile stresses and the susceptible AHSS leads to LME cracking on the weld surface. The cracks forming on the weld surface do not conform to quality standards and are a concern for vehicle safety. Although in recent years there has been a strong research effort into LME during RSW, there remains questions on how the RSW process effects the temperature and stress state of the material to accentuate LME. Research is still ongoing to determine the cause of such severe LME cracking during RSW and to suggest possible mitigation techniques.

1.2 Objectives

This study aims to examine the occurrence of LME in the RSW process and provide a detailed description for LME onset for mitigation of detrimental LME cracks. The main objectives are:

1. Identify the role of LME cracks in joint strength and determine the impact of crack location on load carrying of the joint
2. Establish the RSW process mechanisms leading to LME crack formation
3. Develop approaches for LME reduction during RSW by mitigating the identified formation mechanisms.
4. Establish a link between the LME formation mechanism during RSW and the fundamental mechanisms of LME
5. Characterize the fundamental Zn transport mechanism leading to the onset of LME

1.3 Thesis Outline

This thesis consists of six chapters. A flow chart showing the progression of this research is shown in Fig. 1-2. The first chapter is an introduction presenting the background and objectives of this research. Chapter two includes a comprehensive review of the proposed mechanisms responsible for LME cracks, their appearance in the Fe/Zn system of interest, and the nature of stress/temperature in the LME phenomenon. Additionally, chapter two reviews the occurrence of LME during RSW and the effect of LME cracks on joint strength.

Chapter three through five represent the content from published manuscripts. Chapter three investigates the effects of LME cracks on RSW joint static strength and seeks to define the detrimental cracks that require mitigation. Chapter four identifies the thermomechanical mechanisms in the RSW process that lead to LME cracking and proposes mitigation techniques based on the findings. Using the results of chapter three, chapter four can adequately explain the occurrence of detrimental LME cracks and provide welding solutions. Chapter five builds on the significance of thermomechanical state to uncover fundamental insights into the LME phenomenon. This chapter identified the embrittler transport and LME onset mechanism as it relates to the occurrence of cracking from the RSW process. Lastly chapter six summarizes the main findings of the present research and proposes the future research opportunities.

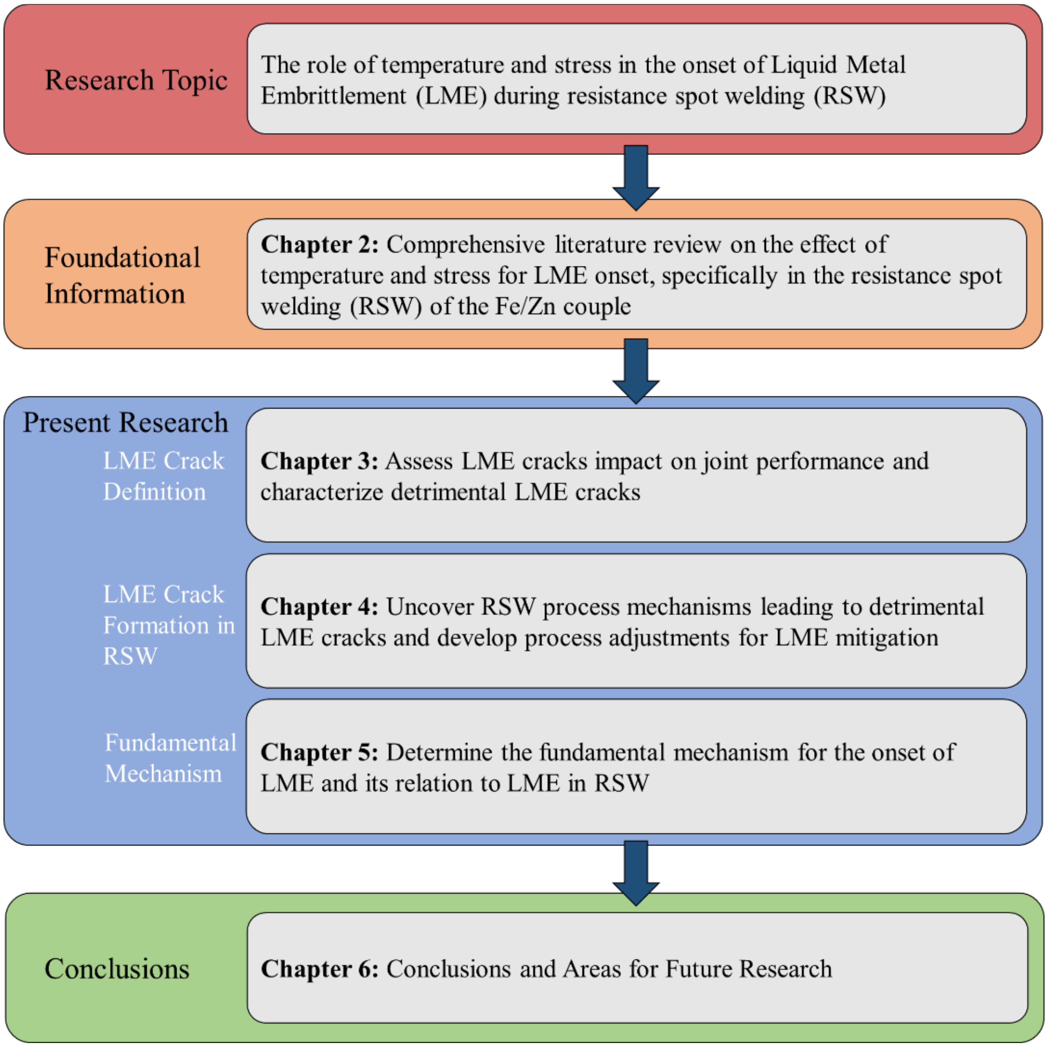

Figure 1-2 *Flow chart of thesis progression*

Chapter 2

Literature Review

2.1 Overview

Liquid metal embrittlement (LME) is the abrupt rupture of a solid metal while in direct contact with a liquid metal. LME has been reported in various solid/liquid couples and has been an active area of academic research for over half a century. In recent years LME research has been pointed towards its occurrence in resistance spot welding (RSW) of newly developed automotive steels. This chapter provides a critical review of the proposed theories and mechanism behind LME and their observation in the Fe/Zn system of interest. Additionally, literature on the occurrence and reduction of LME in resistance spot welding (RSW) will be analyzed in detail. The fundamentals and application of LME reviewed in this chapter provides foundation and direction for LME-RSW research.

2.2 Liquid Metal Embrittlement

Thus far, several mechanisms have been proposed to describe the onset and propagation leading to LME cracking. Despite these efforts, there is still no universal agreement about the LME mechanism. This is due to the general complexity of the phenomenon, lack of experimental/modeling evidence, and potential differences in the mechanism for the various LME couples. Below is a summary of the proposed LME mechanisms, their observation in the Fe/Zn couple of interest, and relevant external factors that have been observed to promote or impede the occurrence of LME.

Proposed LME Mechanisms

Several models have been proposed to explain atomic-scale events leading to LME in different solid/liquid systems. The proposed LME theories can be categorized as either ductile or brittle fracture models with embrittler transport mechanisms described as either liquid flow or diffusion. A timeline of the proposed LME theories over several decades has been illustrated in Fig. 2-1. Table 2-1 summarizes the theoretical models from each category that will be discussed in this section.

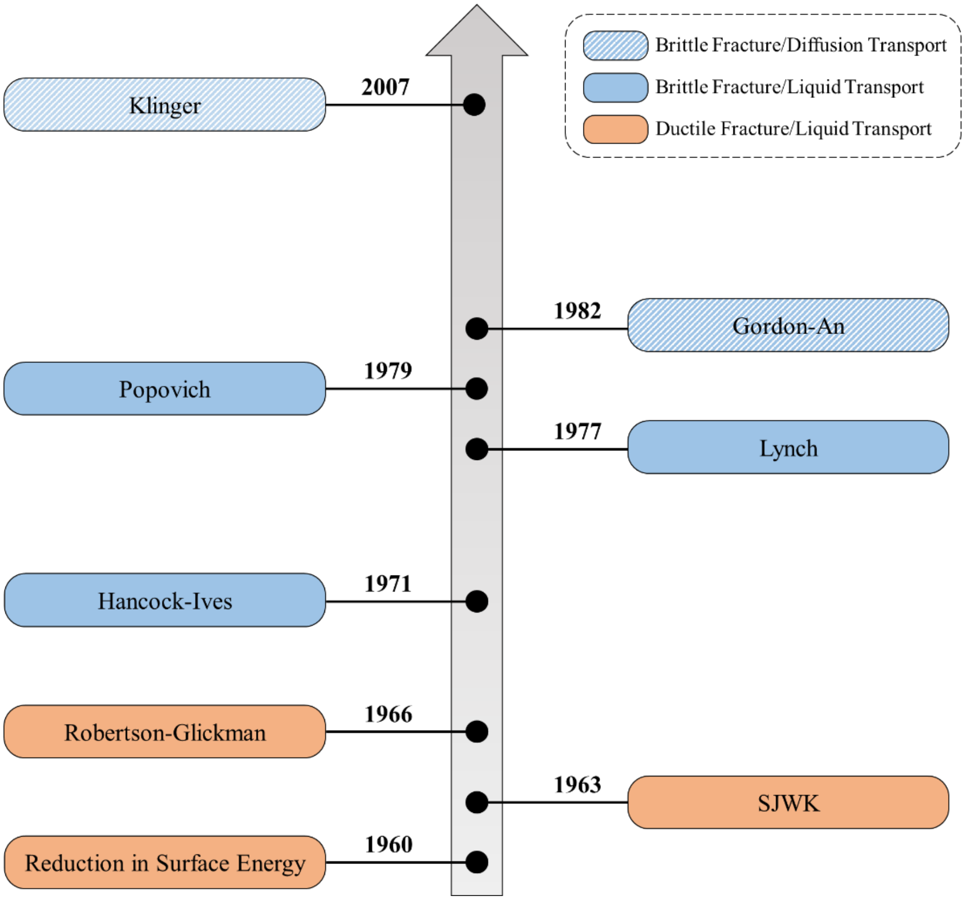

Figure 2-1 *A timeline of the proposed theoretical LME models categorized by model type*

Table 2-1 *Summary of proposed theoretical LME models and their key points*

Category	Theoretical Model	Key Points
Brittle Fracture Models	Reduction in Surface Energy [17]	• Reduction in surface energy due to adsorption of embrittler atoms • Lowers critical stress for occurrence of fracture
	Stoloff-Johnson-Westwood-Kamdar (SJWK) [18,19]	• Liquid atoms weaken solid atoms bonds due to chemisorption • Applied stress breaks weakened bonds
	Robertson-Glickman (DCM) [20]	• Stress-assisted dissolution of solid atoms into liquid • Dissolved solid atoms in the liquid deposited on the crack surface
Ductile Fracture Models	Hancock-Ives [21]	• Dislocation pile-up interaction with liquid metal atoms diffusing ahead of crack tip causing a stress concentration
	Lynch [22]	• Dislocation nucleation facilitated by lower interatomic bond strength from adsorption of liquid metal at crack tip • Void coalescence in plastic zone ahead of crack tip
	Popovich [23]	• Adsorbed liquid atoms increase dislocation activity and activate new slip systems • Enhanced localized work hardening and microcrack nucleation
Grain Boundary Models	Gordon-An [24]	• Stress-assisted grain boundary diffusion of embrittler atoms • Formation of penetration zone at the grain boundary before crack nucleation
	Klinger [25]	• Grain boundary wedging forms a stress gradient along grain boundary • Stress gradients leads to enhanced diffusion of the embrittler leading to stress-assisted diffusion

Fracture Models

The first theory explaining the LME fracture mechanism traces back to 1960 when Rostoker et al. [17] described LME as the reduction of the surface energy (RSE) in the substrate due to the adsorption of the embrittler liquid phase, however the atomistic cause for the reduction in surface energy was not explained. The Stoloff–Johnson–Westwood–Kamdar (SJWK) model [18,19] is an extension of the RSE theory, which provides more detail at the atomic level. In the SJWK model, the liquid metal atoms at the crack tip reduce the interatomic bond strength of the substrate due to new chemical bonds generated at the adsorbent surface (chemisorption). In the presence of stress, this reduction of bond strength leads to bond breaking and crack formation. The next proposed LME theory is known as the dissolution-condensation mechanism (DCM) which was first proposed by Robertson [26] and further developed by Glickman [27–30] and is known as Robertson-Glickman model. The key point regarding Robertson-Glickman model is the repeated mechanism of the solid dissolution at the grain boundary into the liquid, which is blunted, then re-sharped from further dissolution [27–30].

In contrast to the models describing LME as a brittle fracture, models were also developed that considered the role of dislocation movement and pile-up in LME fracture. This classification is labeled as the 'Ductile Fracture Models' in LME literature. However, the experimental studies on LME in the Fe/Zn system has shown no evidence of dislocation activity in the fracture mechanism [31,32] (to be discussed further in the following section). Given the insignificance to the Fe/Zn system, these models will not be discussed in detail but will still be summarized generally as it relevant to the understanding of the LME mechanism. Three main ductile models were developed by: Hancock and Ives [21], Lynch [22], and Popovich [23]. The key points for each model are summarized in Table 2-1, however each model describes LME fracture by the effect the adsorbed liquid embrittler atoms have on dislocation nucleation, movement, and pile-ups. Based on these models, the LME fracture surface would contain ductile features and there will be dislocations present ahead of the crack tip. These brittle and ductile models conflict on the nature of LME fracture, but they both rely on the presence of a liquid embrittler. A similarity shared among all the fracture models is the embrittler is transported as a liquid phase to the crack-tip

Embrittler Transport Models

The early models of LME all described the adsorption of the liquid phase in the crack for propagation or in the grain boundary for initiation. Transport of the embrittler was described as the liquid flow to the crack-tip. For example, the Roberston-Glickman model relied on the constant flow of liquid embrittler to the crack-tip for repeated dissolution of the substrate and re-sharpening. Likewise, the SJWK model relies on the liquid embrittler at the crack tip for chemisorption. The presence of liquid at the crack-tip has been observed recently, as the embrittler was found in a globule-pucker shape on the crack-tip surface indicating it was liquid at the time of grain boundary separation [33]. However, recent work focused specifically on the embrittler transport mechanism has created an alternate description for embrittler transport in LME.

In the past decade, a new model of LME transport has been developed based on grain boundary diffusion of the embrittler into the solid material. This approach to the LME transport mechanism was first introduced by Krishtal [34] and then further developed by Gordon and An by studying conditions leading to crack formation [24]. Based on the Gordon-An grain boundary diffusion model, it is claimed that the embrittler atoms diffuse by stress-assisted diffusion into substrate grain boundaries to form a ‘penetration zone’ where the embrittler atoms collect prior to the observed intergranular fracture. Gordon and An [24] studied the effect of temperature and stress on crack initiation and propagation in both liquid metal-induced and solid metal-induced cracking. Gordon and An determined that the onset of cracking required exceeding a threshold temperature, indicating LME to be thermally activated. Furthermore, the threshold temperature and time for crack formation decreased with increased applied stress, showing that the onset mechanism is stress-dependant. From the study's results it was clear there is a 'critical"' stress level for the embrittlement phenomena to occur. Moreover, the critical stress magnitude was shown to decrease with increasing temperature, both of which would affect the kinetics of the proposed diffusion mechanism.

Building on the stress-assisted diffusion theories from the Gordon-An model, Klinger [25] developed a framework to describe the kinetics of the stress-assisted grain boundary diffusion leading to the onset of LME. In the Klinger model, a geometric diffusion wedge is formed at the grain boundary/free surface interface from the plating out of the diffusing atoms, which leads to a stress gradient along the boundary. The stress gradient causes a chemical potential gradient which results in an additional diffusion flux enhancing the embrittler atom's penetration of the grain boundary. The schematic and numerical results of Klinger's model is shown in Fig. 2-2.

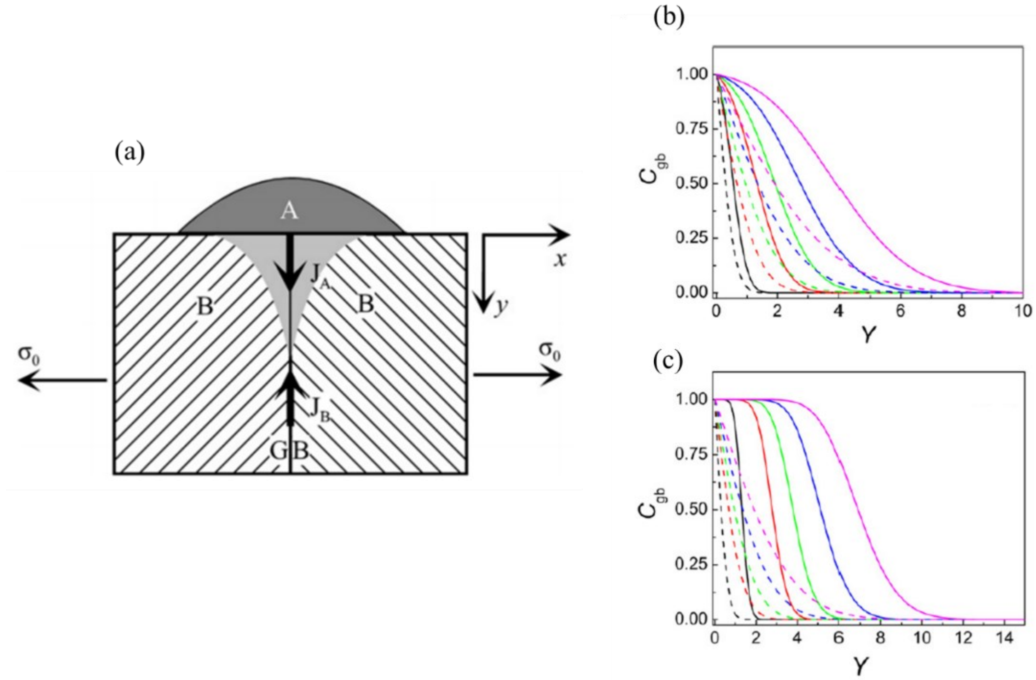

Figure 2-2 *(a) Schematic representation of the Klinger grain boundary diffusion model* [25] *(b) enhanced diffusion (solid lines) under low stress conditions (c) enhanced diffusion (solid lines) under high stress conditions*

A key feature of both these grain boundary diffusion models is that the liquid penetration is preceded by embrittler diffusion into the grain boundary. Recent experimental observations in the Fe/Zn system have shown evidence for diffusion of the embrittler prior to liquid penetration [35] and the phenomenon's increased susceptibility with temperature and stress [36]. For this reason, the grain boundary diffusion models have gained traction in recent years as an accurate description for LME, particularly in the Fe/Zn, which is the focus of the following section.

LME in the Fe/Zn System

The Fe/Zn system is the focus of this thesis and therefore the literature identifying the LME mechanism in that system will be explored in detail. In the Fe/Zn system, theories involving dislocation activity have been ruled out, but an agreed upon model for LME is still missing since experimental results lack enough detail to justify the exact mechanism(s). Furthermore, due to the characteristics of LME in Fe/Zn system such as solubility of Zn into Fe, tendency to formation of intermetallic compounds, formation of LME-cracks at high temperatures (e.g. higher than melting point of Zn), predicting LME behavior is challenging. Numerous investigations have been conducted in the Fe/Zn system over various hot-working processes in the past decade. Researchers have tried to link their observations with the previously discussed LME models for fracture and embrittler transport. In the past several years it has become clear that LME in the Fe/Zn system occurs in an intergranular and brittle fashion, however the description of the embritter transport remains contested. Several studies have reported the presence of liquid Zn at the crack tip leading to fracture while others have noted Zn diffusion into the grain boundary precedes fracture. A review of this studies is required to determine the source and possible reconciliation to the conflicted reports. Table 2-2 summarizes the proposed LME mechanisms in the Fe/Zn system from recent studies.

***Table 2-2** A summary of LME fracture and transport mechanisms in the Fe/Zn system literature*

Fracture	Transport Mechanism	Study	Key Points
Intergranular brittle fracture	I: Zn diffusion II: Liquid Zn flow to crack tip	Kang et al. 2016 [31]	• Stress-assisted Zn diffusion precedes grain boundary wetting or direct liquid Zn penetration are possible • Analysis of the crack after formation made the mechanism unclear
Intergranular brittle fracture	Liquid Zn flow	Lee et al. 2019 [37]	• Liquid Zn penetrates austenite grain boundaries • Region transforms to brittle intermetallic leading to grain boundary fracture
Intergranular brittle fracture	Zn diffusion	Razmpoosh et al. 2018 [38]	• Low Zn wt% ahead of the LME crack tip indicated Zn diffusion precedes crack growth • LME susceptibility increased with increased tensile loading
Intergranular brittle fracture	Liquid Zn flow	Murugan et al. 2020 [33]	• Direct contact of liquid Zn with steel • Zn liquid at crack tip and during instant of grain boundary separation (SWJK model)
Intergranular brittle fracture	Zn diffusion	Ling et al. 2020 [39]	• Low Zn wt% ahead of the LME crack tip indicated Zn diffusion precedes crack growth
Intergranular brittle fracture	Liquid Zn flow	Razmpoosh et al. 2020 [32]	• Liquid Zn penetration to the crack-tip induces grain boundary fracture (SJWK model)
Intergranular brittle fracture	Zn diffusion	Razmpoosh et al. 2021 [35]	• Micro-events leading to LME: 1. Stress-assisted diffusion into the grain boundary 2. Fracture in grain boundary area 3. Liquid Zn flow following grain boundary separation

From the summarized literature in Table 2-2, no study has reported evidence of ductile LME fracture. The brittle fracture is compatible with all the experimental observations of LME, while the presence and involvement of dislocations in LME fracture has not been reported. Kang et al. [31] claimed that due to the lack of evidence for an increased dislocation density near LME-crack tip, crack initiation from ductile fracture (dislocation activity) models are not applicable to the Fe/Zn system. However, brittle LME fracture is stated in each of the studies. The SJWK model is the most reported fracture model for LME in the Fe/Zn system.

The experimental observations showing liquid embrittler penetration leading to brittle intergranular fracture are highlighted in Fig. 2-3. Kang et al. [31] argued that the presence of Γ-$(Fe,Mn)_3Zn_{10}$ into the LME-crack (as shown in Fig. 2-3(a)) implies that the Zn liquid phase was present at high temperatures in the crack tip region. Lee et al. [37] explained LME occurrence by Zn infiltration into the grain boundaries, based on microstructural analysis of the cracked zone. As illustrated in Fig. 2-3(b), the crack area is composed of Γ and α-Fe(Zn) phases which indicates that Zn liquid infiltrated into the grain boundaries. The TEM-EDS line profile of the crack area shows the presence of approximately 30 at.% Zn in the grain boundaries. Additionally, Murugan et al. [33] examined the fracture surface of LME cracks in detail and observed the spike-like globules (Fig. 2-3(d)) of 62 wt% Zn, indicating the presence of a liquid phase at the incident of fracture. The authors concluded a liquid penetration of Zn and brittle fracture that aligns with the SJWK model. Razmpoosh et al. [32] conducted HRTEM and EELS elemental maps of the Zn-penetrated portion of a grain boundary (Fig. 2-3(c)) which show brittle intergranular fracture and indicated liquid Zn flow to the crack tip precedes grain boundary fracture. The authors identified their observations as the SJWK model. The studies discussed and the observations shown in Fig. 2-6 conclusively show the brittle nature of the LME fracture, but the discussion on the transport mechanism leading to LME is limited.

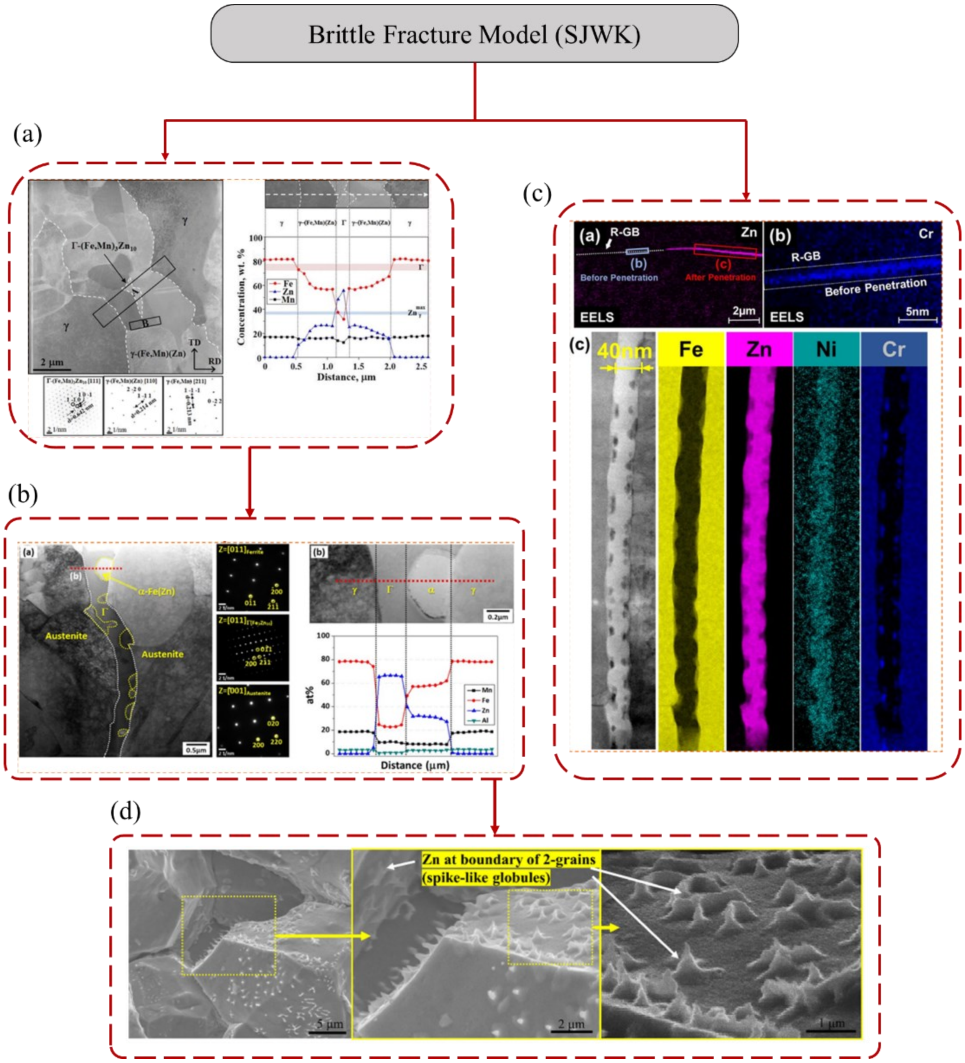

Figure 2-3 Experimental observations for brittle LME fracture (a) TEM micrographs along with Zn EDS elemental distribution at a grain boundary which confirms the presence of liquid Zn in LME-crack [31] *(b) STEM bright-field image, selected area diffraction patterns of the cracked zone and EDS line profile showing liquid Zn penetration* [37] *(c) HRTEM micrograph and EELS maps of the alloying elements of the grain boundary after Zn-penetration* [32] *(d) Spike-like globules of Zn on brittle intergranular fracture surface indicating the presence of liquid Zn at the instant of fracture* [33]

Kang et al. [31] proposed a description of LME based on the SJWK model (Fig. 2-4(a)) but admitted it was possible another mechanism was responsible for the Zn transport into the grain boundary. As described by Kang et al. [31], in the stress-assisted diffusion model (Fig. 2-4(b)), Zn atoms diffuse into the steel grain boundaries by stress-assisted solid-state diffusion. As Zn reaches its maximum solubility in the solid grain boundaries, small islands of liquid Zn are formed by which the grain boundary cohesion is lost, and cracks are initiated.

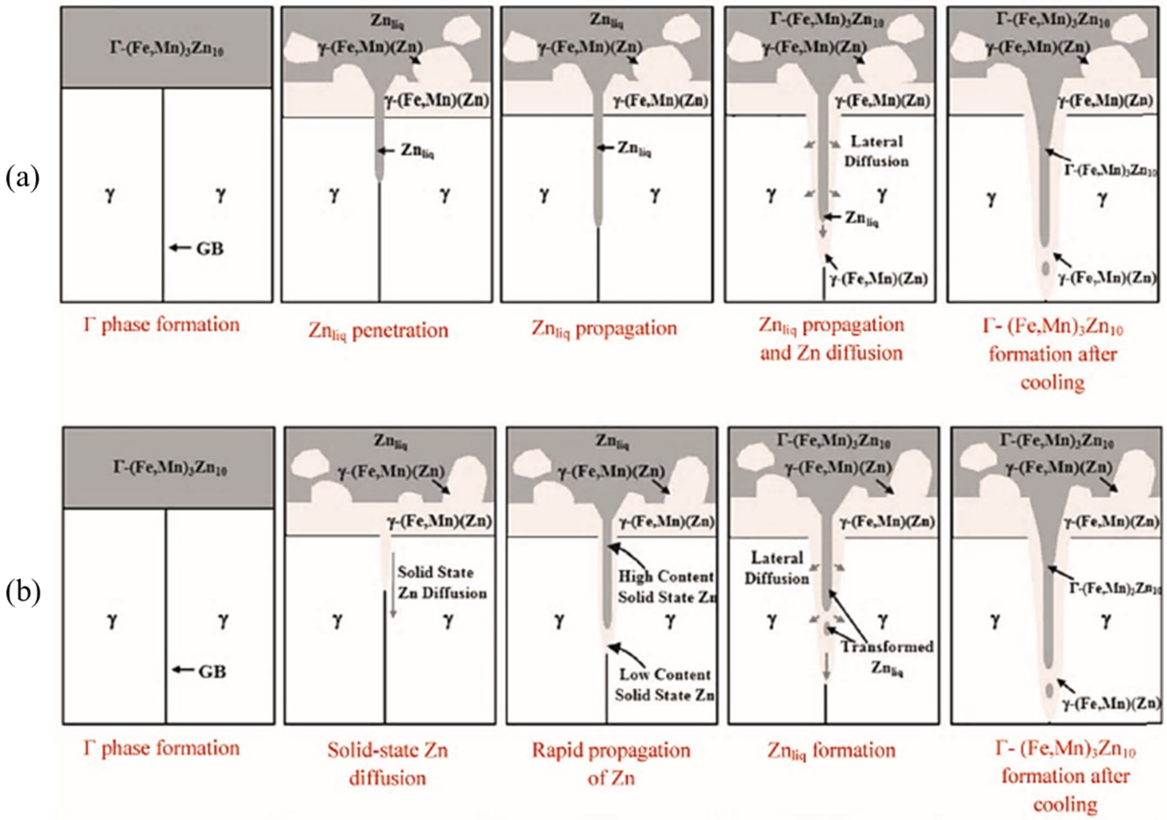

***Figure 2-4** Mechanism of LME crack formation by Kang et al.* [31] *in Zn-coated TWIP steel during hot-tensile testing; (a) chemisorption of liquid-metal (or SJWK) model and (b) stress-assisted diffusion model*

Kang et al. argued that the presence of a low amount of Zn (4 wt.%) at the grain boundary tip indicates that solid-state grain boundary diffusion occurred during the embrittlement event. This interpretation has been also implemented by other recent studies as evidence for occurrence of the grain boundary diffusion model. The experimental observations from recent studies on the transport mechanism of LME aligned with the grain boundary diffusion models are summarized in Fig. 2-5. Ling et al. [39] considered solid-state diffusion during resistance spot welding of AHSS based on TEM observations from the crack zone. The highest content of Zn was detected as 9.42 wt.% which indicates that no liquid phase reached the crack tip, and the existence of Zn was a result of solid-state Zn diffusion (Fig. 2-5(b)). Razmpoosh et al. [38] also argued that low Zn content at the crack tip and ahead of the crack is an indication of the grain boundary diffusion model (Fig. 2-5(c)). Recently, Razmpoosh et al. [35] also conducted a detailed atomic probe tomography (APT) analysis on Zn penetrated grain boundaries and further emphasized the grain boundary diffusion mechanism. Zn penetration along a grain boundary occurs in micro-event stages. First, Zn atoms diffuse into grain boundary by stress-assisted diffusion which results in weakening of the adjacent Fe-Fe atomic bonds. Thereafter, a fracture path is created on one side of the grain boundary, and finally, liquid Zn flows into the newly formed crack (Fig. 2-5(d)).

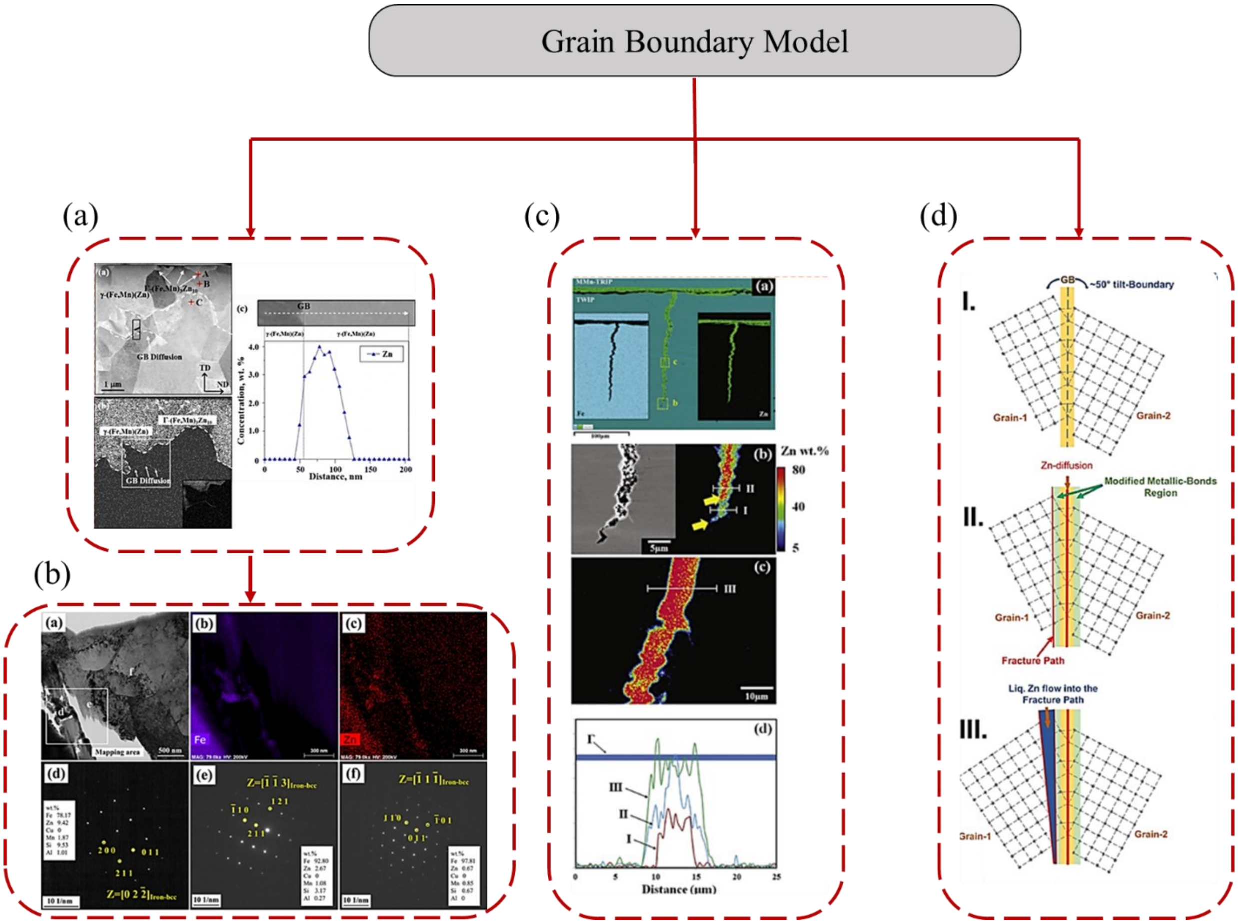

Figure 2-5 *Experimental observations for validation of grain boundary diffusion mechanism for occurrence of LME in different Fe/Zn system; (a) STEM micrograph close to the tip of the LME crack showing Zn penetration by Kang et al.*[31]*, (b) TEM micrograph along with EDS maps and selected area diffraction (SAD) patterns of the LME crack zone showing Zn solid-state diffusion by Ling et al.* [39]*, (c) EDS and EPMA elemental map showing Zn diffusion ahead of the crack tip by Razmpoosh et al.* [38] *and (d) Schematic illustration of micro-events by Razmpoosh et al.* [35] *which starts with solid-state diffusion penetration.*

The most recent studies investigating the LME mechanism in the Fe/Zn system have established Fe/Zn LME to be a brittle fracture, with no study reporting evidence of ductile fracture. However, there remains some contrasting observations between the liquid penetration based embrittler transport and the grain boundary diffusion models. From the literature presented in this section, there appears to be evidence for both models, but the most recent studies agree on a diffusion-based mechanism. The detailed micro-events proposed by Razmpoosh et. al [35] provides some insight into the contrasting results, as that description states that Zn liquid penetration is preceded by Zn grain boundary diffusion. This indicates the elementary Zn transport mechanism is grain boundary diffusion while also explaining the evidence for the presence of liquid Zn in the crack. However, it does not fully explain the observation of Murugan et al. which showed Zn in liquid phase at the instant of fracture. The literature has shown that grain boundary diffusion plays a role in LME as it is consistently observed ahead of the crack tip but an interrupted or in-situ investigation is needed to provide the final insights into LME onset and Zn transport mechanism.

Stress and Temperature Effect on LME

There are three broad factors necessary for the occurrence of LME which includes:

(i) Applied tensile stress
(ii) Susceptible solid substrate
(iii) Direct contact of the liquid embrittler

Additionally, in the Fe/Zn system, a susceptible temperature is also recognized as a factor [14]. Each of these prerequisites has characteristics which control the degree of susceptibility to LME-cracking. This section will focus on the characteristics of applied tensile stress and temperature as they are the factors relevant to the objectives of the thesis.

As stated above, the occurrence of LME in the Fe/Zn system is dependent on the temperature of the process and tensile stress applied to the Fe substrate. Several studies have examined the role of temperature in Fe/Zn LME and tried to uncover the cause for the susceptible range. Albeit more limited, researchers have looked at the minimum applied stress required for LME but the mechanistic role of stress in LME remains unclear.

Beal et al. [40] extensively studied the influence of temperature and stress on Zn-induced LME in steel using thermomechanical Gleeble testing. A temperature range of 700 °C – 900 °C was identified where LME occurred (labelled as ‘ductility trough’) and it was concluded LME is only active in this range. However, it was also noted that the minimum temperature for LME occurrence lowers with strain rate. Additionally, Kang et al. [41] examined TWIP, press-hardened steel (PHS), and interstitial-free (IF) steel using thermomechanical testing, and found Zn-penetration to consistently occur in the TWIP steel, and no evidence of Zn penetration in the IF steel. Since the IF steel was tested both below the Ac_1 temperature (no austenitic transformation) and above the Ac_3 temperature (complete transformation to austenite), it was concluded that LME does not exclusively depend on crystal structure. It was theorized that the IF steel’s low load carrying (and therefore mild stress state), and lack of alloying elements did not allow Zn penetration of the steel grain boundaries. Jung et al. [15] studied LME in AHSS with different microstructures, such as TWIP steel, DP steel and draw quality steel. Similarly, Jung et al. also concluded the crystal structure was not exclusively responsible for the occurrence of LME [15]. Similar to the previous work, a temperature range was identified for LME, which depended on strain rate and steel type.

Beal et al. investigated the effect of strain rate on LME. It was discovered that the onset of LME occurs at lower temperatures if the strain rate is high (1.3 s^{-1}). It was theorized this is due to the increase in flow stress, which allows the steel to reach the higher stress levels necessary to trigger LME. This created the idea (formulated by Beal et al.) of a critical stress required for the onset of LME, which is shown in Fig. 2-6. It can be seen from the figure that LME only occurs in cases where the UTS is greater than the critical stress. Thus, in cases of high strain rate, the UTS is increased which then exceeds the critical stress. Additionally, the critical stress also explains the lack of LME below 700 °C. From Fig. 2-6 it is shown that the critical stress is higher than the UTS at lower temperatures, thus not triggering LME.

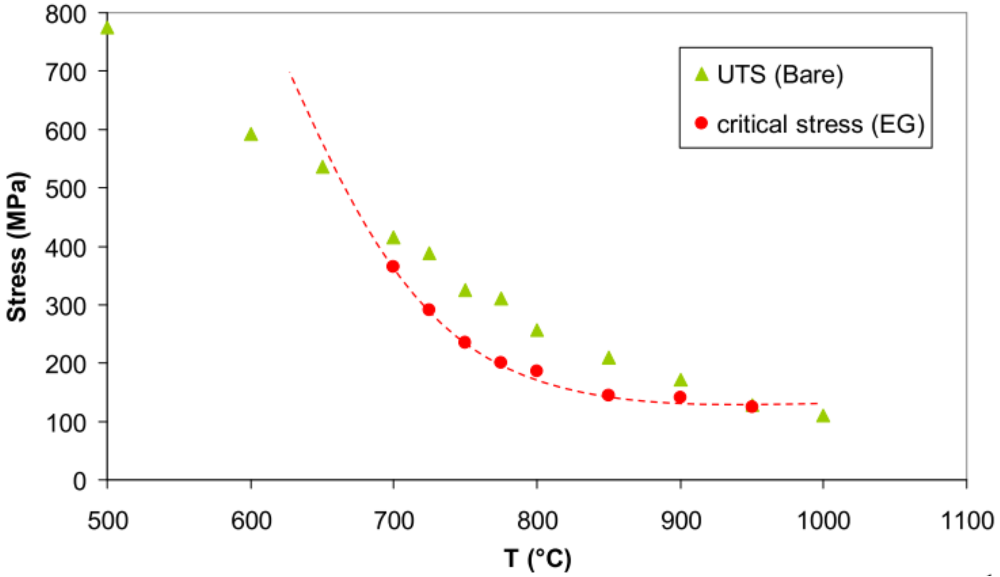

Figure 2-6 *Critical stress for onset of LME at various temperatures* [42]

Similar findings were reported by both Jung et al. [15] and Bhattacharya et al. [43] who also carried out thermomechanical testing. This further supports the notion of a critical stress (which appears temperature dependent) for the onset of LME. Therefore, the material stress state is significant for the onset of LME. Beal et al. [44] prepared AHSS cup samples with high residual stresses and submerged them into a liquid Zn bath at 440 °C and LME occurred. The authors concluded that LME occurred below the established temperature range due to the high residual stresses which exceeded the critical stress for LME. Although excellent work has been done to discover and establish the concept of a critical stress for the onset of LME, much more detail is necessary to understand why stress state dominates the onset of LME. Considering the recent research showing LME to be a grain boundary diffusion-based phenomenon in the Fe/Zn system, it is logical the temperature and stress state of the solid would enhance LME process thus increasing susceptibility.

2.3 Grain Boundary Diffusion

Grain boundary diffusion is the mechanistic basis for many materials science phenomena such as intermetallic compound growth [45], coating growth [46], sintering [47] and brazing [48]. In recent years, grain boundary diffusion has become a discussed mechanism for LME. As recent experimental evidence and mathematical modeling has pointed towards a grain boundary diffusion mechanism for LME, a comprehensive understanding of grain boundary diffusion is necessary to contribute detailed LME research and explain its occurrence during material processing.

Theoretical Aspects of Grain Boundary Diffusion

Grain boundaries provide a high diffusivity path in the bulk material. Due to the high concentration of defects in the grain boundary resulting from their crystallographic misalignment, diffusion occurs much faster than in the bulk, where the defect concentration is much smaller. The general approach to modeling grain boundary diffusion involves the use of a so-called uniform thin slab model. This was first proposed by Fisher [49] which detailed the grain boundary as an isotropic slab of material of uniform thickness within which diffusion occurs according to Fick's laws.

The grain boundary slab model has a relatively simple geometry, where one isolated grain boundary (a bicrystal scenario) or parallel grain boundaries (a polycrystal scenario) is assumed perpendicular to the free surface. This is shown schematically in Fig. 2-7. It is assumed that the concentration variation across the grain boundary slab (x-direction) can be neglected and the diffusivity along the grain boundary is much larger than in the bulk material lattice.

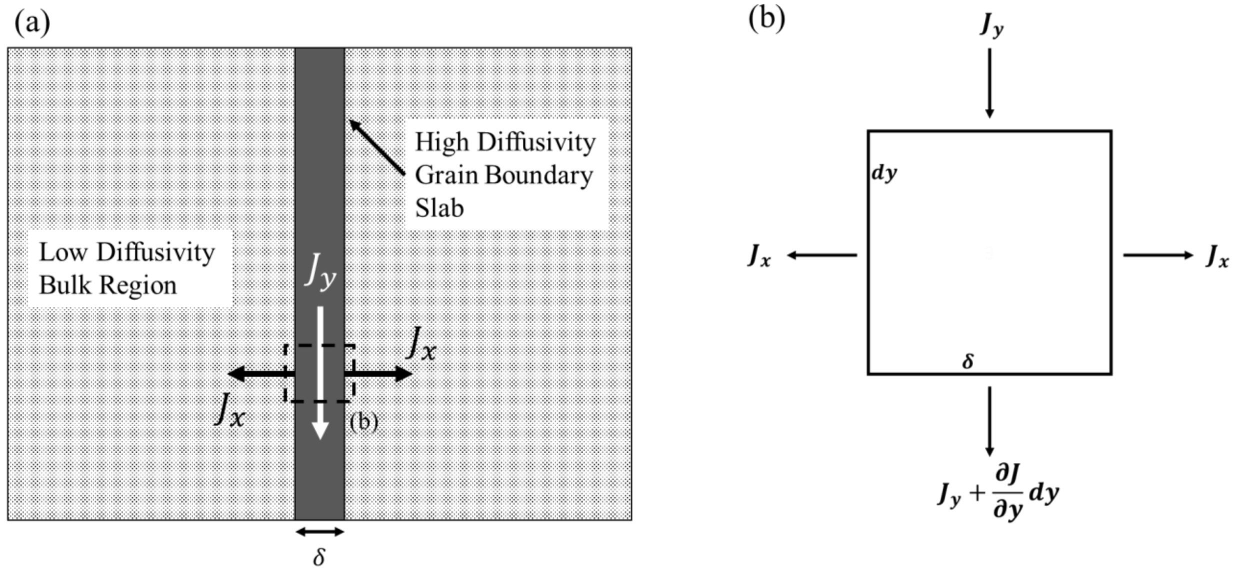

Figure 2-7 *(a) schematic of the grain boundary diffusion model developed by Fisher (b) Diffusion fluxes passing in and out of a grain boundary element*

The fluxes in Fig. 2-7 follow Fick's 1st Law [50] which states:

$$J_y = -D_{gb} \frac{\partial c_{gb}}{\partial y} \qquad (2-1)$$

$$J_x = -D \frac{\partial c}{\partial x} \qquad (2-2)$$

Where, c and c_{gb} are the solute concentrations in the bulk material and in the grain boundary respectively, D and D_{gb} are the diffusion coefficients in the bulk material and in the grain boundary respectively. By performing a mass balancing on an element in the grain boundary (Fig. 2-7(b)) and substituting Eq. 2-1 and 2-2 we can obtain the continuity equation for grain boundary diffusion:

$$\dot{m}_{acc} = \dot{m}_{in} - \dot{m}_{out} \qquad (2-3)$$

$$\frac{\partial c_{gb}}{\partial t} = \frac{1}{1\,dy\,\delta}\left[\delta\left(J_y - J_y - \frac{\partial J_y}{\partial y}dy\right) - 2dyJ_X\right] \qquad (2-1)+(2-2) \rightarrow (2-3)$$

$$\frac{\partial c_{gb}}{\partial t} = D_{gb}\frac{\partial^2 c_{gb}}{\partial y^2} + \frac{2D}{\delta}\left(\frac{\partial c}{\partial x}\right)_{x=\delta/2} \qquad |x| \leq \frac{\delta}{2} \qquad (2-3b)$$

Where δ is the thickness of the grain boundary slab. Additionally, in the bulk material the diffusion equation is:

$$\frac{\partial c}{\partial t} = D\left(\frac{\partial^2 c}{\partial x^2} + \frac{\partial^2 c}{\partial y^2}\right) \qquad |x| > \frac{\delta}{2} \qquad (2-4)$$

Eq. 2-4, which describes the diffusion in the bulk material, shows the typical structure of Fick's 2nd law in a two-dimensional system. However, Eq. 2-3b which describes the diffusion in the grain boundary slab is more complex and is made up of two parts. The equation indicates that the solute concentration in the grain boundary results from the difference of the flux along the grain boundary (first term) and flux into the bulk material (second term). Before examining the solutions to the isolated grain boundary problem, it is important to note the nature of these governing equations. In Eq. 2-3b there are two diffusion fluxes at play that compete for the resultant concentration and solute penetration. Furthermore, since both c and c_{gb} appear in Eq. 2-3b there is clearly a dependence on the solution for c from Eq. 2-4.

The first analysis of combined lattice and grain boundary diffusion was carried out by Fisher [49] for a semi-infinite sample with a slab of grain boundary and an infinite source (constant surface concentration). Whipple [51] provided an exact solution to this problem by using a Fourier-Laplace transformation approach. Suzuoka [52] later solved the case of an instantaneous source (finite surface source) condition utilizing Whipple's transformations to evaluate the complex inversion integral. Although Whipple and Suzuoka analysis provides an exact continuum model solution, in practice many investigators continue to use Fisher's analysis since it is simpler to apply. Furthermore, with the advances in computing technology the application of numerical methods such as the finite difference method has become common for developing solutions.

Harrison [53] defined three classes of grain boundary diffusion kinetics which depend on the strength of the diffusion flux out of grain boundary and into the bulk material (in a polycrystalline analysis it also depends on grain size). The first class labelled as Type A kinetics describes when the flux to the bulk is dominant and the lattice diffusion distance large compared to the grain size. Grain boundary diffusion depth penetration has been reduced and much of the solute has diffused into the grain. In Type B kinetics, the diffusion into the bulk is weaker and each grain boundary is assumed to be isolated. This is identical to the bicrystal model developed by Fisher, Whipple, and Suzuoka which considered both segments of Eq. 2-3b. Lastly, in Type C behaviour, there is negligible lattice diffusion and diffusion only occurs along the grain boundary meaning the second term in Eq. 2-3b can be neglected. This kinetic regime is common at relatively low temperatures when grain boundary diffusion is much more dominant than bulk diffusion. A schematic representation of Harrison's classifications is shown in Fig. 2-8. It is noteworthy that when using the previously described infinite source surface conditions in the Type C regime, the solution simplifies to the common error function [54].

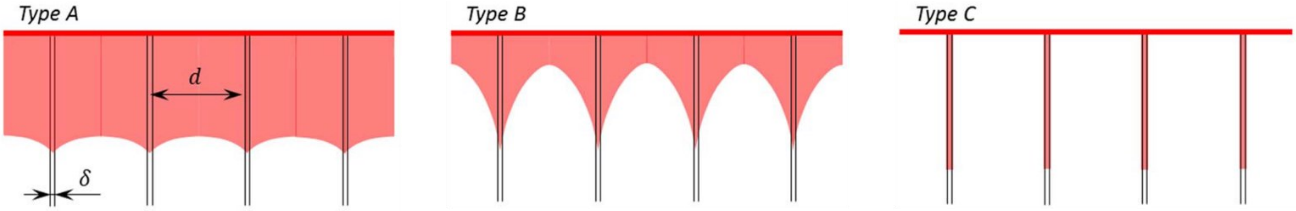

Figure 2-8 *Schematic representation of Harrison's classification of grain boundary diffusion kinetics* [55]

As the literature moves towards a grain boundary diffusion description of LME, these governing equations are essential to understanding the onset of LME. The mathematical description of grain boundary diffusion provides otherwise forgone insights, such as the embrittler's penetration's dependence on both bulk and grain boundary diffusivity and the critical role temperature plays in kinetic regime and diffusivity coefficient. However, LME researchers have noted that classic grain boundary diffusion is typically not sufficient and requires enhancement from a stress-assisted mechanism [31,56].

Stress-assisted Diffusion

In addition to the flux effects of a concentration gradient, a potential gradient also causes the movement of atoms. In the general case of a potential gradient, consider a single particle moving in a potential field $\mu(x, y)$; the gradient of this potential describes the force F on the particle [57]. Thus:

$$F = -\nabla\mu \qquad (2-5)$$

As an analogy to macroscopic particles, consider a marble on an inclined plane. The potential in this case is due to gravity and from classic mechanics it is established the force on the particle parallel to the plane is proportional to the slope of the plane. It has been found empirically that a potential gradient of force gives rise to a diffusion velocity (v) dependent on both the force and the atomic mobility (which is proportional to the diffusivity constant $M = {}^{D}/_{kT}$). In applying a potential gradient instead of a concentration gradient, one small force is simply replaced with another. To now translate this literary description of the potential field flux into a mathematical description, it follows:

$$J_s = vc = MFc = -\frac{Dc}{kT}\nabla\mu \qquad (2-6)$$

Where J_s is the diffusion flux caused the gradient in potential field and c is the concentration of the solute. In the case where the potential gradient is an elastic stress gradient, the relationship is described as [58]:

$$\nabla\mu = -\Omega\nabla\sigma \qquad (2-7)$$

Where Ω is the atomic volume and $\nabla\sigma$ is the stress gradient. Substituting Eq. 2-7 into 2-6 gives the mathematical description of the stress diffusion flux.

$$J_s = \frac{D\Omega c}{kT}\nabla\sigma \qquad (2-6b)$$

In the case of both a concentration gradient (J_c as Fick's 1st Law) and potential gradient (Eq. 2-6b) the two fluxes must be combined to determine the overall flux

$$J = J_c + J_s = -D\nabla c + \frac{D\Omega c}{kT}\nabla\sigma = -D\left(\nabla c - \frac{c\Omega\nabla\sigma}{kT}\right) \qquad (2-8)$$

Where J describes the combined effect from both fluxes. The combined fluxes can now be used in the overall mass balance continuity equation to determine $c(x, y)$ in the presence of a stress gradient.

With a theoretical description and mathematical definition of stress-assisted diffusion established, the concept can be applied to grain boundary diffusion. The integration of the stress diffusion term was first carried by Bika and McMahon [59] to develop a model for dynamic grain boundary embrittlement. The governing equations can be developed by substituting the combined fluxes (Eq. 2-8) into Fisher's model for grain boundary diffusion. In this case, the governing equation for grain boundary diffusion becomes:

$$\frac{\partial c_{gb}}{\partial t} = \frac{\partial}{\partial y}\left[D_{gb}\frac{\partial c_{gb}}{\partial y} - \frac{c_{gb}\Omega D_{gb}}{kT}\frac{\partial \sigma}{\partial y}\right] + \frac{2D}{\delta}\frac{\partial c}{\partial x} \qquad (2-9)$$

Although the governing equation appears long and complex, researchers have been able to develop solutions numerically in recent years using both finite difference method and finite element method. The challenge researchers have identified when solving this mathematical model for stress-assisted grain boundary diffusion is the determination of the stress gradient along the grain boundary. In other words, developing an accurate equation for $\sigma(y)$.

As mentioned in the previous section, Klinger [25] proposed a mathematical model of stress-assisted grain boundary diffusion applied to LME in Cu/Bi. As described by Rabkin [56], in many cases the grain boundary diffusion speed driven purely by a concentration gradient is insufficient to explain the occurrence of LME. This is in agreement with the Gordon-An model and Klinger built on Rabkin's idea to develop his model incorporating the stress diffusion flux.

Klinger developed a stress function based on the model for dynamic embrittlement proposed by Bika and McMahon [59]. Their model states that a cavity or wedge forms at the grain boundary/free surface interface due to the plating out of the diffusing atoms. Under a global external stress on the bulk material, the diffusion wedge formation leads to a stress relaxation at that location, which results in a stress gradient along the boundary and a diffusion flux as described by Eq. 2-6b. Gao et al. [60] utilized this approach to model the formation of diffusion wedges leading to cracking of thin films in a single component system. Klinger looked to extend the model by Gao et al. to a two-component system that better represented LME. Based on the method of Gao et al., Klinger developed a shape function for the stress along the grain boundary that represented the relaxation provided by the wedge formation. Klinger's model proved successful at describing the enhanced diffusion kinetics of the embrittler leading to LME, however it must be noted that his model lacks experimental evidence. Although theoretically sound, it requires detailed experimental analysis to confirm its accuracy.

From Eq. 2-9, two key parameters have a strong effect on the diffusion kinetics: applied stress and temperature (which greatly affects the diffusivity coefficient). It should therefore come as no surprise that LME is typically observed in hot-working processes which involve high temperatures and tensile stresses. In recent years, RSW has been identified as an LME susceptible process. The foundational understanding of LME and grain boundary diffusion kinetics is imperative to analyze the RSW process and determine why the process greatly accentuates LME cracking.

2.4 LME in Resistance Spot Welding

The occurrence of LME in the RSW of 3G AHSS has become a highly researched topic in academia over the past five years. RSW has been identified to accentuate the LME phenomena due to the elevated temperatures and stresses produced by the process [61]. However, the sources of stress during the RSW and their relation to LME cracking are not identified. Furthermore, how the thermomechanical RSW mechanisms relate to the fundamental LME mechanisms remains unclear. This section will provide a brief review of the RSW process as well as examine the research investigating the RSW process aspects that accentuate cracking. Lastly, the limited literature characterizing LME crack's detrimental effect on joint strength will be reviewed.

Resistance Spot Welding Process

Automotive structures are joined together using several welding processes, but the most widely used process is RSW. The process is an economical method for joining metals and is particularly useful for thin sheet materials, which are common in automotive structures. The sheets to be joined are stacked together in a lap configuration, to create a joint at the sheet-sheet interface. The RSW process operates in five fundamental steps as illustrated in Fig. 2-9. First, the workpiece is loaded between the water-cooled copper electrodes. The electrodes essentially provide three functions: a conduit to carry high current to the workpiece, a heat sink to control the weld formation/cool down, and to apply a force for better contact. In the second stage, the electrodes clamp down on the sheets and the force is applied (squeeze time), which is followed by passing a current through the sheets to be joined (weld time). Once the weld cycle is complete, a quality joint is ensured by the continued squeezing while cooling to avoid any voids or other shrinkage defects (hold time). The electrodes then release.

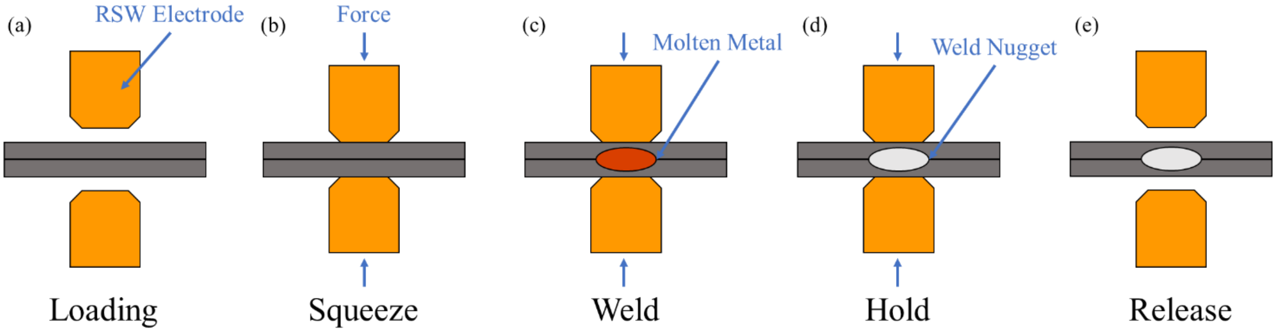

Figure 2-9 *Stages of RSW process (a) material loading (b) squeeze time (c) current application and material melting (d) hold time for cooling and solidification (e) electrode release*

The resultant fusion zone (FZ), also referred to as the weld nugget, occurs at the sheet-sheet interface. Adjacent to the FZ is the heat affected zone (HAZ) where the heat of the process has caused metallurgical transformations in the solid material. In the case of steel welding, this is separated into the upper-critical heat affected zone (UCHAZ) and sub-critical heat affected zone (SCHAZ) which is distinguished by the austenite phase transformation. The austenite transformation is dependent on exceeding the steel's transformation temperature (Ac_1), which therefore indicates the maximum or minimum temperatures of each region based on the transformations that took place. A schematic of the RSW cross section and HAZ is shown in

Fig. 2-10. The HAZ and the associated phase transformations have been the cause of several welding issues such as softening [62,63] but also provides indicators of the thermal history experienced by the material during RSW.

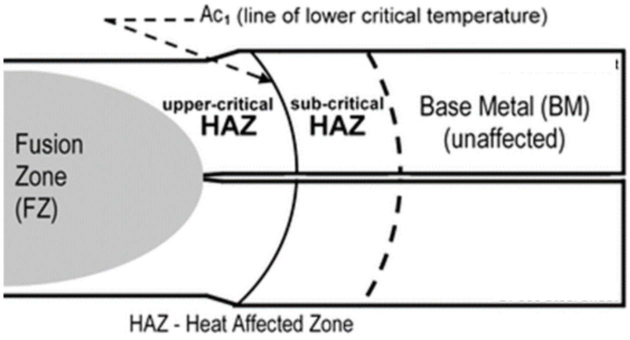

Figure 2-10 *Schematic of heat affected zone regions in a typical RSW joint* [63]

In addition to the phase transformations, RSW also provides the necessary conditions for the occurrence of LME. A Zn coating is commonly used to protect the sheet steel from the corrosive environment during its service life. However, during the RSW process, the Zn coating at the electrode-sheet interface melts while the steel substrate stays solid. This is due to the heat generated from the process and much lower melting temperature of Zn (419 °C) compared to the steel (~1475 °C); creating a liquid embrittler in contact with a susceptible material. The RSW process also provides the required stresses for the onset of LME. The specific stress mechanisms during RSW leading to LME remain unclear, but generally it is thought the clamping pressure and temperature gradients of the process lead to stresses in the substrate at the electrode sheet-interface [61]. During welding, the melted Zn coating penetrates into the steel grain boundaries, which are under tensile stresses from the RSW process, leading to the formation and propagation of LME cracks [16,64,65]. A diagram showing the presence of the three necessary factors is shown in Fig. 2-11. The occurrence of LME during RSW of Zn coated steels is a recent finding, and limited research has been conducted in this domain. LME cracks have been observed in DP and TRIP steels with tensile strengths less than 1000 MPa [66–68]. However, LME cracking has been much more commonly observed in 3G AHSS with tensile strength greater than 1000 MPa.

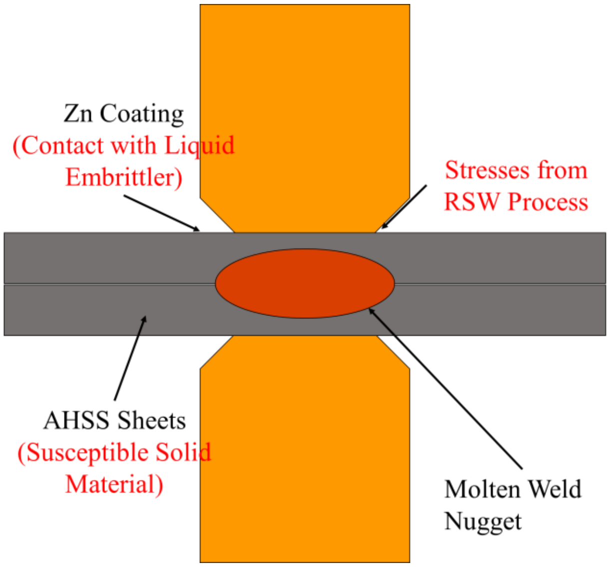

Figure 2-11 *Schematic of the RSW process showing the nugget location and prerequisites for LME formation*

LME Crack Characterization

Researchers have observed LME cracks of varying depths and in multiple locations around the spot weld [14]. LME crack locations have been categorized according to their location with respect to the spot weld geometry. These are: the weld surface above the nugget or centre (Type A), the weld indent shoulder (Type B), and at the sheet-sheet interface (Type C), which are all shown in Fig. 2-12 [69]. Although LME cracks can vary in depth, cracks up to 1000 µm have been reported in both the Type A and Type B locations after welding using severe conditions (high heat input) [70,71]. There is no present literature describing the distinctions in cause and timing of these three LME crack classifications, which is fundamental for designing techniques to mitigate cracking.

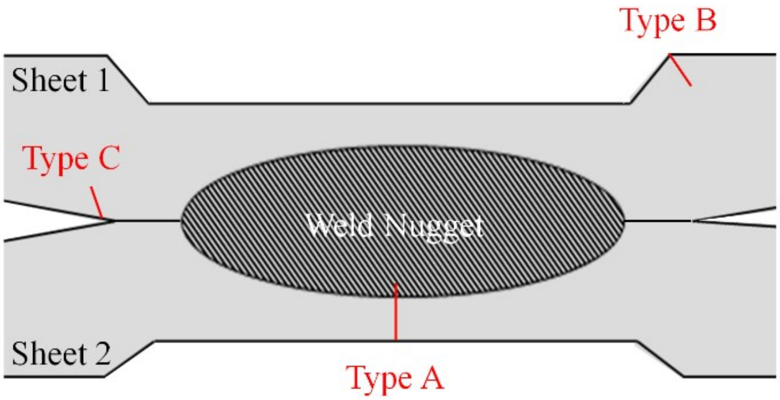

***Figure 2-12** Observed regions for LME cracking in RSW*

There are numerous welding parameters used in the RSW process to control weld size and quality. Weld current, weld time, and electrode force (which impacts the system's resistance) have a direct effect on the heat generation and nugget growth. As well, other parameters affect other aspects of the process. For example, hold time affects cooling rate, and electrode geometry affects heat distribution and stress near the electrode-sheet interface. Several studies have been conducted to determine how welding and material parameters affect LME cracking severity. Each parameter will be discussed in-turn with respect to how it affects the factors of LME development; particularly stress and temperature of the process.

Thermomechanical Origin of LME Cracks in RSW

It is widely agreed that increasing heat input increases LME severity [14]. Kim et al. [67] showed LME severity increases with increased weld current and time when welding with a standard weld schedule. However, lowering heat input results in a corresponding decrease in LME cracking. Ashiri et al. [72] observed that LME cracking only occurred after a critical level of heat generation was exceeded. Through mathematical modeling of the resistance spot welding process, Ashiri et al. observed that severe tensile stresses at the electrode sheet interface appeared after a critical amount of heat generation. From Section 2.2.3, it is established that the presence of tensile stresses at elevated temperatures will lead to LME in the Fe/Zn system. The work by Ashiri et al. provided an essential pathway to LME mitigation during RSW: process modifications to avoid an LME susceptible thermomechanical state.

Of the three factors responsible for LME (material, stress, and contact with embrittler), reducing LME by manipulating tensile stress during the welding process has been the most common subject of RSW studies. Ashiri et al. [72] used two pulses to avoid a critical amount of heat generation and thus LME cracking. The first pulse was used to form the 4√t minimum nugget diameter with a strong bond around the edge of the nugget. Then a second pulse was used to grow the nugget and control thermal stresses. The two-pulse scheme successfully mitigated LME cracking by reducing thermally induced stresses in the Type B crack location. Current pulsing was also successfully used by Kim et al. [67] to decrease LME. In that work, a pre-current was used in conjunction with a two-pulse welding scheme to reduce LME cracking. However, it should be noted that the pre-welding current pulse only successfully reduced LME if a low pre-welding current pulse was used, relative to the welding current [73]. Although the previous studies broadly attribute the observed decrease in LME to controlling heat input during welding, Wintjes et al. [73] showed that current pulsing decreased LME by the combined effects of stabilizing the Zn in the galvanized coating through interdiffusion with Fe in the steel substrate and controlling the tensile stresses associated with the electrode contact [74]. This was shown by varying pulse distribution in a two-pulse weld. As the length of the first pulse increased, so did the Fe content of the Zn coating which increased the melting temperature of the coating through intermetallic formation. However, if the first pulse was too long, the hot strength of the substrate dropped sufficiently for the electrode to press into the material, leading to LME. This was also seen by Choi et al. [75], who independently investigated on the effect of welding time on LME. Choi et al.

claimed that the increase in observed LME was due to increased heat input, however, Wintjes et al. provided more detail into the specifics on the mechanism leading to LME crack formation.

Bohne et al. [76] investigated the use of extended hold times for LME crack mitigation. With a mix of experimental observations and thermomechanical simulation, it was determined that the use of extended hold times withdrew excess heat from the weld, eliminating tensile stress from thermal shock at electrode release. However, the results from this study indirectly indicate that this method was only successfully reduced Type A cracks, as these cracks form due to the thermal stresses associated with the electrode release. Conversely, Type B cracks form due to the stresses associated with electrode contact as seen in [73,77]. Although this study showed a legitimate methodology for LME reduction, it also gave critical insights into the stress mechanisms for the formation of LME cracks, particularly Type A cracks.

Not surprisingly electrode force also has an influence on tensile force during the welding cycle. Although ironically, increasing electrode force leads to decreased LME severity. This correlation was connected to the associated decrease in heat generation due to improved contact at the faying surface [67,75,77,78]. This is perpetuated by claims from Choi et al. [75] who concluded that the effect of low electrode force on increased contact resistance and heat input is far more significant than the lower mechanical load on the weld surface. However, this only explains the results by Kim et al. and Barthelmie et al. [67,78] who did not control for heat input in their experimental procedure. Conversely, Choi et al. [75,77] increased welding current as they increased welding force so that nugget diameter (thus heat input) was held constant at all force levels. The results of Choi et al. are summarized in Fig. 2-13 which shows increasing LME with decreasing electrode force. By keeping nugget diameter constant, heat generation must have been constant, and therefore it must be concluded that increasing electrode force must decrease LME by a mechanism other than reducing heat input. Choi et al. [75] showed in their thermal simulation that increased electrode force decreases surface temperatures, which they propose reduces LME by reducing the time that the steel substrate is in contact with the liquid Zn.

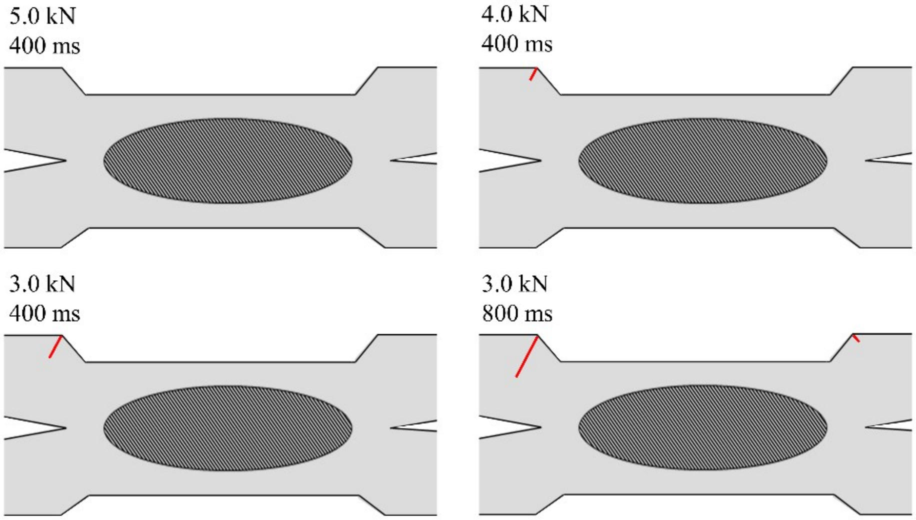

Figure 2-13 *LME cracking increasing with decreasing electrode force (adapted from* [75]*)*

Both Barthelmie et al. [78] and Kim et al. [67] showed that increasing electrode diameter decreases LME. In Barthelmie et al.'s case, a 50% reduction in LME severity was seen. However, it is unclear if all welds in this test were made using the same heat input (and by association nugget size), which needs to be controlled for to conduct a direct comparison [72]. If heat input was not held constant during these studies, the observed reduction in LME cracking may be due to decreased heat input, which is possible as increasing electrode diameter will decrease current density. Murugan et al. [79] found that cracking decreased when using electrodes with radiused tips (as opposed to electrodes with flat contact faces). Furthermore, cracking decreases as the electrode radius increased. Additionally, it was shown that cracking was further reduced when electrode curvature was increased due to a reduction in current density at the edge of the electrode contact area. Temperature and stress were decreased at that location. Although these studies have started to provide insight into how electrode shape contributes to the temperature field during RSW, a comprehensive comparison of distinct electrode geometries is missing from literature.

There have been several different approaches to studying and mitigating LME during RSW. The methods reviewed in this section focused on manipulation of tensile stress and temperature, however other research beyond the scope of the thesis objectives have looked at material susceptibility and contact with liquid Zn. A summary of the approaches to LME mitigation is shown in Fig. 2-14 which is categorized based on the target LME factor with the mechanism of reduction identified. When surveying the literature, it should be noted that all the above changes in the welding parameters (changing current, current pulsing, changing hold time, and changing electrode geometry) affect stresses during the RSW process. As mentioned previously, it was initially thought that the mechanical load of the electrode force was responsible for LME cracking during RSW. After reviewing the present literature, it is unclear if the stresses from the RSW process are driven by thermal or mechanical factors. A more detailed process analysis is required to pinpoint the exact thermomechanical mechanisms responsible for the formation of LME cracks in the distinct regions.

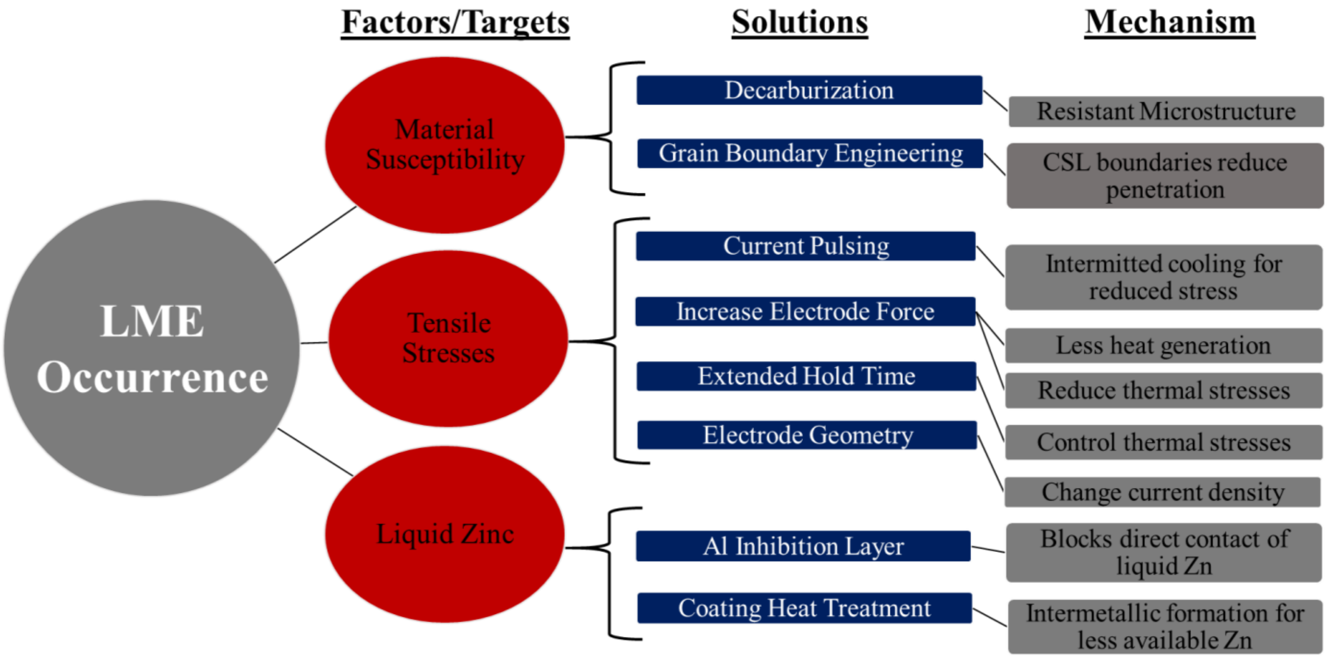

Figure 2-14 *LME reduction methods organized according to targeted factor with the reduction mechanism identified*

Effect of LME Cracks on Joint Performance

The initial consensus in the literature was that LME cracks had no effect on mechanical weld performance [67,80,81], which was widely accepted by industry and academic researchers. However, when examining their methodology, it can be seen these studies did not properly isolate the impact of LME cracks. Work by Kim et al. [67] compared a high current (cracked) case to a low current (crack-free) case but did not control for the effect of nugget size on weld strength (Fig. 2-15). As the high current case had a larger weld, it would be stronger than the smaller nugget case, despite the presence of cracks. This explains the conclusions of the study, which showed an increased strength in the high current (cracked) case. Similarly, Jiang et al. [81] did not make a direct comparison to an equal crack-free sample, although the methodology is not well described. The study carried out by Benlatreche et al. [82] examined a dissimilar weld between a TRIP 1180 and mild steel using tensile shear strength (TSS) testing. During TSS, a welded coupon is pulled by a uniaxial tension tester to create a shear load on the weld joint to evaluate the weld strength. The study concludes that LME had no impact on weld mechanical performance despite LME cracking on the TRIP side, however it should be noted that joints always failed in the mild steel base material which has significantly lower mechanical properties compared to TRIP 1180 (Fig. 2-16). Therefore, it is more correct to say the cracked TRIP1180 weld was stronger than the mild steel base material. However, the results of this study raise an interesting question regarding whether LME affects joint strength in dissimilar welds made of materials with mismatched mechanical properties. Depending on the relative strength of the materials, LME cracking may be innocuous.

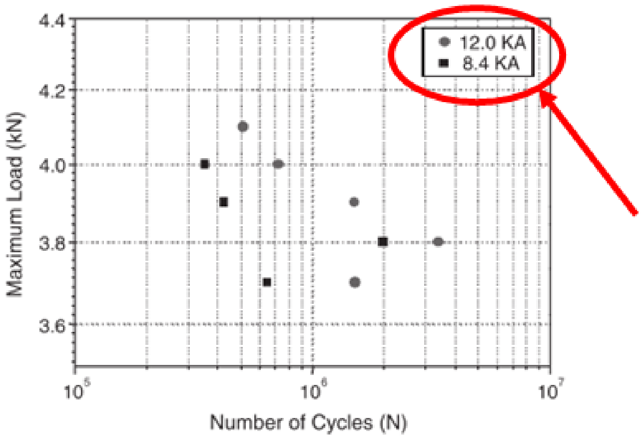

Nugget size increased from 6.70mm to 7.36mm

Figure 2-15 *Inconsistent nugget size used to evaluate mechanical performance* [67]

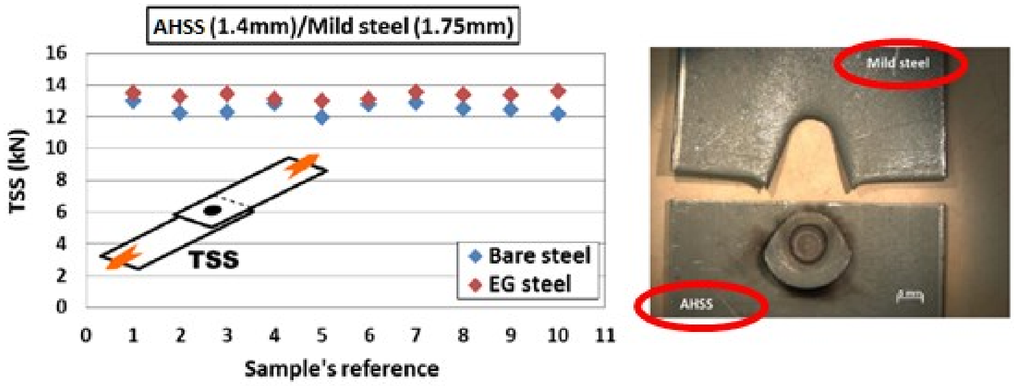

Figure 2-16 *Dissimilar weld case shows fracture to occur in the mild steel side of the joint* [82]

Recent studies with improved methodologies have shown contrasting results. A study carried out on four types of AHSS by Wintjes et al. [70] showed a drastic decrease in weld strength for TRIP 1100 and TRIP 1200 joints, which also featured large and numerous cracks. Conversely, a DP 980 and TRIP 690 steel was also studied, but due to their less severe LME, these welds did not show the same drastic strength loss. Choi et al. [71] observed a severe decrease in mechanical performance in TRIP 1180 joints. However, it is stated that a decrease in performance was only observed for conditions that produced cracks greater than 500 μm. In the case of weld strength, the results were similar to the reports from Wintjes et al. and Choi et al. in that a significant effect was observed in samples containing large cracks. However, samples with medium and short cracks show no large detrimental effect.

Although work is being done to characterize how LME cracking affects joint strength, it is clear there are still many questions. It is unknown whether loss in joint strength is due to loading configuration, LME crack length, or a combination of these two factors. Furthermore, no literature covers the role of location or crack type (A, B, or C) in joint strength loss. More work must be done to characterize the detrimental characteristics of LME cracks so it can be the target of reduction methods. Much more work is needed in this area to define when cracks are innocuous and when they reduce joint strength to understand what the implication of LME cracking on vehicle safety. These characteristics are important to identify to guide the research of the thermomechanical mechanisms in the process responsible for LME. Then, once detrimental characteristics have been defined, they can be targeted using thermomechanical adjustments to the RSW process to suppress the onset mechanism for LME.

Chapter 3

Effect of LME Cracks on Joint Strength

3.1 Overview

There are conflicting reports on the effect of LME cracks on RSW joint performance. Studies have concluded that LME cracks have no impact on joint strength or fatigue life [67,82], however more recent work has shown LME cracks to be detrimental in certain cases [71]. This chapter discusses the effect of LME cracks on RSW joint strength and determines the factors that lead to a detrimental effect. Tensile shear testing on coated (cracked) and uncoated (no cracks) welds was carried out to isolate the impact of LME cracks, which revealed LME cracks to be part of the fracture path and degradation of joint strength but only in certain cases. To study the effect of LME crack location on strength a customized welding electrode that controlled LME crack formation was used. Overall, this chapter signifies the critical crack characteristics for strength loss and provides insight into the disagreement in the current literature.

3.2 Background

The tensile shear test is a standard testing method for evaluating static weld strength. This is due to its simplicity and because most welded structures are designed to carry tensile shear loads [83]. The peak load obtained from the force displacement curve is commonly used to describe the weld's strength [83–86]. Failure occurs in two modes: interfacial and button pull-out. In interfacial failure, a crack propagates through the fusion zone, while during pull-out, the nugget is completely pulled from the sheets. Spot welds that fail in pull-out mode are preferred due to their higher energy absorption compared to interfacial failure [86–89].

Currently, it is unclear whether LME cracks have an impact on mechanical performance [14]. A study by Choi et. al showed a decrease in mechanical performance in LME cracked welds [71]. In contrast, several studies have shown that LME cracks have no influence on the mechanical behaviour of spot welds [67,81,90]. However, the studies showing no detrimental effect either focused on materials with low susceptibility to LME, dissimilar welds, or in comparison between high and low welding current conditions. In addition, there is no quantitative comparison between welds in a Zn coated steel to those in an uncoated steel, accounting for the effect of nugget size on strength. Furthermore, no studies have been conducted to determine the relationship crack location plays in decreasing weld strength, or lack thereof. Current studies have only focused on crack size as a measurement of crack severity and only related crack size to loss of mechanical strength. Since the weld nugget is not loaded uniformly during tensile lap shear testing [84,87], it is essential to understand the relationship between crack location and weld strength behaviour.

In this study, several Zn coated AHSS with varying microstructures were welded and tensile lap shear tests were carried out on both coated and uncoated samples to determine how LME cracking affects RSW joints. In addition, a fractography study was carried out to locate LME cracks on the fracture surface and identify a detrimental area for LME crack location in lap shear loading. Furthermore, samples with LME cracks in various locations on the weld surface were compared to uncoated (not cracked) samples, and a relationship between crack location and decrease in weld strength was observed. A finite element method (FEM) model was used to calculate the stress field of the lap shear loading in both the crack and uncrack conditions to provide further insight into the experimental observations.

3.3 Experimental Procedure

Welded Sample Preparation

In this study, galvanized (GI) DP 980, TRIP 690 and TRIP 1100 steels were examined due to their industrial relevance. The chemical compositions and mechanical properties can be found in Table 3-1 and Table 3-2 respectively. Materials were welded in both their coated and uncoated conditions to isolate the effect of LME cracks on strength. Uncoated materials were obtained by stripping the Zn coating from the examined materials. The coating was removed from the sheets by submerging the samples in a solution of 50% hydrochloric acid and 50% water, for 10 to 12 seconds.

Table 3-1 *AHSS coating thickness and material chemistry*

Steel Grade	Top Coating (g/m^2)	Bottom Coating (g/m^2)	C (wt%)	Mn (wt%)	Si (wt%)	Cr (wt%)	Mo (wt%)	Al (wt%)
DP 980	60	55	0.15	1.50	0.30	0.22	0.27	0.04
TRIP 690	58	69	0.20	1.66	0.40	0.04	-	1.31
TRIP 1100	58	70	0.20	2.24	1.50	0.03	-	-

Table 3-2 *AHSS mechanical properties*

Steel Grade	Thickness (mm)	Yield Strength (MPa)	Tensile Strength (MPa)	% Elongation
DP 980	1.2	600	980	13.8
TRIP 690	1.2	445	690	20.7
TRIP 1100	1.6	861	1100	14.5

Samples were welded using a medium frequency pedestal direct current resistance spot welder with a Rexroth controller. To remove surface contamination, the coupons were cleaned with ethanol prior to welding. Since it has been shown that LME is more prominent at high welding currents [14,67], all welds in the coated samples were made at the expulsion current (I_{max}), which is defined as the minimum current where three consecutive welds show expulsion. I_{max} was determined for each material stack up and used as the welding current. The remaining parameters including, welding time, force, and hold time were selected in accordance with AWS D8.9 and are listed in Table 3-3 [91].

Table 3-3 *Welding schedules for each AHSS according to AWS standard* [91]

Steel Grade	Welding Current (kA)	Electrode Dia. (mm)	Force (kN)	Weld Time (ms)	Hold Time (ms)
DP980	10	6.0	4.0	250	167
TRIP690	11	6.0	3.6	250	167
TRIP1100	11	7.0	5.5	200 – 33 – 200	167

The welding currents used for the uncoated samples were chosen so that they would produce the same nugget size as measured at I_{max} in the coated samples. Nugget size for both conditions is 7.7 mm, 6.5 mm, and 6.6 mm for the TRIP 1100, TRIP 690 and DP 980 respectively. Using the same nugget size for coated and uncoated samples ensures any difference in strength is not due to a difference in weld size, which is identified as the largest influence on weld strength [92]. Although the nugget size is different for each material, the coated weld was compared to their uncoated counterpart, which has the same nugget size. This allows for a comparison of strength loss at I_{max} across the materials studied. Additionally, welded samples of the coated condition were cross-sectioned to examine LME crack size across the different materials. The cross-section cutting was selected to intersect the most severe surface cracks and LME crack depth was measured as the straight-line distance from the opening to the root. Further details on the LME crack measurement procedure can be found in [93]. The samples were prepared using standard metallographic techniques and cracks were measured using ImageJ software.

Location Sample Preparation

To investigate the effect of location, controlled LME cracks were introduced into the TRIP 1100 material (Table 3-1) by using specially modified upper electrodes. Dome shaped electrodes with an original radius of 7 mm were modified by machining their contact face. The electrode was machined into the desired geometry by milling the top surface at an angle of 1° as pictured in Fig. 3-1. The custom electrode cap geometry creates a pressure concentration on the edge of the electrode, therefore inducing formation of LME cracks in that location. By rotating the electrode tip, LME cracks can be obtained in different desired locations. Crack locations are separated into three categories to compare their sensitivity on mechanical performance. These locations are labelled using an angle system with respect to the loading direction in lap shear test. The angles of 0°, 90°, and 180° (see Fig. 3-2) are used to identify the location of cracks.

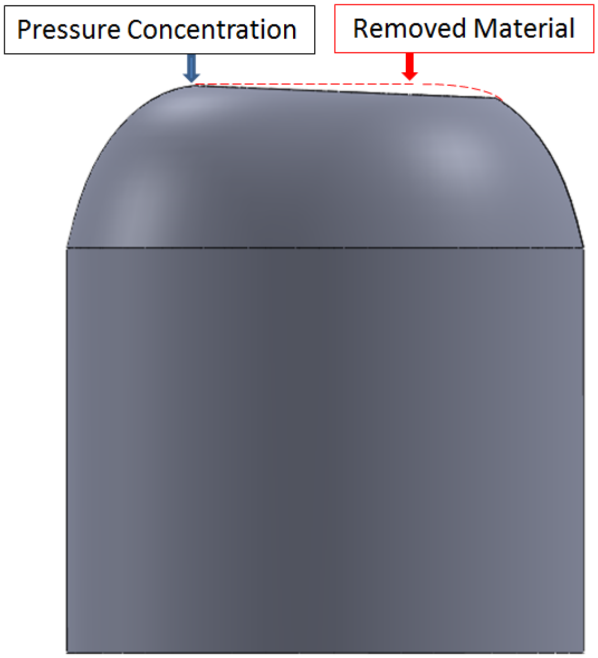

Figure 3-1 *Schematic of modified electrode cap to promote local formation of LME cracks*

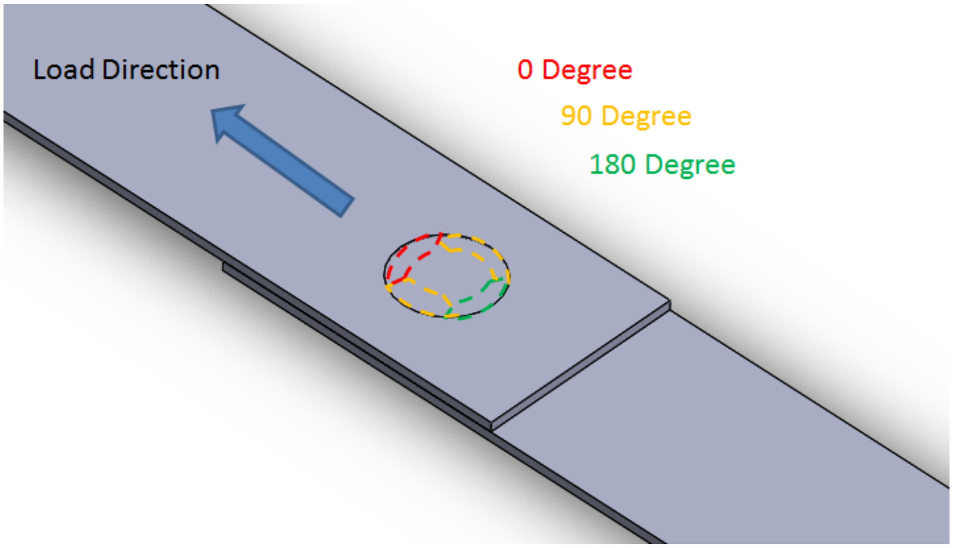

Figure 3-2 *Illustration of lap shear samples with LME crack location cases highlighted*

To further promote formation of LME cracks, high welding currents are used since it has been shown that LME is more prominent at high currents [67]. All welds in the coated samples were made at I_{max}. The welding currents used for the uncoated samples were chosen so that they would produce the same nugget size as measured in the coated samples. A nugget size of ~7.3 mm was used for both conditions. The slight variation in nugget compared to the strength study is likely due to the modification of the electrode face. Using the same nugget size for coated and uncoated samples ensures any difference in strength is not due to a difference in weld size, which is identified as the largest influence on weld strength [92]. The remaining parameters including: welding time, force, and hold time were selected in accordance with AWS D8.9 and are listed in Table 3-2 [91].

Lap Shear Testing

Tensile lap shear testing was carried out using an Instron Model 4206 tensile tester. Fig. 3-3 shows an illustration of the lap shear sample's geometry. The overlap was determined to meet the minimum value for lap shear tensile testing given the geometry of the samples [94]. Six samples for each condition were tested at a cross-head speed of 2 mm/min until failure. The change in strength between welds made in the coated and uncoated samples at each electrode pressure orientation is normalized against the strength of the welds in the uncoated material. The change in strength is defined as the strength of weld in the uncoated sample subtracted from the strength of the weld in the coated sample (a negative change in strength indicates the strength of the welds in the coated coupons are lower than those in the uncoated coupons).

The fracture surfaces from the lap shear tensile tests were examined using a field-emission scanning electron microscope (FE-SEM), along with energy dispersive x-ray spectroscopy (EDX) to identify high Zn concentrations. Fractured tensile samples were also cross sectioned and prepared using through conventional procedures, i.e. mounting in conductive epoxy resin (Polyfast), grinding with SiC sandpaper up to 1200 grit, polishing with 1 μm diamond dust, and

5% Nital etch to allow for clear observation with the FE-SEM and EDX. Lower magnification images of the fracture cross sections were taken with an optical microscope and stereo microscope.

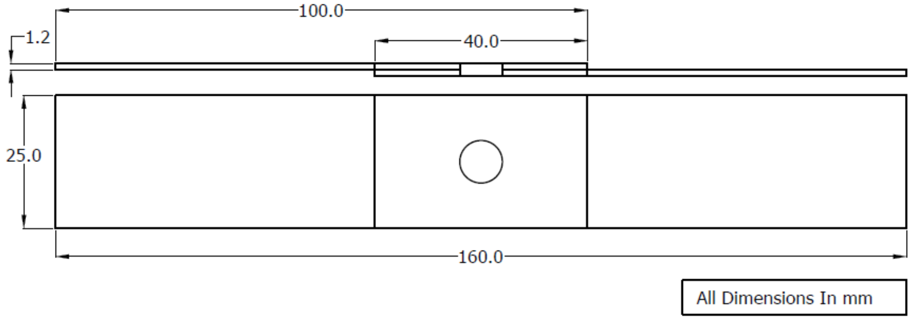

Figure 3-3 *Schematic of lap shear coupons*

Finite Element Method Model

A FEM model of the resistance spot welded lap shear test was also created to study how LME cracks affected stress distribution and material behaviour during testing. The model was utilized to understand the effects of a crack on the stress fields during linear elastic loading of the lap shear sample. In addition, the loading of the crack was examined in different locations in the weld area and was compared with the experimental results.

The FEM model was constructed using solid 8-node elements. In order to reduce computational time and cost, the unnecessary geometry which would be inside the tensile grips was removed. The boundary conditions were applied to the geometry to simulate the loading and constraints of the tensile lap shear testing. One end was fixed in place, while a tensile load was applied to the other end. For the purpose of this study, a static loading case was modeled. Since the model only operates in the linear elastic region, the only material properties needed are the elastic modulus and Poisson's ratio for steel. For this model a Poisson's ratio of 0.33 and an elastic modulus of 200.5 GPA [95] were used. The geometry was appropriately partitioned to produce an efficient grid generation of points which is commonly referred to as a mesh. A mesh of hexahedron elements was chosen since they suit the geometry and are computational efficient. A mesh convergence study was carried out to confirm the stresses in the model were not a function of mesh size (Fig. 3-4). The final mesh size used for the study produced 300,000 elements.

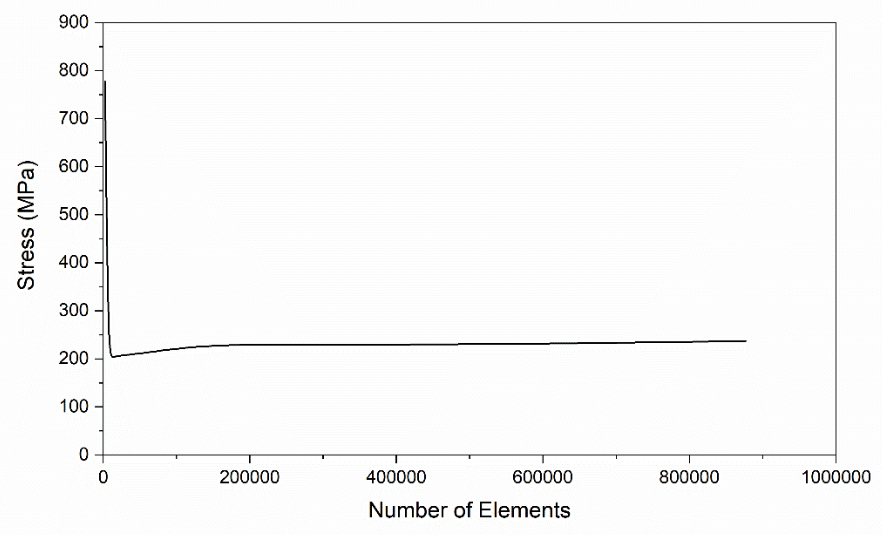

Figure 3-4 *Mesh convergence study at a node of interest, showing stress becomes independent of mesh size*

A crack is a displacement discontinuity in the geometry. Attempting to model such discontinuities within the geometry's mesh can be difficult to simulate and often exhibits poor results. In the case of a crack, a complex mesh in the crack region is needed and the concern of stress singularities at the crack tip give uncertain results. However, extended finite element method (XFEM) allows cracks and other discontinuities to be accurately modelled with the addition of enrichment functions to the classical FEM displacement equations [96]. These enrichment terms do not affect the topography of the mesh and allow the crack to be modelled independent of the mesh. These terms depend on the geometry of the crack, which is described with the technique of level sets.

The LME crack was modelled as a geometric discontinuity in the 3D lap shear sample through XFEM. The crack geometry was taken from typical LME cracks found in TRIP 1100 welded lab samples. A crack length of 400 μm was used. The crack was placed and studied in various locations matching the locations from the experimental set up.

3.4 Results and Discussion

Effect on Lap Shear Strength

The results of TRIP 1100 showed a 43.6% decrease in peak load between the coated and uncoated samples (see Fig. 3-5 and Table 3-4). The large decrease in lap shear strength is unexpected and is in contrast to previous LME work [67,81,90]. Contrary to the results of TRIP 1100, the welds in DP 980 and TRIP 690 did not show the same decrease in strength between the uncoated and coated samples. The TRIP 690 showed no statistical difference in strength between the two conditions. The 7.5% decrease in strength between the coated and uncoated DP 980 welds was statistically significant but is not as substantial as the loss from the TRIP 1100 welds. Overall, DP 980 showed a loss of strength, but not nearly to the same degree as TRIP 1100.

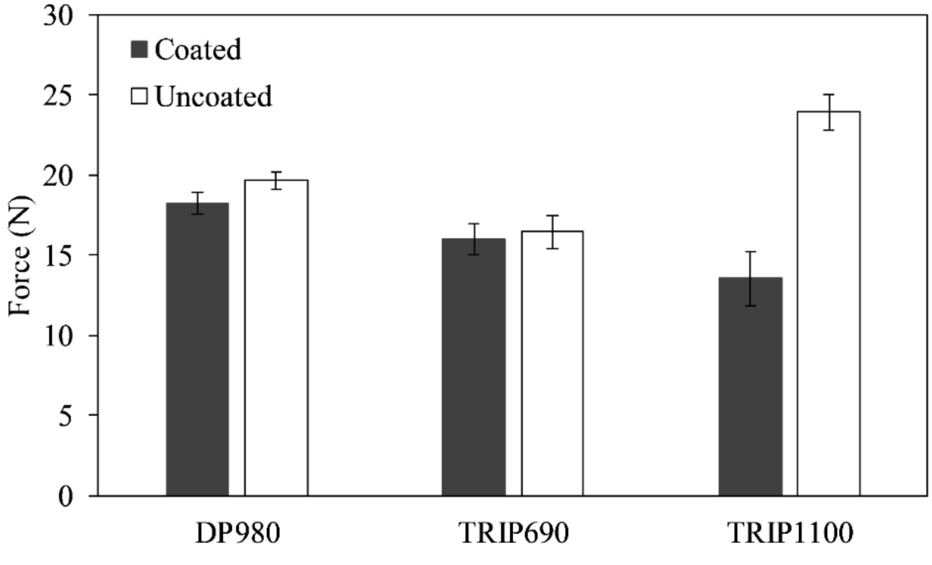

Figure 3-5 *Mean lap shear strength for each material, coated and uncoated (6 samples per case)*

Table 3-4 *Comparison of lap shear test results for each case (6 samples per case)*

Steel Grade	Mean Lap Shear Strength (kN)	95% Confidence Interval	Decrease in coated sample
DP980 – Uncoated	19.62	± 0.55	7.1%
DP980 – Coated	18.24	± 0.68	
TRIP690 – Uncoated	16.45	± 1.01	2.6%
TRIP690 – Coated	16.02	± 0.96	
TRIP1100 – Uncoated	23.91	± 1.11	43.5%
TRIP1100 – Coated	13.51	± 1.73	

Given that the nugget diameter between the coated and uncoated samples is consistent, which is identified as the largest influence on strength [92], the difference in peak load for TRIP 1100 is unexpected. Other factors must play a significant role for such a large loss of strength to occur. One such factor could be the number, size, and location the of LME cracks; for example, it is possible that TRIP 1100 has large cracks in the location of highest stress during testing. Conversely, DP 980 and TRIP 690 possibly develop smaller cracks and there is less chance to have significant cracks in critical areas. The loss of strength in TRIP 1100 is likely due to the frequency at which large cracks develop, which are more probable to develop in a load bearing area of the weld.

The analysis of crack size and distribution shows TRIP 1100 develops the greatest number of cracks above 400 μm compared to welds of the other materials, as seen in Fig. 3-6. DP 980 and TRIP 690 do not develop nearly as many large cracks (>400 μm) since the cracks that form are mostly small cracks (<100 μm). There is a considerable difference in the distribution of crack size between TRIP 1100 and the other materials. Since TRIP 1100 welds develop the largest LME cracks most often among the materials tested, it is also reasonable that LME will have the largest effect on strength loss in TRIP 1100 welds.

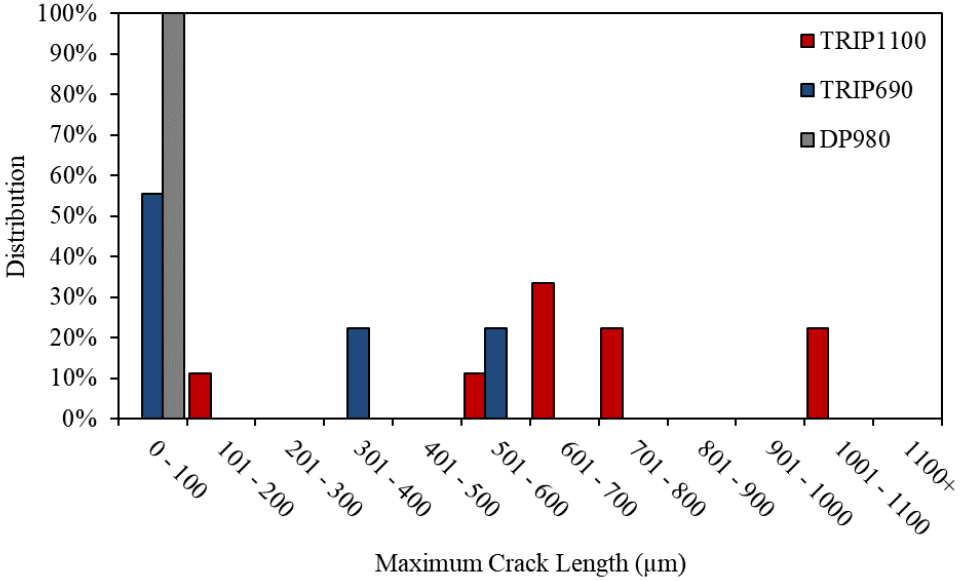

Figure 3-6 *Distribution of maximum LME crack length from each sample in the coated condition for all materials (9 samples per material)*

The results of the tensile lap shear test suggest the LME cracks can play a role in the static strength of spot welds. However, it is dependent on material susceptibility and crack development. Since a decrease in weld strength was observed for coated TRIP 1100, which was also observed to be LME prone, further work must be done to confirm that LME is responsible for the decrease in strength. To do this, the fracture surfaces of the fractured welds were examined after tensile lap shear testing.

The weld nuggets and adjacent sheet metal fractures of TRIP 1100 were cross sectioned and examined. The uncoated sample showed a fracture path that is consistent with what is seen in button pull out according to literature [86]. An image showing the cross section of the coated and uncoated fracture can be seen in Fig 3-7. In Fig. 3-7(b) and Fig. 3-7(c) the coated sample appears to show a different morphology towards the top and bottom edge of the sample, as the fracture sharply changes directions. This area was more closely examined using the SEM and EDX elemental analysis. The results show areas of high Zn concentration along the fracture surface. EDX elemental maps and point analysis are shown in Fig. 3-8 and Table 3-5 respectively identify Zn on the fracture surface, which is a distinctive characteristic of LME cracks [97,98]. With the abrupt change in fracture path and the results of the EDX analysis, it is believed that while cracks initiated at the sheet interface from lap shear testing, the LME cracks simultaneously grew until both cracks met and caused final fracture.

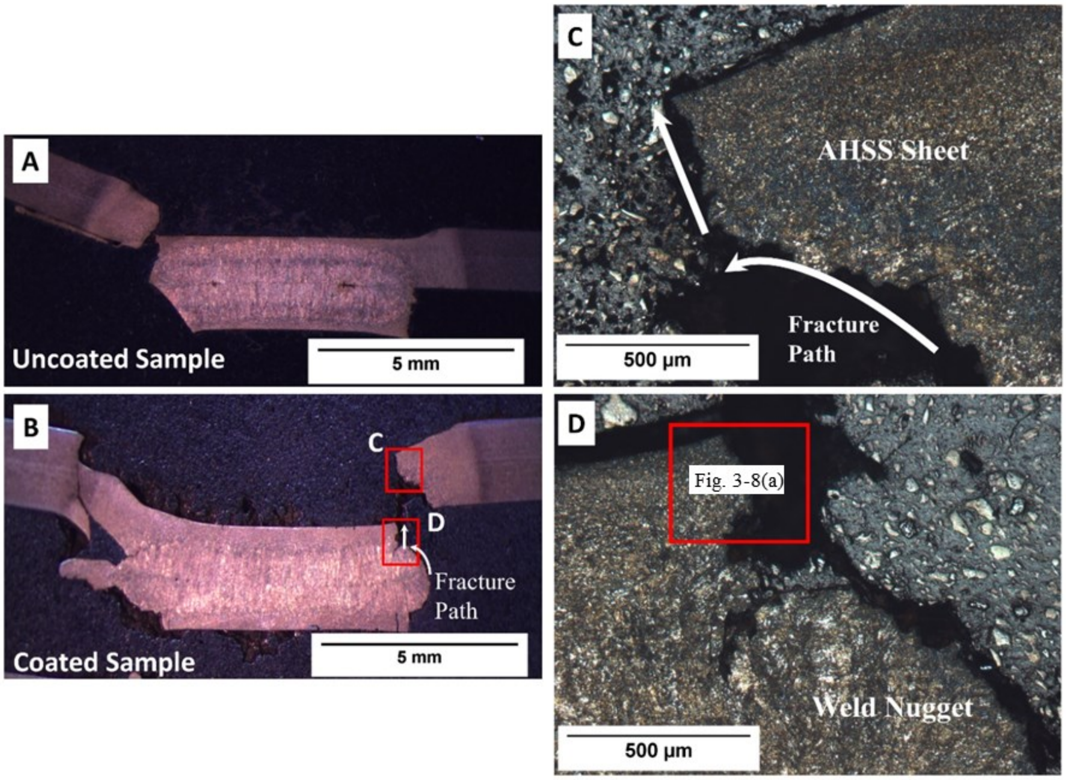

Figure 3-7 *TRIP 1100 nugget and sheet fracture cross sections (A) image of uncoated sample cross section showing the typical fracture morphology for button-pullout (B) image of coated sample cross section showing the unusual shape change in fracture direction (C) high magnification image of fracture path in coated sample sheet fracture (D) high magnification image of coated sample in nugget fracture showing similar fracture path*

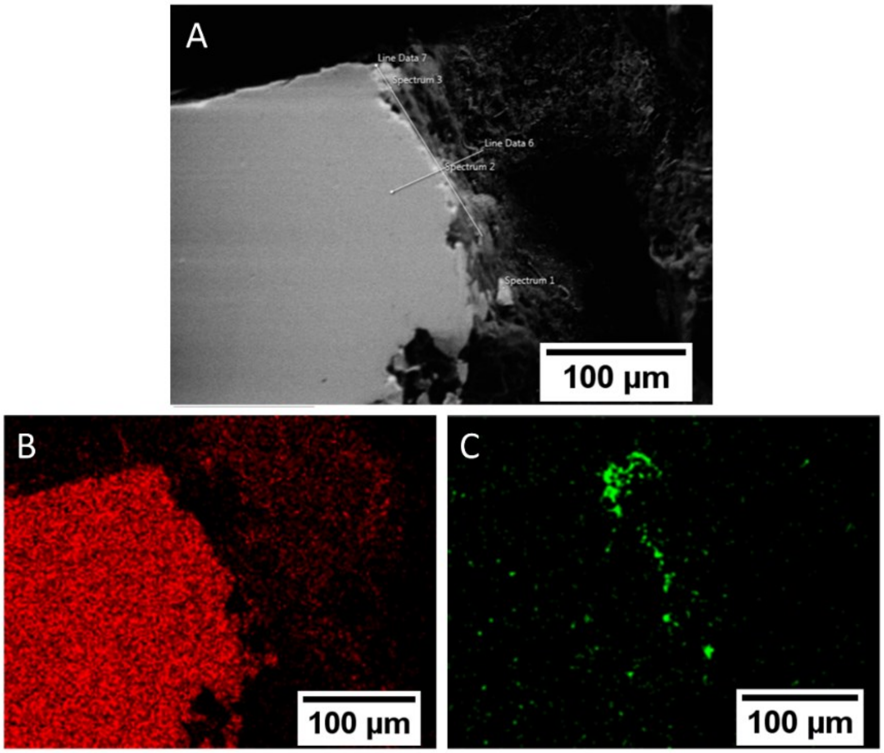

Figure 3-8 *(a) Coated TRIP 1100 SEM image of crack area (b) EDX map for Fe (c) EDX map for Zn showing high concentrations on fracture surface*

Table 3-5 *EDX spectrum results from Fig. 3-8(a)*

Spectrum	Zn Wt%	Variance
Spectrum 1	24.18	0.48
Spectrum 2	39.78	0.61
Spectrum 3	56.39	0.98

Observing the growth of the LME cracks before and after testing is a plain indication of their role in in the sample's fracture. Images of TRIP 1100 LME cracks on the weld surface prior to and post testing are shown in Fig. 3-9(a) and 3-9(b) respectively. The clear propagation of the LME cracks and their growth into the fracture path shows they contributed to the observed loss of strength in the TRIP 1100 samples. Conversely, LME cracks in the centre of the sample appear to be unchanged through the tensile test. Since they are not located in an area loaded during lap shear testing [87,88], they did not contribute to the loss in strength. The cracks are not oriented in way that would allow them to grow or assist in nugget pull-out failure. For LME cracks to have an influence on weld strength, they must be in the periphery of the electrode indentation and be oriented in a circumferential fashion. Thus, the periphery and shoulder of the electrode indention (Type B) can be labelled as the critical area for LME development.

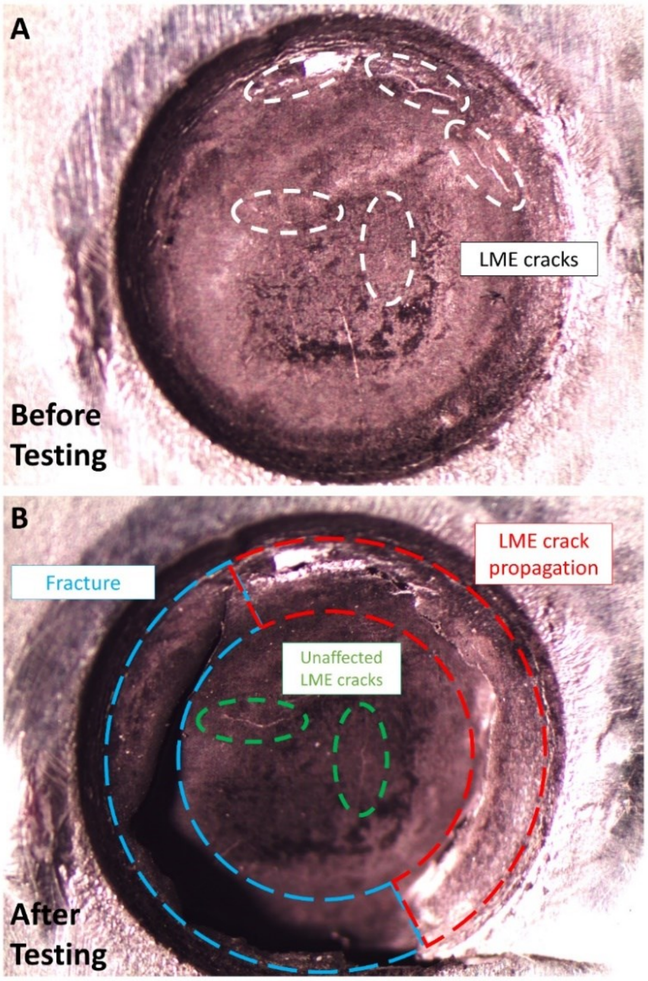

Figure 3-9 *TRIP1100 weld surface (A) surface before lap shear testing showing the location of numerous LME cracks (B) weld surface after lap shear testing showing the growth and propagation of LME cracks in red, the fracture purely from lap shear testing in blue, and the LME cracks that were not involved with fracture in green*

The results showed a significant amount of Zn on the fracture surface, meaning that LME cracks were part of the fracture mechanism during lap shear testing. Zn on the fracture surface is a standard indication of LME cracks [97,98]. The change of fracture morphology in the area where LME cracks are known to form [97] also points towards the involvement of LME cracks. Furthermore, the results imply LME cracks must be in a specific location and orientation to influence the stress field during lap shear testing. LME cracks that develop in the centre of the weld and do not affect lap shear tensile strength. In addition, the analysis of the maximum crack length distribution indicates that LME cracks exceeding 400 μm need to frequently be formed for there to be an impact on joint strength. The insights from this study are essential to the overall framework of LME during RSW. The identification of detrimental cracks is needed as researchers look towards process adjustment for LME reduction. However, a more detailed inspection of LME cracks in the weld shoulder is needed as the weld is not uniformly loaded during lap shear testing.

Impact of Location

LME crack location along the weld periphery was further investigated to determine its significance to strength loss. The results of the lap shear testing showed varying degrees of strength decrease with crack location. The 0°, 90°, 180° cases showed a 42.2%, 19.7% and 7.8% decrease in strength respectively, in comparison to their uncoated counter parts. Although all the control cases are uncoated, they may not exhibit the same strength due to asymmetrical electrode in the welding process. The comparison between Zn coated samples and uncoated samples can be seen in Fig. 3-10. Given that all samples are compared against their uncoated counterparts, the only difference between the three cases is the crack orientation. The results of the lap shear testing show there is a relationship between crack location and strength loss, in addition to the previously observed relationship to crack length. A plot comparing the normalized change in strength to crack location is shown in Fig. 3-11, which shows the crack is the most detrimental at the 0° position and its effect on strength decreases as the crack moves towards the opposite position on the weld surface.

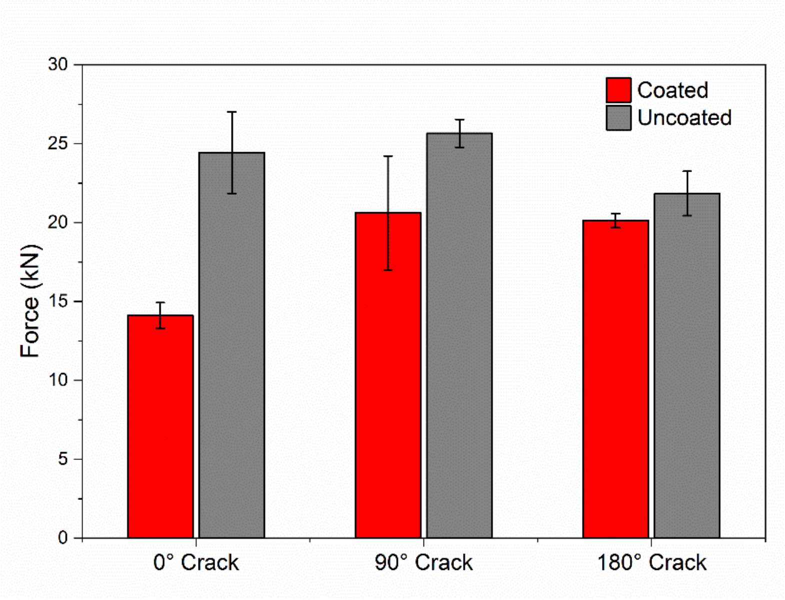

Figure 3-10 *Mean TRIP 1100 lap shear strength for each crack location from experimental work (6 samples per case)*

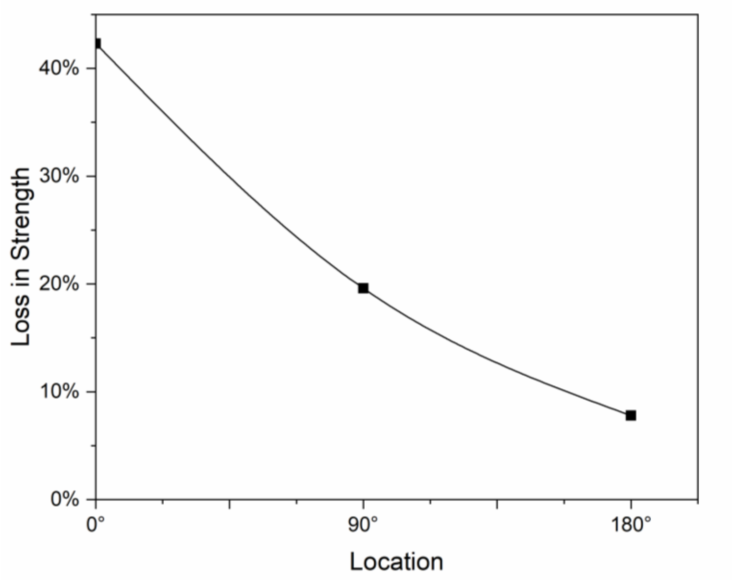

Figure 3-11 *Relationship between loss in strength and crack location relative to the axis of tension*

By examining the weld surface of each crack orientation case it is clear the crack location affects its influence on fracture. Fig. 3-12 shows before and after testing images of the weld surface for each case. When looking at Fig. 3-12(a), it is clear that the fracture grows at the LME crack and propagates along the weld edge. Lap shear fractures are known to initiate at the 0° location [84,85,87]. The 0° case can be labelled as the most critical, as it has been shown to exhibit the largest loss in strength and has the largest influence over fracture development. The 90° case shown in Fig. 3-12(b) shows a less severe case. It can be seen that fracture initiated in the 0° position but propagated to join the crack at the 90° position, along with several other directions. Although the fracture was influenced by the presence of the crack, it did not have the same clear impact on the weld fracture, which is reflected by the lower loss in strength. Finally, the 180° case proved to be the least severe, as the fracture developed independently from the presence of the crack and played no large role in its growth. This is once again reflected in the strength results with the 180° case showing a miniscule decrease in strength with no statistical significance. Altogether, the loss in strength appears to correlate to the role of the LME crack in fracture formation and path.

The current literature surrounding LME during RSW has used maximum crack length as the parameter to describe crack severity [71]. However, with the findings of this study, location plays a role in the strength loss from LME cracks. Crack location must also be considered when discussing the crack severity of a weld. Even though current literature has shown the significance of crack length, a crack of considerable length will not be detrimental if it is not stressed during loading. Both crack characteristics must be taken into account when designing RSW process adjustments for reduced LME.

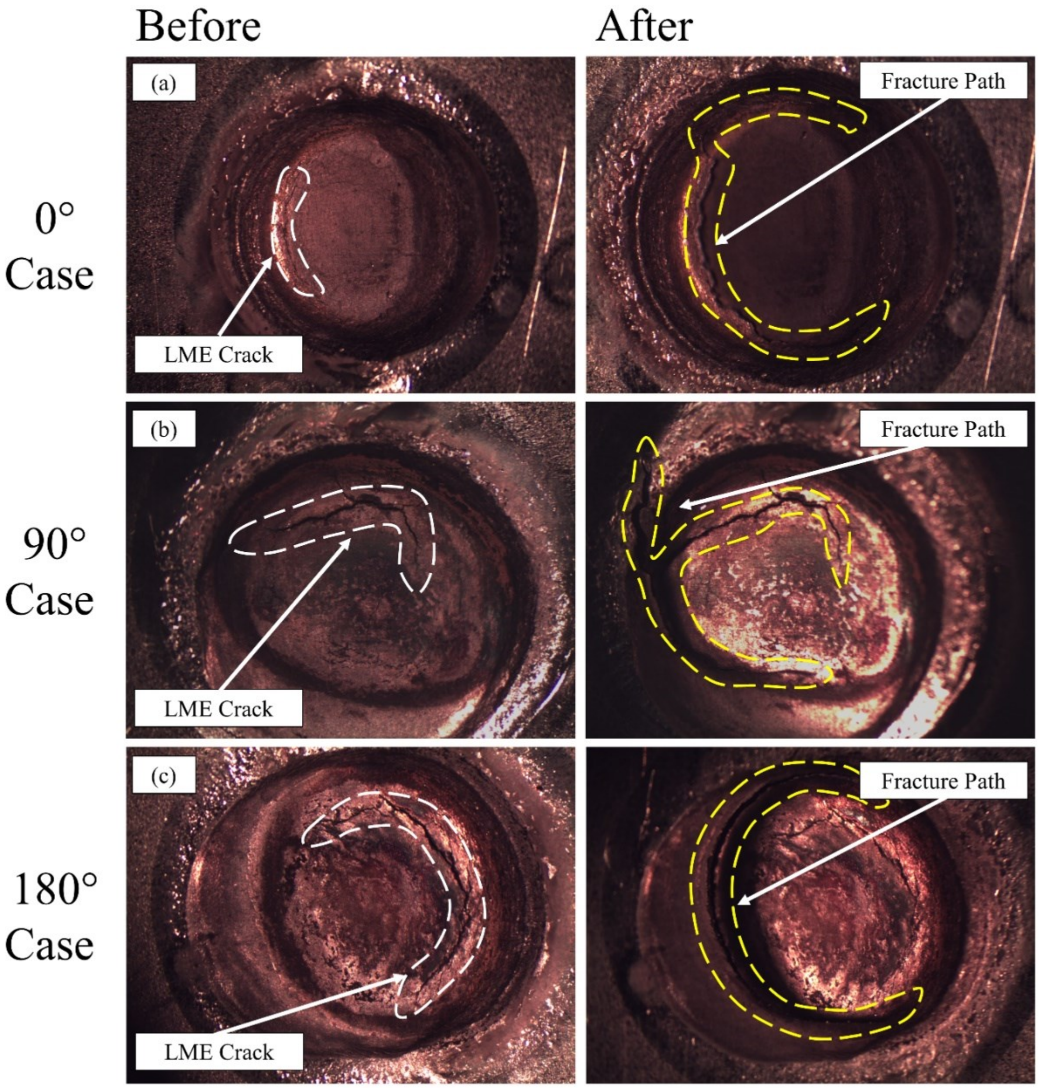

Figure 3-12 *Coated TRIP1100 lap shear surface fractures before and after testing (a) images of the 0° case showing the growth and propagation of the LME crack into the fracture path (b) images of the 90° case showing the partial overlap between LME crack and fracture path (c) images of the 180° case showing the fracture path developed independent of the LME crack*

The lap shear testing shows a relationship between loss in strength and crack location. Although it is clear this relationship exists, a FEM model is used to further understand and explain the variation in strength loss with crack location. The surface and internal geometry stress fields of the sample during lap shear testing were examined by FEM to explain the experimental results. A sectional view showing the internal stresses in the weld is shown in Fig. 3-13. Fig. 3-13(b), (c), (d), and (f) show the no crack, 0°, 180°, and 90° cases respectively. The stress fields for the no crack case match what is reported in literature for nugget loading during lap shear testing [84]. The highest stresses are found at the sheet interfaces as is commonly described. A crack on the surface of this area alters the shape of the stress field and amplifies the peak stress. Fig. 3-13(c) shows the effects of the LME crack in this location, penetrating 400 µm into the material thickness direction. The sample's loading is very sensitive to the crack's presence, since the crack is large enough to penetrate into the high stress bands and is located in a highly loaded area. In contrast, a crack located on the opposite side (the 180° case) would not have any impact on the internal stress fields. From Fig. 3-13(d) it can be seen the crack does not significantly affect the shape or magnitude of the stress fields. The crack is located in a region that is not initially loaded during lap shear testing. Lastly, in Fig. 3-13(f) the influence of the 90° crack location on the stress field is shown. It can be seen the crack has no detrimental impact, and the negative effects seen in lap shear testing come from whether the fracture path intersects the existing LME crack (as seen in Fig. 3-12(b)). The dependency on fracture path in the 90° case explains the large strength loss variability seen in Fig. 3-10. These results provide an explanation for the trends seen in the experimental crack location study.

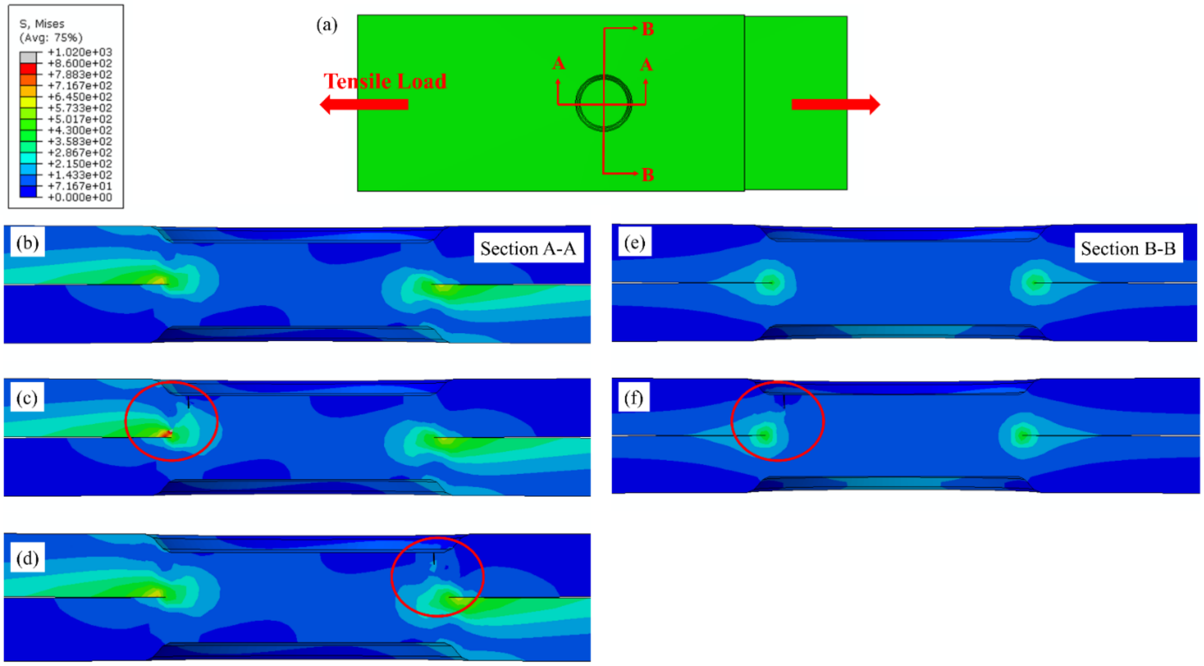

Figure 3-13 *Stress fields for lap shear testing with varying crack locations. Cracks are superimposed on the stress fields for visual purposes only. (a) Top view of the lap shear sample showing the axis of loading and cross sectional locations (b) cross section A-A with no crack showing the internal stress field (c) cross section A-A and elevated stress field of the sample with a crack in the 0 location (d) cross section A-A and stress field showing miniscule effects of the crack located in 180 position (e) cross section B-B with no crack showing the internal stress field (f) cross section B-B and stress field showing the crack in the 90 location with little impact on the stress field*

The results of the XFEM model show that a crack located in an unloaded region of the weld nugget does not affect the stress field in the loaded weldment, so it will not have an effect on failure strength. The results also give an understanding of how cracks affect the stress field during lap shear loading. Overall, detrimental LME cracks should be characterized according to their location in addition to size as shown in 3.4.1. The size of LME cracks depends on many factors including the RSW process and metallurgical factors from material susceptibility. However, the location of LME cracks depends solely on the process since the onset of LME requires the stress and elevated temperatures provided by RSW. Therefore, the thermomechanical mechanisms responsible for the onset of LME in RSW should be investigated to reduce detrimental LME cracking. From the insights provided by this study, if location can be controlled and LME crack sized reduced, detrimental LME cracks can be mitigated.

3.5 Summary

This chapter studied the under reported critical characteristics of LME cracks and provided new insight into the contradictions in literature about the effect of LME cracks on RSW joint strength. LME cracks can reduce joint strength depending on their location and size. The following conclusions can be drawn:

(a) The results of the lap shear test showed a 43.5% loss in strength in the TRIP1100, which was highly susceptible to LME cracking. Examination of the fracture surface showed LME cracks in the outer portion of the weld were part of the fracture path, contributing to the loss in strength. LME cracks located in the centre of the weld did not contribute to the fracture.

(b) A relationship exists between LME crack location and loss of lap shear strength. The variation in loss of strength with crack location can be explained by the increased intensity of the stress fields surrounding the crack.

(c) Less LME susceptible AHSS did not exhibit strength loss due to the lack of large LME cracks and less likelihood of cracks occurring in critical locations.

(d) Detrimental LME cracks have been characterized according to both crack size and location. LME crack mitigation techniques should target LME cracks based on both these criteria, particularly location where the RSW process is solely responsible

Chapter 4

LME Crack Formation and Reduction in Resistance Spot Welding

4.1 Overview

It has been determined that both LME crack size and location are important characteristics for evaluating detrimental LME cracks. However, the formation mechanisms responsible for the development of LME cracks during RSW have not clearly been established. In order to mitigate LME cracks, the mechanisms leading to crack formation must be identified and targeted. This chapter investigates the resistance spot welding process and pinpoints the mechanistic cause for LME in RSW. Process parameters are adjusted by way of input current waveform, electrode geometry and angular electrode alignment which revealed that LME cracks in different regions of the weld have distinct thermomechanical formation mechanisms. The observations highlight the significance of temperature and stress state for the onset of LME in RSW. Furthermore, the results from this chapter provide insight into previous observations of LME crack occurrence in RSW from literature.

4.2 Background

As discussed in Chapter 2, there have been several studies focused on RSW process modifications for LME reduction. In general, increasing heat input has been observed to worsen LME. However, the precise process mechanisms to leading LME formation still eludes researchers. Given that

LME crack location was established to have a significant impact on strength loss, the formation mechanism of the distinct crack types (Type A: weld centre and Type B: weld shoulder) needs to be identified and eliminated through RSW process adjustments.

For LME to occur, three factors must be present: liquid Zn must be in direct contact with solid steel, the substrate must have a susceptible microstructure, and the substrate must be under tensile stresses [67,72]. The welding process causes two of these factors (liquid Zn and tensile stresses) to occur. Therefore, the welding parameters have a large influence on LME crack formation during RSW. Previous work carried out by Beal et al. suggested modification to the RSW process parameters to avoid activating LME [16]. However, the link between RSW process parameters and stresses developed during the process is unclear. A recent studies by Choi et al. [99] and Bohne et al. [100] found that the instant the electrodes are released, large tensile stress developed due to the sudden change in cooling rate. These studies imply the management of the cooling rate discontinuity can result in decreased LME severity.

Another process aspect found to be closely related to the occurrence of LME is the RSW electrode. Barthelmie et al. [78] showed that using a larger electrode face diameter reduced cracks by 50%. Similar results were observed by Sierlinger et al. [101] who used an increased electrode face diameter to reduce LME cracking. Likewise, Kim et al. [67] observed LME severity decreased with increasing electrode diameter. However, from these studies, the role the electrode plays in LME crack formation remains unclear. Murugan et al. [79] also found that cracking decreased with increasing electrode radius. Additionally, it was shown that cracking was further reduced when electrode curvature was increased due to a reduction in current density at the edge of the electrode contact area. Temperature and stress were decreased at that location.

This study investigated the formation of LME cracks in the RSW process in detail, building on previous literature while also providing new insights into the process mechanisms leading to LME. The identified mechanisms can then be used as the foundation for LME reduction techniques. The thermal shock at electrode release was investigated with weld process adjustments beyond extended hold times. Additionally, the key role of RSW electrodes was examined through a direct comparison of electrode geometries. The temperature and stress effects of the electrode were explored using both experimental methods and commercial welding simulation software Sysweld®. Finally, the study examined the role of external sources of stress and distortion by way of angular electrode misalignment. The external application of mechanical factors further identified the causes of LME during RSW.

4.3 Experimental Procedure

Sample Preparation & LME Quantification

In this chapter, the highly LME susceptible TRIP 1100 AHSS listed in Table 3-1 was studied exclusively. This was due to the material's high sensitivity to LME occurrence and the material's industrial relevance. Resistance spot welding was completed using a trans-gun direct current spot welding machine mounted on a 6-axis robot arm. The electrode gun is C type clamp gun with servo-controlled electrode force and Rexroth welding controller.

Samples for LME observation were prepared through conventional procedures, i.e. mounting in conductive epoxy resin (Polyfast), grinding with SiC sandpaper up to 1200 grit, polishing with 1 μm diamond dust to allow for clear observation and measurement of LME cracking in the weld area. LME cracks were observed and measured using an optical microscope (Oxford BX51M). LME severity was quantified from crack measurements from welded samples using the LME crack index [102]. Measurements were taken for both the crack depth and number of cracks (account for location), which have both shown to be an important factor in LME severity. The crack index holistically quantifies LME cracking of a welded cross-section so an accurate comparison can be made between welding conditions. The crack index is defined as:

$$CI = \frac{nL}{\tau} \qquad (4-1)$$

Where n is the mean number of cracks per sample, L is the lognormal median crack depth and τ is the sheet thickness.

Welding Current Ramping

To investigate the stresses associated with electrode release, a ramp down welding current scheme was developed to withdraw heat from the weld throughout the cycle. This approach would provide a similar effect to the previously mentioned studies investigating hold time without extending the overall welding time. In the standard condition, a two equal pulse welding scheme was used as recommended by American Welding Society D8.9 specification for this material grade [91]. A ramping current condition was designed to give a weld nugget of the same size. To do this, the input current was designed to best match the heat input of the standard condition. In order to keep the process heat input the same, the area under both conditions' current-time graph was kept approximately constant. This is shown mathematically in Eq. 4-2, which was used to determine the ramp peak current and the slope of the ramp line.

$$\int_0^{t_f} I_S(t)\,dt \approx \int_0^{t_f} I_R(t)dt \qquad (4-2)$$

Where I_S is the current of the standard scheme, $I_R(t)$ is the current of the ramping scheme, and t_f is the total weld time. If we assume that $I_R(t_f) = 0$, Eq. 4-2 can be simplified to:

$$\int_0^t I_S(t)\,dt \approx \frac{1}{2} I_{Ri} t_f \qquad (4-3)$$

Where I_{Ri} is the peak current or the current at $t = 0$. For the standard case, a current well above the expulsion current (I_{max}) for this material grade was selected. Using I_{max} + 20% (12 kA) since the Type A cracks targeted by this study only appear above expulsion. Using $I_S = 12\ kA$ and from Fig. 4-1 and Eq. 4-3, the ramp down current was determined and is defined in Eq. 4-4. With the current profile of the ramp case determined, samples were welded under both conditions. The entire welding schedule is summarized in Table 4-1.

$$I_R = -50.4(\mathrm{t}) + 22 \qquad (4-4)$$

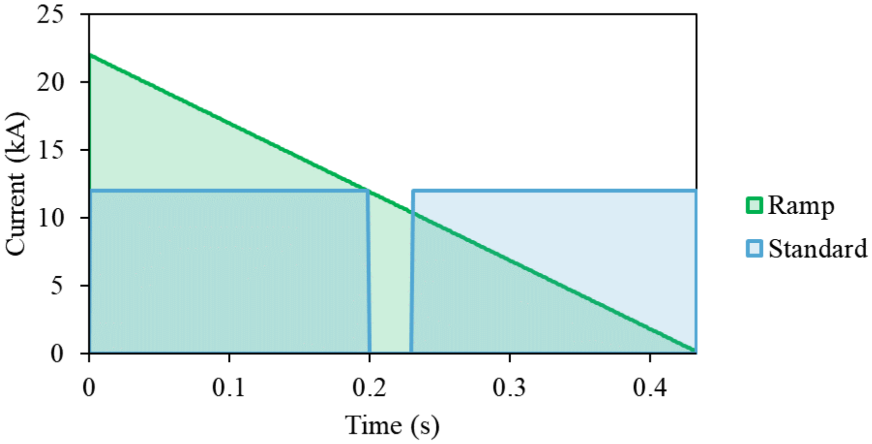

Figure 4-1 *Current schemes for the standard and ramp conditions*

Table 4-1 *Welding schedules for the standard the ramp current conditions*

Welding Schedule	**Welding Current (kA)**	**Electrode dia. (mm)**	**Welding time (ms)**	**Hold time (ms)**	**Force (kN)**
Standard	12	7.0	200 – 33 –200	167	3.5
Ramp	0 – 22 (See Eq. 4-4)	7.0	433	167	3.5

Electrode Geometry

Three distinct electrode types were selected for the study: B-nose, truncated cone, and radius tip electrodes. A schematic drawing of each electrode is shown in Fig. 4-2. To ease the process of keeping heat input constant, the same electrode face diameter of 7 mm was selected for both the B-nose and truncated cone type. Keeping heat input constant allows for an isolated comparison of how each electrode type affects LME cracking.

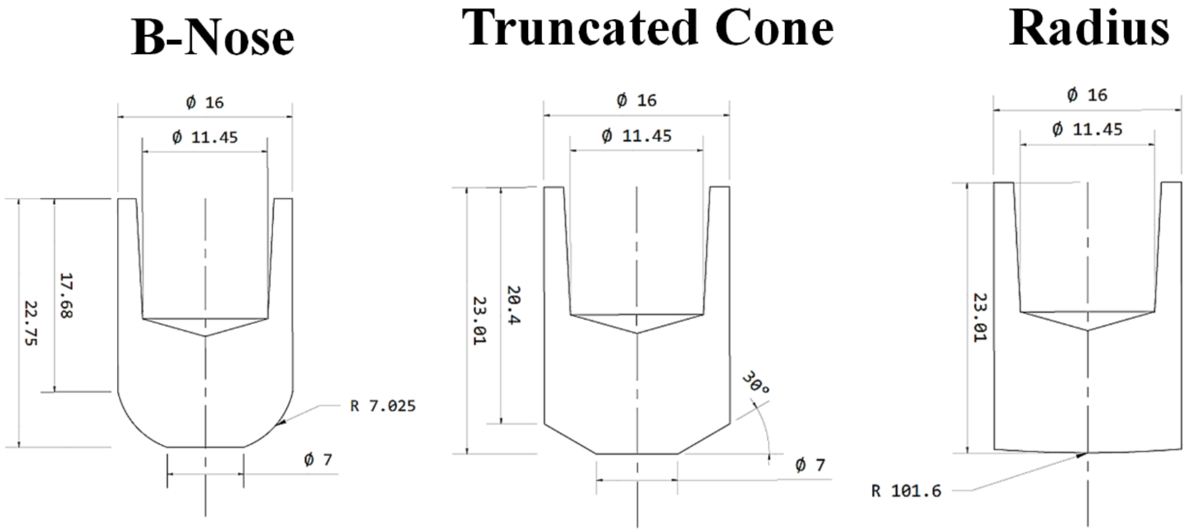

Figure 4-2 *Schematic of each electrode investigated (all dimension in mm)*

Due to the need for changing electrode caps and equipment availability, spot welding for this study was carried out using a 60 Hz single phase alternating current pedestal welding machine. A welding schedule developed based on the A/SP AC starting weld schedule [103] at a heat input just below the expulsion current (11.5kA) for the B-nose electrode, as shown in Table 4-2. This heat input was selected to promote LME cracking for clear observation while not exceeding the expulsion current (I_{max}). The current was adjusted for the cone and radius electrode case (if needed) so the nugget size (and therefore heat input) was the same for all cases. A weld nugget size of 7.4 mm with a 95% confidence interval of 0.1 mm was produced for all samples.

Table 4-2 *Weld schedules used for the electrode geometry study*

Welding Current (kA)	**Electrode dia. (mm)**	**Welding time (ms)**	**Hold time (ms)**	**Force (kN)**
11.5	7.0	117 – 16 – 117 – 16 – 117	167	4.2

To study the cracking phenomena during spot welding, the RSW process was simulated using an axisymmetric finite element method (FEM) model. The critical conditions for the characterization of LME at the electrode-sheet interface was defined as the simultaneous presence of surface temperatures exceeding 419°C (melting temperature of Zn) and tensile stresses; this is a similar methodology used in previous work [69,72,99]. The temperature and stress distributions experienced during RSW were simulated using the commercial finite element software package Sysweld®, designed to simulate the RSW process. A mesh was generated using the software's RSW tool which included 2306 2D quad-tria linear elements for the B-Nose case, 2280 elements for the truncated cone, and 2572 elements for the radius electrode. Temperature dependent material properties for recently developed AHSS (such as TRIP 1100) are not widely available and determining them experimentally can be cumbersome and time-consuming. For this study, the thermo-electrical-mechanical material properties were generated using the material properties simulation software JMatPro® and implemented into the welding software with direct help from ESI Sysweld®. The simulation predicted a nugget size of 7.45 mm which is within the range of the experimental results. To further validate the simulation, the cross-sections of the experimental and simulated temperature results are compared in Fig. 4-3, showing a similar shape in nugget and heat affected zone.

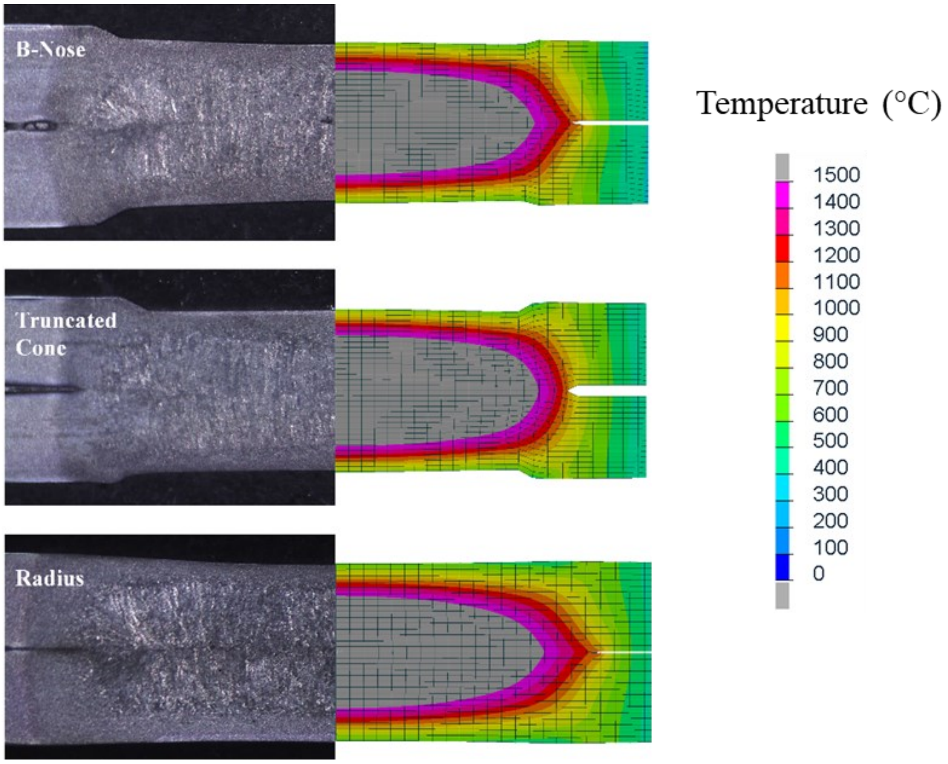

Figure 4-3 *Validation of cross-sections between experimental results and temperature simulation results for each electrode type*

Angular Misalignment

To assess the impact of angular misalignment, the standard weld schedule was used (Table 4-2) and the robot arm was programmed to weld at four electrode angle cases that are relevant to industrial environments including: 0°, 2°, 4°, and 6°. Fig 4-4 shows an illustration of the off-axis angled welding. Welding was carried out on 100 × 25 mm coupons of TRIP 1100 clamped on both ends, using the same weld schedule for all four cases. A heat input just below the expulsion current (9.5 kA) was used. This heat input was selected to promote LME cracking for clear observation while not exceeding the maximum expulsion current. All cases produced a weld nugget size of 6.5 mm with a 95% confidence interval of 0.2 mm.

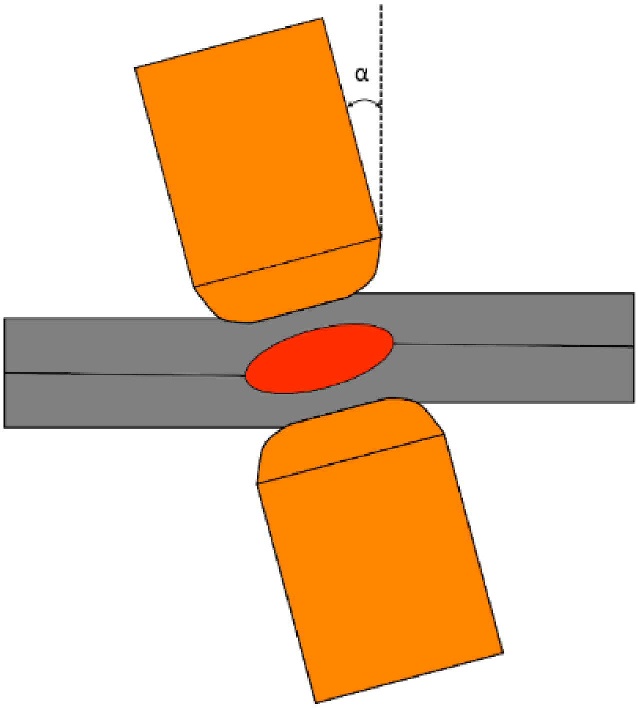

Figure 4-4 *Schematic of angular electrode misalignment with α denoting the angle of misalignment*

Samples for microstructural observation were prepared in the same fashion as for LME observation with addition of etching with 2% Nital (2% HNO_3 + 98% ethanol). Microstructures were characterized using a field emission scanning electron microscope (FESEM, UltraZeiss).

4.4 Results and Discussion

Weld Current Ramping & Centre LME Cracks

The results of the ramp down and standard welding schedules yielded similar weld geometries since the heat input was the same in both cases. Statistical analysis showed no significant difference in nugget size between the two sample types and had a mean nugget size of 7.7 mm with a 95% confidence interval of ± 0.4 mm. Despite the similar final nugget geometry, the two conditions underwent different heating cycles due to the difference in the input current waveform. The current and resistance monitoring from the welding controller is shown in Fig. 4-5.

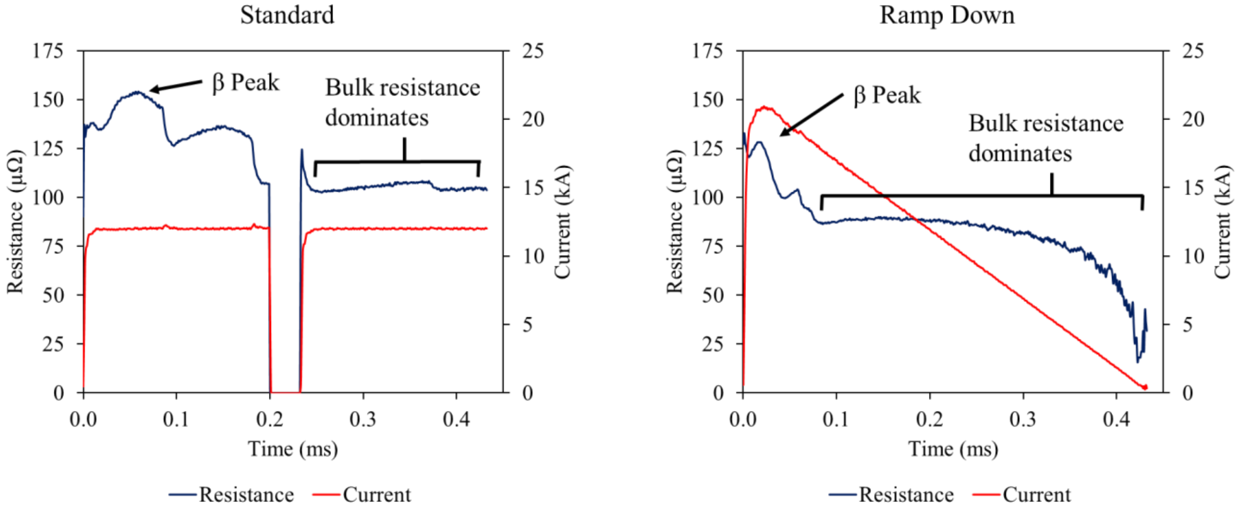

Figure 4-5 *Current and resistance monitoring for standard constant current welding schedule and ramp down current schedule*

From Fig. 4-5, the contact resistance decreases, and material bulk resistance dominates much sooner in the ramp schedule relative to the standard schedule. The first resistance peak after the inflection point is labelled as the β peak, which indicates the start of nugget growth [104]. The ramp down current experiences the β peak much sooner, implying that melting at the sheet-sheet interface happened earlier. Furthermore, the β peak value is lower when welding with the ramp down schedule compared to the standard constant current schedule. This is likely due to the use of a higher current at the time the respective β peak occurs. Additionally, using the current and resistance plots in Fig. 4-5, the power curves during the welding cycle can be calculated. A comparison of the front-loaded, ramp down schedule and the standard weld schedule's power generation is shown in Fig. 4-6.

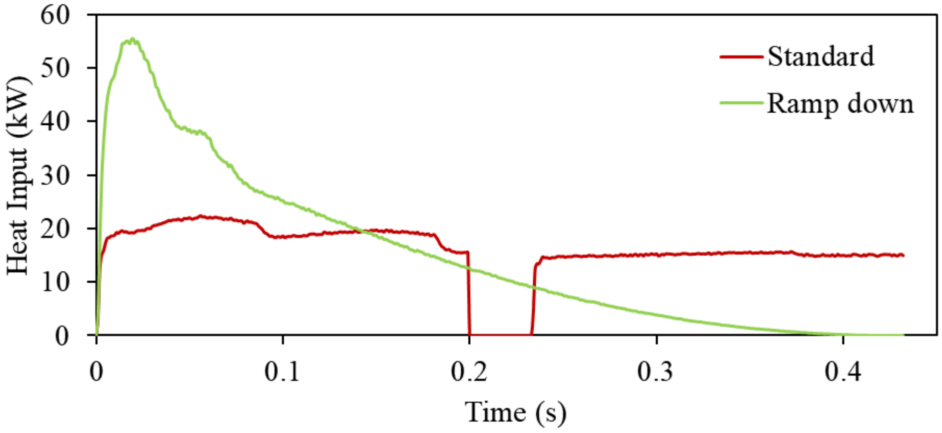

Figure 4-6 *Power curves for standard weld schedule and ramp down weld schedule*

From Fig. 4-6, it can clearly be seen that the ramp down schedule generates the most power in the initial quarter of the weld time. As the weld time continues, the power generation lowers significantly, particularly in the latter half. At this point, it is expected the heat being withdrawn from the weld area by the water-cooled electrodes is greater than the heat being generated. After 0.3 s, there are no signs of nugget growth from the dynamic resistance curve and the power generated is less than 10% of the power output during nugget formation. Similar to the mechanism of extended hold time [99,100], withdrawing heat from the weld mitigates the rapid increase in heat at the weld surface when the electrode (strong heat sink) is removed, as the weld has already cooled through the welding cycle. From the results of the RSW process monitoring, there is expected to be a decrease in LME crack severity in the ramp down current case, particularly for electrode indent area cracks. Unlike the ramp down case, the standard case produces power much more consistently. Throughout the welding cycle the power generated does not go below 70% of the power generated during nugget formation, indicating that a significant amount of heat is being generated. Due to the unmitigated build-up of heat, the electrode removal would result in the previously established stresses and therefore more severe LME cracking.

The results of the standard current showed severe degree of LME cracking. LME cracks were observed across the weld surface in both the electrode indent area and in the weld shoulder. An image showing a typical cross-section of the standard current type sample is shown in Fig. 4-7. It can clearly be seen from Fig. 4-7 that the standard current resulted in severe LME cracking. Large LME cracks were observed in several locations. To fully quantify LME severity the cracks were counted, measured, and are presented as the crack index measuring 1.74 ± 0.07. The high values for crack depth and number of cracks results in a high cracking index which indicates poor weld quality and detrimental LME [102].

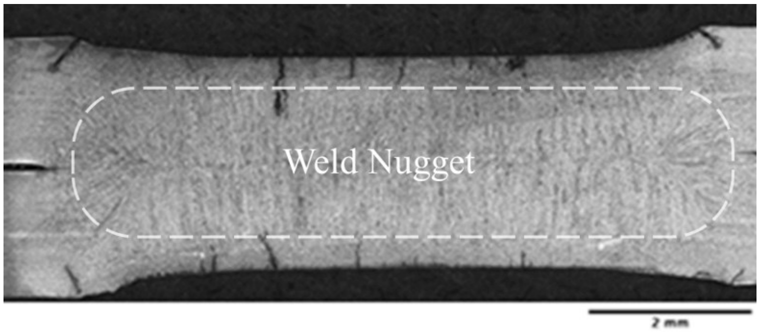

Figure 4-7 *Typical weld cross-section of the standard welding current case*

A comparison of typical cross-sections for each sample type and the local cracking index on cross-section regions is shown in Fig 4-8. The figure shows a stark difference in LME cracking between the ramp down and standard cases. The ramp down current contains fewer LME cracks, particularly in the centre of the weld. The observed ramp down heat generation gives insight into the reduced formation of centre cracks. The weld starts cooling much sooner in the ramp down case and therefore spends less time at elevated temperatures mitigating the thermal shock at the weld centre during electrode release. This results in fewer cracks forming in this location, and also less crack propagation as in the constant current case. It is also interesting to note that in the standard constant current case, the large cracks propagate into the weld nugget, meaning they grew after the nugget was solidified. This further confirms the occurrence of centre cracks to take place after the nugget has solidified during electrode release. Additionally, shoulder LME cracks were observed in both cases (although somewhat less severe in the ramp down case as shown in Fig. 4-8). This observation indicates the formation of shoulder cracks does not depend on the thermal shock and depends on a distinct thermomechanical mechanism.

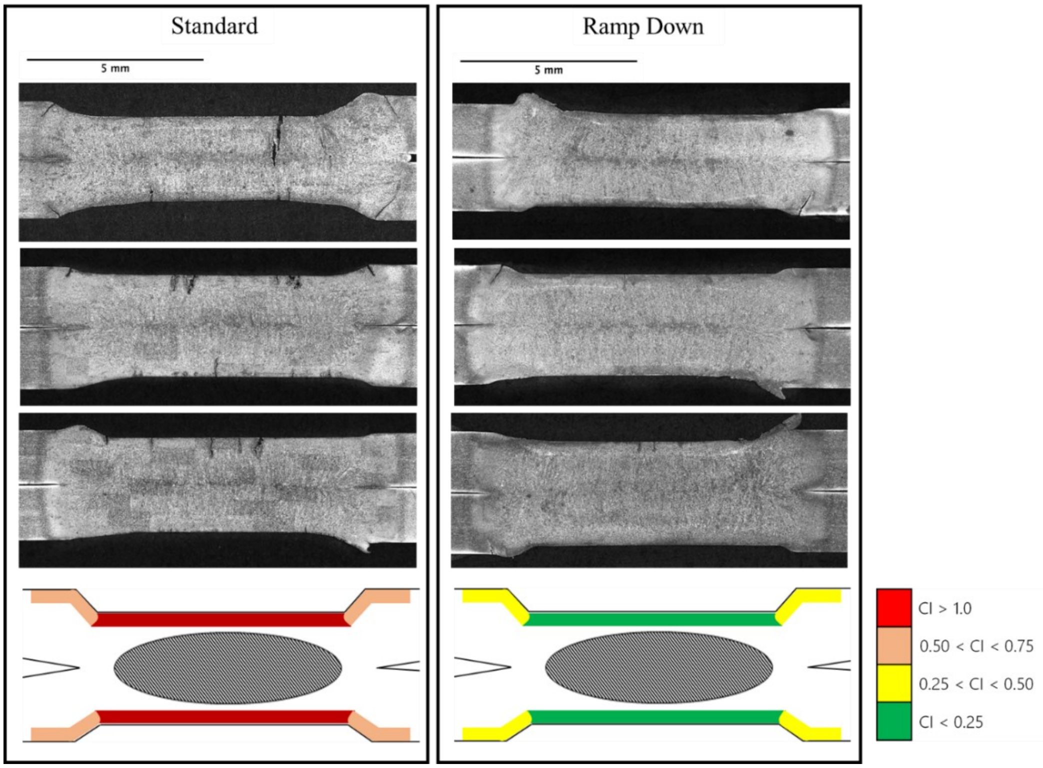

Figure 4-8 *Comparison of LME cracks in welded cross sections of standard weld type and ramping current and a contour map showing the cracking index at different locations*

In order to fully characterize the LME crack populations a full analysis of LME crack metrics was carried out. The results for ramp-down current crack index with a 95% confidence interval are compared against the standard current in Fig. 4-9.

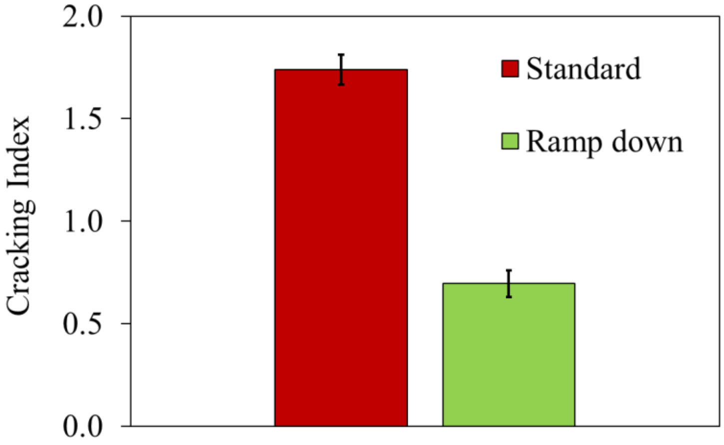

Figure 4-9 *Crack index for ramp down current compared to standard constant current (6 samples per case) at I_{max} + 20%*

From the LME crack index shown in Fig. 4-9 there is clearly a reduction in overall crack severity at high heat inputs. Additionally, the maximum crack depth in the standard case (1319 µm) was significantly larger compared to the maximum crack depth when current ramping was used (597 µm). However, most of the positive effects occurred for Type A centre cracks only (as was seen in Fig. 4-8). The ramp down technique was not as effective at mitigating the formation of Type B shoulder cracks, indicating that their occurrence does not depend on the thermal shock during electrode release.

The ramp down methodology reduced the formation of centre cracks considerably and provided insight into their formation. Like the results of previous hold time techniques, the ramp down current front loaded the heating and power generation which allowed heat to be withdrawn from the weld and mitigating the thermal shock at electrode release. Furthermore, this methodology was applied to a lower heat input case and showed a similar trend. The crack index was reduced with a more noticeable reduction in centre crack severity. Although this study has provided excellent insight into the formation and possible mitigation approaches to LME centre cracks, the formation of shoulder cracks remains unclear. Given the detrimental location for LME cracks is in the weld shoulder or periphery, their formation and reduction require attention.

Electrode Geometry & Shoulder LME Cracks

RSW with distinct electrode geometries showed significant differences in LME cracking for each location. The results showed a clear impact of electrode geometry on the overall LME severity, where welds made using the radius electrode showed the least LME cracking. The results are summarized in Fig. 4-10. The lower LME severity of the welds made using the radius electrode is consistent with previous work [79], but it is important to note the distinction between the cracking observed in welds made with B-nose and truncated cone electrode. The geometry of the electrode shoulder is the only distinction between the B-nose and cone electrode; the electrode face is identical between the two. Similar results would therefore be expected for cracking in the centre region, however, cracking observed in the shoulder region of the respective welds was observed to be quite different. To further investigate the differences in LME crack distribution, the crack index was calculated for the centre and shoulder region for each electrode type. The results showed clear differences in the locations of severity, which are related with electrode shoulder geometry. Experimental cross-sections of the weld samples and the localized LME crack index results are plotted in Fig. 4-11.

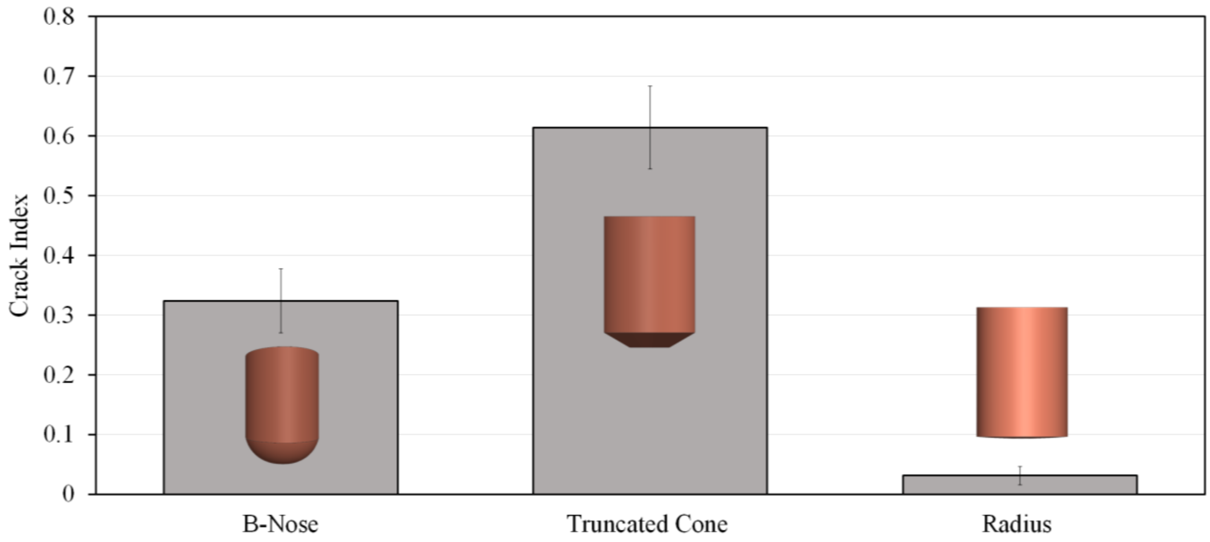

Figure 4-10 *LME severity for each electrode case (6 samples per case)*

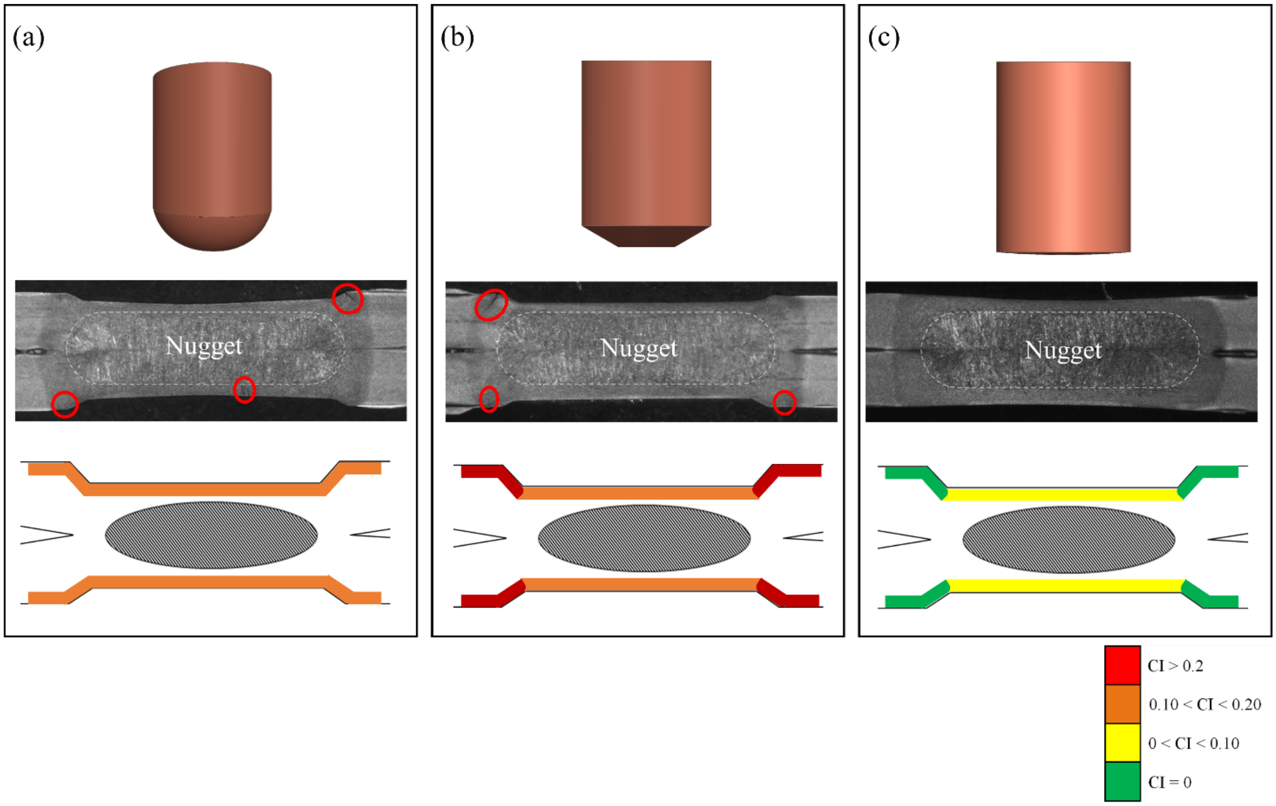

Figure 4-11 *Weld cross-section and localized LME crack index for (a) B-nose electrode type (b) truncated cone (c) radius tip electrode*

The weld cross-section images and crack index plots in Fig. 4-11 show that changing electrode types caused different LME cracking patterns. Clearly, no shoulder cracking occurred when welds were made using the radius electrode, and minimal cracking was observed in the centre region. The radius electrode provides the best option for LME reduction. As expected, similar cracking severity levels were seen in the centre region of both the B-nose and truncated cone. However, when comparing the cracking severity from the weld shoulder, there is a clear increase in severity from welds made using the cone type electrode as compared to the B-nose. Since the only difference between the two cases is the weld shoulder geometry, it can be stated that a truncated cone shaped shoulder leads to worse LME cracking compared to the B-nose. When comparing shoulder cracking in the experimental cross-sections in Fig. 4-11 (a) and (b), it was observed that shoulder cracking in the welds made using cone shaped electrodes (b) is further outside the indent compared to cracks in welds made using the B-nose electrodes (a). Additionally, cracks are commonly observed on the outer portion of the electrode indent in previous work using cone shaped electrodes [80,90] but it has not been reported for B-nose electrodes. Further RSW process analysis is needed to gain insight into this observation. It is well established in literature that temperature and stress are the governing process factors for the onset of LME during welding [44,72]. Therefore, a more detailed thermomechanical analysis of the welding process is needed to understand how changing electrode geometries impacts LME crack development.

To further investigate the thermomechanical differences at the steel surface during the welding cycle made with different electrode types, the welding process was simulated using the Sysweld® software. A temperature and stress plot result taken from the weld shoulder region (see Node 566 and Node 567 respectively as an example in Fig. 4-13(a)) is shown in Fig. 4-12. This plot shows that the various electrodes result in different temperature and stress responses in the steel during the welding process. The stress results presented are in the parallel direction of the sheet length since that is the stress component responsible for LME cracking.

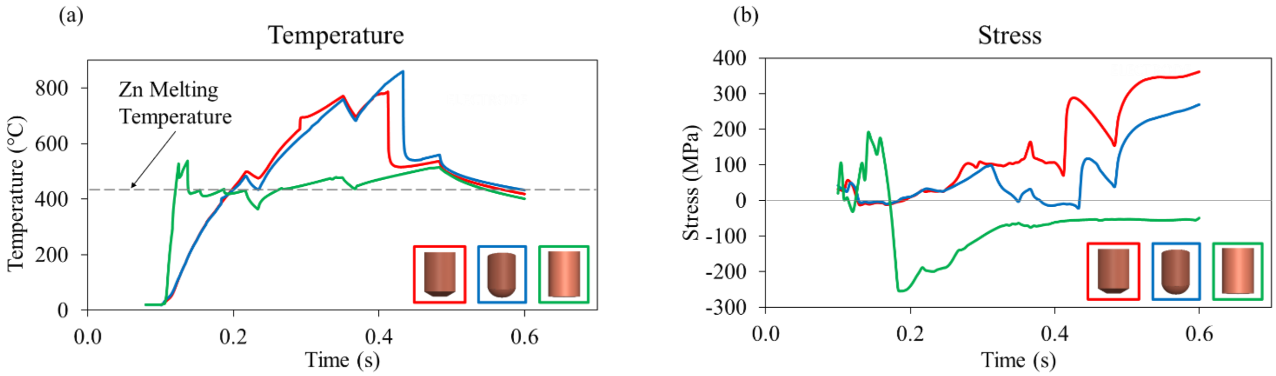

Figure 4-12 *Plots for (a) temperature in the weld shoulder area (b) stress perpendicular to the thickness direction*

When comparing the electrodes, it may be seen that the temperature and stress plots at the shoulder of welds made with the radius electrode are fundamentally different than those from welds made with the B-nose and truncated cone electrodes. The shoulder of the welds made with radius electrodes experienced temperatures that stayed close to or below the melting of Zn (419 °C) and stresses were compressive, except for a brief period during initial stage of welding. These characteristics are due to the unique contact of the radius shaped electrode. In contrast, welds made using both the B-nose and truncated cone electrode show consistent heating (apart from the cooling between the pulses) until a sudden drop in temperature is observed towards the end of the weld time. This sudden drop in temperature is accompanied by a sudden increase in tensile stress. The large temperature drop is due to the material softening in the sheet steel, leading to plastic deformation in the sheet from the electrode pressure, which creates a new thermal contact at the shoulder. This event is called the 'mechanical collapse' and is shown graphically for the cone electrode in Fig. 4-13. After this point, all three temperature curves converge as shown in Fig. 4-12, since they all have direct contact with the electrode, which is extracting heat from the weld.

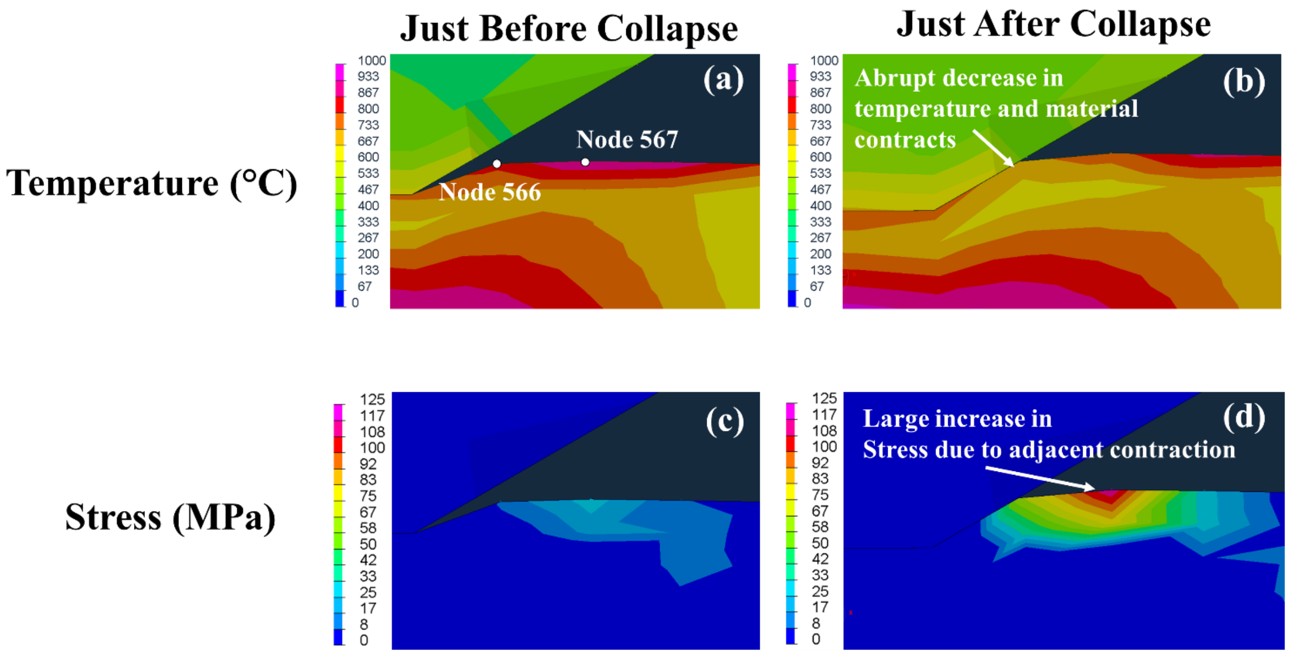

Figure 4-13 *Temperature and stress (a) Temperature plot at the location of shoulder cracks just before collapse (b) temperature field at the instant just after collapse (c) stress field just before collapse (d) stress field just after the collapse showing increase in stress*

Mechanical collapse not only affected shoulder temperature, but it also increased the tensile stresses. Fig. 4-13 shows that increased cooling resulted in a peak stress in the steel away from the electrode/sheet contact, where fastest cooling rate occurred. This phenomenon of sudden cooling with the resulting stress can best be explained in its basic form with a schematic of the material movement during the welding process. In Fig. 4-14 shows a string of elements represented the material at the top surface of the sheet during welding before collapse. At this time the whole region is hot and is at temperature equilibrium. Once mechanical collapse occurs, the element on the left suddenly cools and contracts. The contraction of the left element results in the neighboring hot elements being stretched into tension to accommodate the volume change of the cooler elements. This causes the greatest increase in tensile stress in the element which did not experience any contraction as it needs to have the greatest compensation for the cold elements' contraction.

Far from the peak stressed element, the elements no longer carry the tensile load and there is no increase in tensile stress due to the contraction of the cold element. From this analysis, it may be seen that the stresses are primarily thermally driven as opposed to mechanically driven, as they are caused by the new thermal contact between the electrode and sheet, leading to a sudden cooling in the weld shoulder.

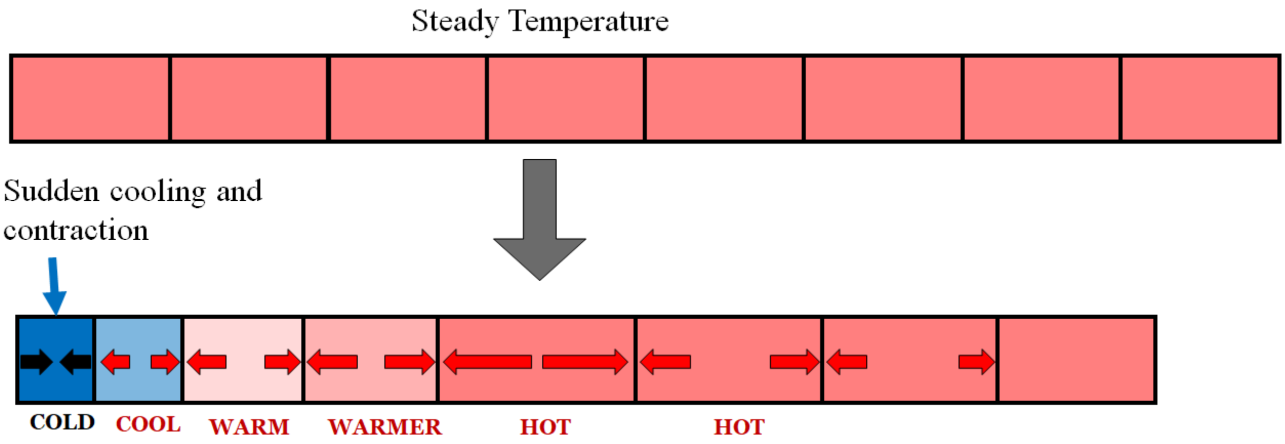

Figure 4-14 *Basic illustration of thermal contraction and tensile stresses in neighboring elements*

The temperature and stress field results show the key role of electrode geometry in LME severity and provides insight on the experimental results. The shape of the electrode shoulder controls the formation of LME cracks as it governs contact conditions between the electrode and sheet at the shoulder. Previous work on electrode force by Choi et al. [69] has also shown the thermal aspects of the RSW process to be significant as more severe LME was observed when welding using low electrode force. Although the mechanical force of the electrode was decreased, the temperature and thermal stress in the steel were much higher. It is therefore not surprising that a thermally dominant mechanism drives LME when the influence of electrode geometry is studied. The radius type electrode proved to be the best for reducing LME cracking because of its consistent contact throughout the welding process. The electrode contacts the sheet early in the process and cools the sheet continuously throughout the welding cycle. However, the differences between the weld shoulder contact of the B-nose and cone type electrode should be investigated in more detail.

When comparing the stress field plots of the truncated cone and B-nose electrodes, a subtle yet significant difference is observed. A stress field comparison between the electrode types showed a shift in the location of highest stress, as shown in Fig. 4-15. In the case of the truncated cone electrode, the location of highest stress is further out from the weld shoulder compared to the B-nose case. A similar pattern was observed for the location of LME cracks in the experimental work (shown in Fig. 4-10), however there was no clear experimental explanation for the change in location. The shift in the location of highest stress shown from the process simulation explains the differences in shoulder crack location.

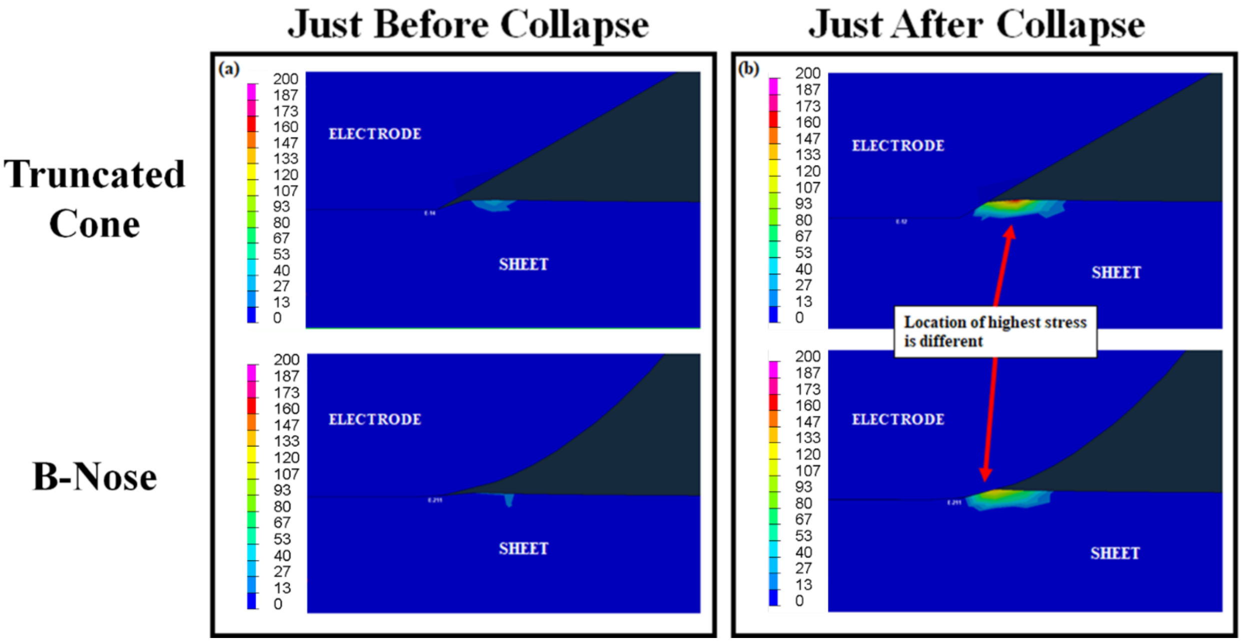

Figure 4-15 Comparison of stress fields (MPa) for cone and B-nose electrode (a) before collapse (b) instant after collapse showing different peak stress locations

Both the truncated cone and B-nose electrode experience the same thermo-mechanical phenomenon leading to tensile stresses in the shoulder region. However, the shift in stress location leads to a shift in LME cracking location as shown in Fig. 4-15. The location of peak stress from the process simulation directly matches the experimental LME cracking location, but it is unclear why the shift in stress location occurred. To gain further insight, the factors that govern thermal contact during the process simulation need to be examined.

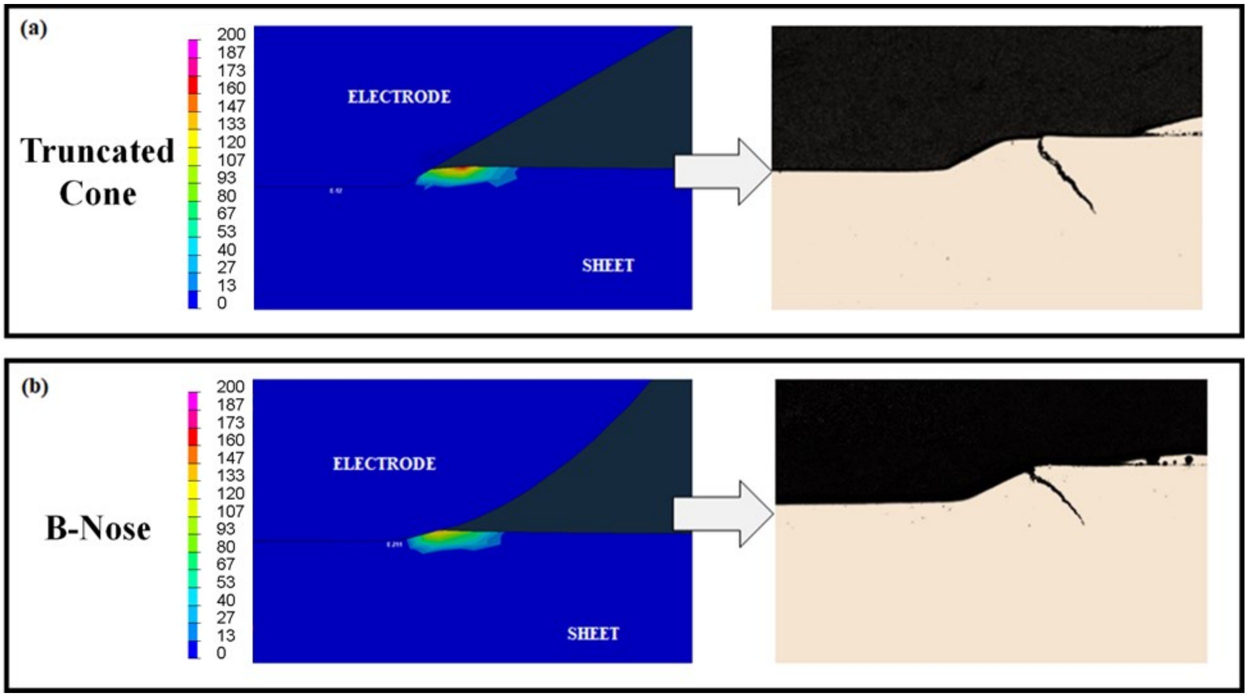

Figure 4-16 *Comparison of the stress field simulation (MPa) and experimental results for LME cracking (a) cone type electrode (b) B-nose electrode*

In order for a shift in location of stress to occur the location of heat transfer to the electrode must be different. As all other process variables are the same, the effects of electrode geometry on thermal contact are examined. The efficiency of thermal contact conductance is highly dependent on the contact pressure between two bodies [105]. To further investigate the thermal contact conductance, the plots of pressure and heat flux were examined which are shown in Fig. 4-17. For the truncated cone, there is a pressure concentration at the corner of the electrode face and electrode shoulder. Additionally, high pressure from the electrode continues up the weld shoulder of the sheet. The high pressure leads to efficient cooling along the entire length of the weld shoulder area, resulting in the entire weld shoulder contracting due to negative thermal expansion. As the weld shoulder is the area contracting, the tensile stresses occur away from the weld shoulder as described previously. Conversely, the B-nose electrode has low pressure along the length of the weld shoulder which leads to the cooling and contracting under the electrode face and at the lower edge of the weld shoulder. This leads to tensile stresses at the top of the weld shoulder. Due to the difference in pressure profile from each electrode, the location of material cooling and contraction shifts, resulting in a shift of high stresses.

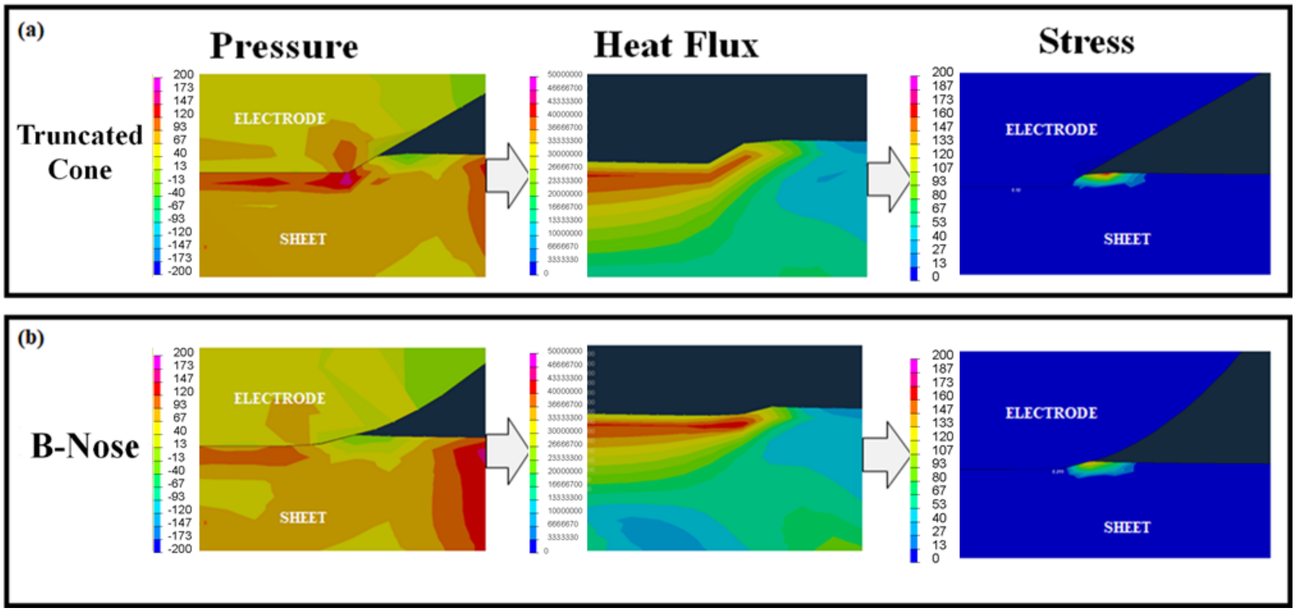

Figure 4-17 *Pressure (MPa), heat flux (W/m^2) and stress fields (MPa) the instant after collapse for the (a) cone electrode (b) B-nose electrode*

The investigation into electrode geometry not only showed new insights in LME shoulder cracking but also into the mechanism that governs crack location in the shoulder. Discrepancies between different locations of shoulder cracks can now be explained with regards to the RSW process. Furthermore, the insights gained on the heat transfer and mechanics of the electrode-sheet interface can be used for further work on LME reduction. Since the mechanism of crack formation is better understood, researchers can work to apply these insights into reduction methods.

Angular Misalignment & Low Temperature LME

Angular electrode misalignment is a common external factor to the RSW process in an industrial setting. LME cracking showed a clear sensitivity to an electrode angle of 4° and 6°. The results are summarized in Fig. 4-19 with a 95% confidence interval. LME severity appears to worsen as electrode angle increases, as an increasing trend is shown. However, it is important to note that no increase in LME was observed in the 2° case compared to the 0° case. The results of a Student's T-Test showed there to be no statistical difference between the cracking severities resulting from both conditions. The weld nugget diameter was measured for each case, which showed a consistent nugget size of 6.5 with a 95% confidence interval of 0.2 mm. This is expected given the heat input for each case remained constant. It is interesting to note that in previous work nugget size was stated to be directly related to LME development during RSW [106] but here there is a separation of nugget size and LME severity as shown in Fig 4-17. Having electrode misalignment introduces bending into the work piece, which results in external mechanical stress. Stress has been described by both Kang et al. [41] and Beal et al. [36] as a critical condition for the onset of LME. The increase in LME severity is due to the increased mechanical distortion from welding with an electrode angle and was observed to be localized to the shoulder region. A progression of increasing LME crack size with each angle case is shown in Fig. 4-19.

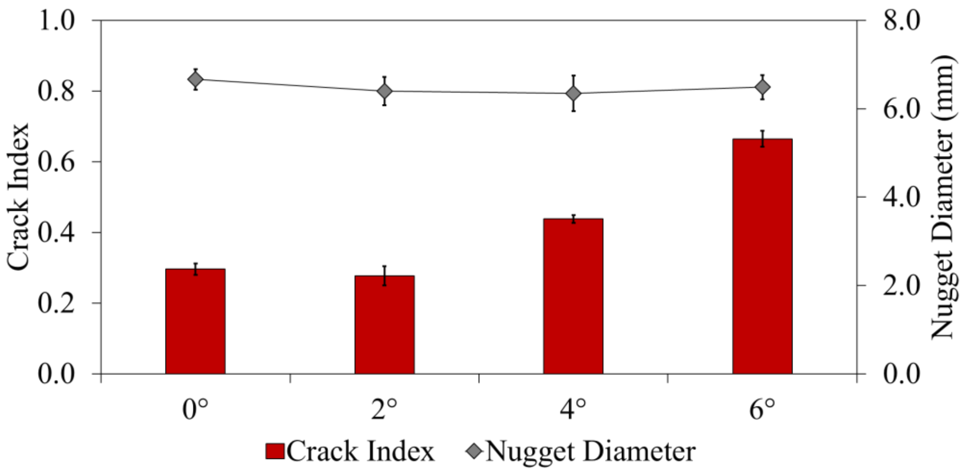

Figure 4-18 *Plots of LME crack severity and nugget size for each electrode angle case (6 samples per case)*

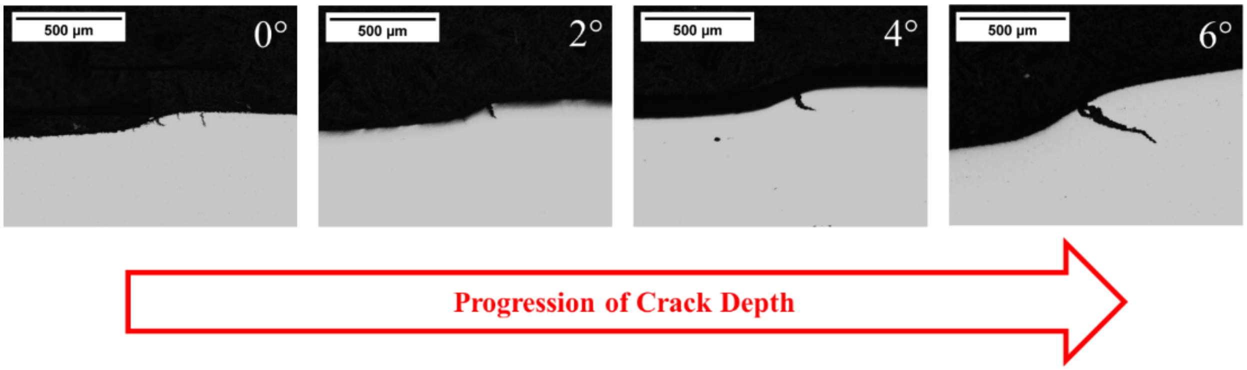

Figure 4-19 *Typical weld shoulder LME cracks for each case showing a progression of crack size*

Similar to the crack index plot, an increasing trend in crack size is observed but there is no discernable difference between the 0° and 2° case (see Fig. 4-19). These results show that the change in stress and thermal fields of the 2° case was not sufficient to promote a detectable difference in LME. Therefore, it can be said that LME cracking during RSW is not sensitive to low angular electrode misalignment. However, a steep increase in LME is observed once the threshold has been crossed, leading to critical LME, despite being below the expulsion condition.

Examples of the welded cross-sections are shown in Fig. 4-20, which shows the severity of the 6° case.

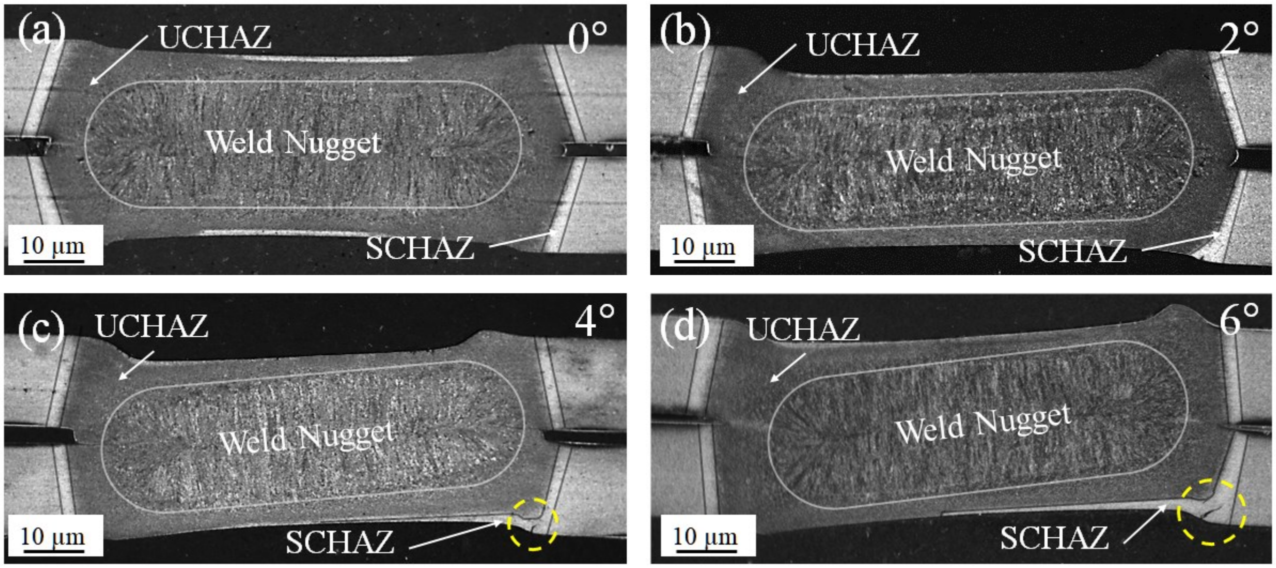

Figure 4-20 *Example cross-sections of the (a) 0° case (b) 2° case (c) 4° case (d) 6° case showing the weld nugget and HAZ shape with large LME cracks highlighted in yellow*

Fig. 4-20 highlights deep LME cracks are in the weld shoulder area, on the side bent in and receiving higher clamping pressure, when large misalignment is introduced. However, a more detailed inspection of the weld in Fig 4-20 (d) shows LME cracks present in the sub-critical heat affected zone (SCHAZ) in addition to the upper-critical heat affected zone (UCHAZ) and inter-critical heat affected zone (ICHAZ). In the present literature, LME cracks during RSW have only been observed in the UCHAZ or ICHAZ above the Ac_1 temperature. However, in this case, cracks can be observed in the UCHAZ and in the outer lighter HAZ regions, indicating that LME cracks may also form in the SCHAZ. Clearly, the weld nugget develops on an angle due to the electrode angle. Additionally, the UCHAZ (shown as the darker shade of grey) is an unusual shape.

It was observed as electrode angle increases the UCHAZ also becomes angled and moves away from the weld shoulder on the indented side. A schematic of the lower right weld shoulder showing the retreating of the UCHAZ boundary, with the stationary LME crack, is shown in Fig. 4-20. Despite the shifting of the high temperature zone away from the weld shoulder, LME cracks still form at that location. The consistency of LME at the weld shoulder shows the stresses experienced during welding are still sufficient for the onset of LME. Additionally, the distortion from the misaligned electrodes leads to a progressively larger crack in this region (as seen in Fig. 4-18) even though peak temperature in this location decreased with increased misalignment. In the extreme case of 6°, a large LME crack has occurred far outside the UCHAZ (Fig. 4-19d). To confirm if LME cracking has occurred outside the UCHAZ or ICHAZ a full characterization of the HAZ is required.

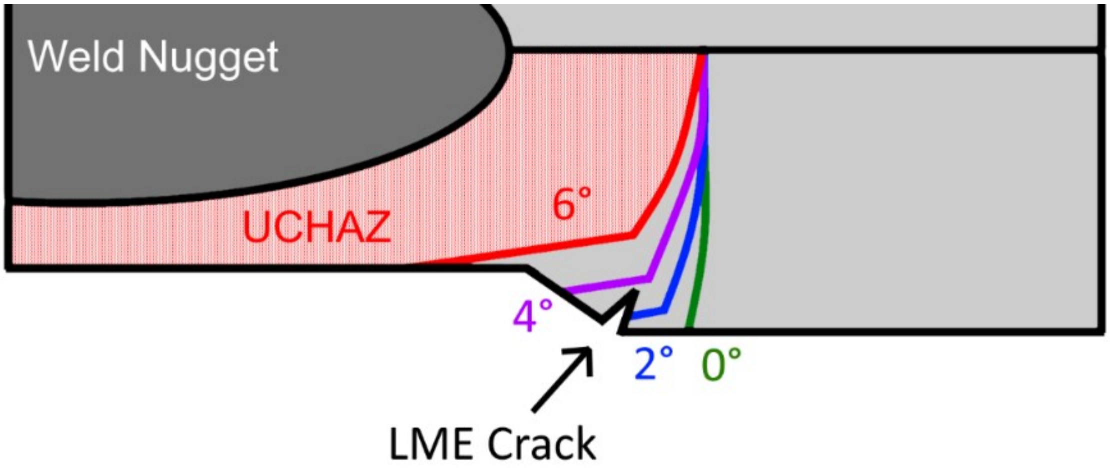

Figure 4-21 *Schematic showing the HAZ moving away from the weld shoulder with increasing angular misalignment while the LME crack location is stationary*

Although etching contrast implied that LME cracking occurred in the SCHAZ, considering the past work by Beal et al. [36] which showed LME sensitivity required material to be heated between 700 °C – 900 °C, a microstructural analysis of the HAZ was completed. Fig. 4-22 shows the optical microscope (OM) micrograph and detailed SEM images of the various microstructures post-welding. The microstructure of the base material (BM) in Fig. 4-22 (a) is comprised of a ferrite matrix with embedded bainite and martensite. Additionally, the microstructure of the SCHAZ (Fig. 4-22 (b)) where the temperature during welding did not exceed Ac_1 is similar to that of BM structure but includes tempered martensite. No significant changes were observed in terms of the volume of bainite but tempered martensite is a clear characteristic of the SCHAZ. The microstructure of the ICHAZ (Fig. 4-21 (c)), where the temperature during welding ranged between Ac_1 and Ac_3, consists of fine martensitic islands in a ferritic matrix. Also, in this region, the bainite phase has virtually disappeared and transformed into martensite due to the intercritical annealing and subsequent quenching. The UCHAZ region, where the peak temperature exceeded the Ac_3 temperature, transformed to coarse martensitic blocks with small fraction of ferrite (Fig. 4-22 (d)). As illustrated, the UCHAZ possessed higher fraction of martensite, but less ferrite compared to the ICHAZ region. Finally, in the fusion zone (FZ), columnar martensite structure with large and thick lath martensite is shown (Fig. 4-22 (e)). With the microstructural features of each region identified, the area near the crack can be characterized. SEM images of the LME crack and surrounding microstructure were taken to identify and match the HAZ region.

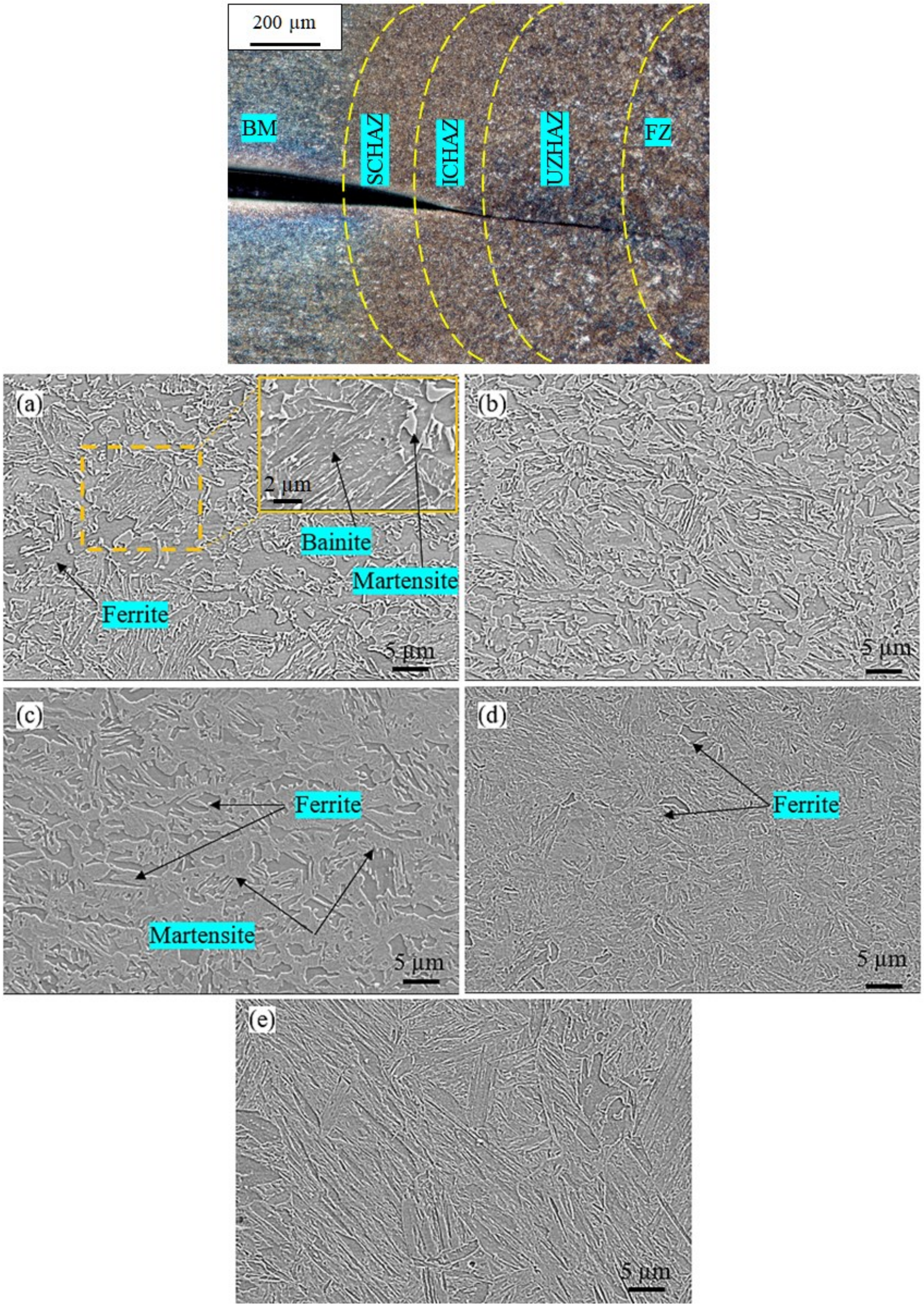

Figure 4-22 *OM micrograph and SEM microstructure of the (a) base metal (BM), (b) sub-critical heat affected zone (SCHAZ), (c) inter-critical heat affected zone (ICHAZ), (d) upper-critical heat affected zone (UCHAZ) and (e) fusion zone (FZ).*

To confirm that cracking did occur in the SCHAZ, images of the microstructure were taken. Fig. 4-23 shows the microstructure surrounding the LME crack, resembling the SCHAZ. The microstructure consists of ferrite matrix accompanied with tempered martensite and bainite. Fig. 4-24 compares the martensite islands in BM and tempered martensite of the SCHAZ (near LME crack). As can be seen in Fig. 4-24 (d), cementite has precipitated into martensite blocks which is an established characteristic of tempered martensite from previous works by Furhara et al. [107]. From the work by Furuhara et al. it is well known that after tempering martensite below Ac_1 temperature, supersaturated carbon previously trapped in the martensite precipitates as cementite on martensitic block, packet, and lathe boundaries. The martensite observed in Fig. 4-24 (d) showed this structure and can therefore be characterized as tempered martensite. The tempered martensite in the crack region is clear evidence that LME cracking occurred in the SCHAZ region. Occurrence of LME in the SCHAZ has not yet been recorded in literature of LME in RSW [61]. This is likely due to the use of conventional welding setups, which may not have provided the necessary thermomechanical conditions for the onset of LME. Additionally, LME in AHSS has been reported by Beal et al. [36] and Jung [108] to occur at temperatures only above a typical Ac_1, which made the idea of SCHAZ crack seem unlikely. However, a detailed look at Fig. 4-23 (b) and (c) conclusively shows the LME crack in the SCHAZ and branching out along the ferrite-prior martensite grain boundaries.

In the literature, LME is widely reported in austenitic structures and rarely observed in ferritic structures. One of the mechanisms for LME crack initiation in the Fe/Zn system is stress-assisted Zn diffusion as described by both Ling et al. [109] and Kang et al. [41]. As reported by Kang et al., the grain boundaries' diffusivity is much higher than the bulk Zn diffusivity in both ferritic and austenitic structures, therefore Zn diffuses along the grain boundaries prior to lattice diffusion.

Additionally, Kang et al., also describes austenitic structures to have a higher Zn grain boundary diffusivity than ferritic structures. Since the LME crack is intergranular, austenitic structures have commonly been reported to be more susceptible than ferritic structures. However, as presented in Figures 4-23 and 4-24, the LME crack propagated along ferrite-prior martensite interfaces. One possible explanation is the increased stress in the material due to the mechanical distortion. Under the grain boundary diffusion-based theories of LME, the stress would enhance the grain boundary diffusion, easing the Zn penetration of the grain boundaries. Under SCHAZ conditions, a typical RSW set-up does not provide the required stress to compensate for the slow low temperature diffusion. Therefore, SCHAZ LME would require sufficient stress for Zn penetration meaning there is a co-dependence on temperature and stress state for the onset of LME.

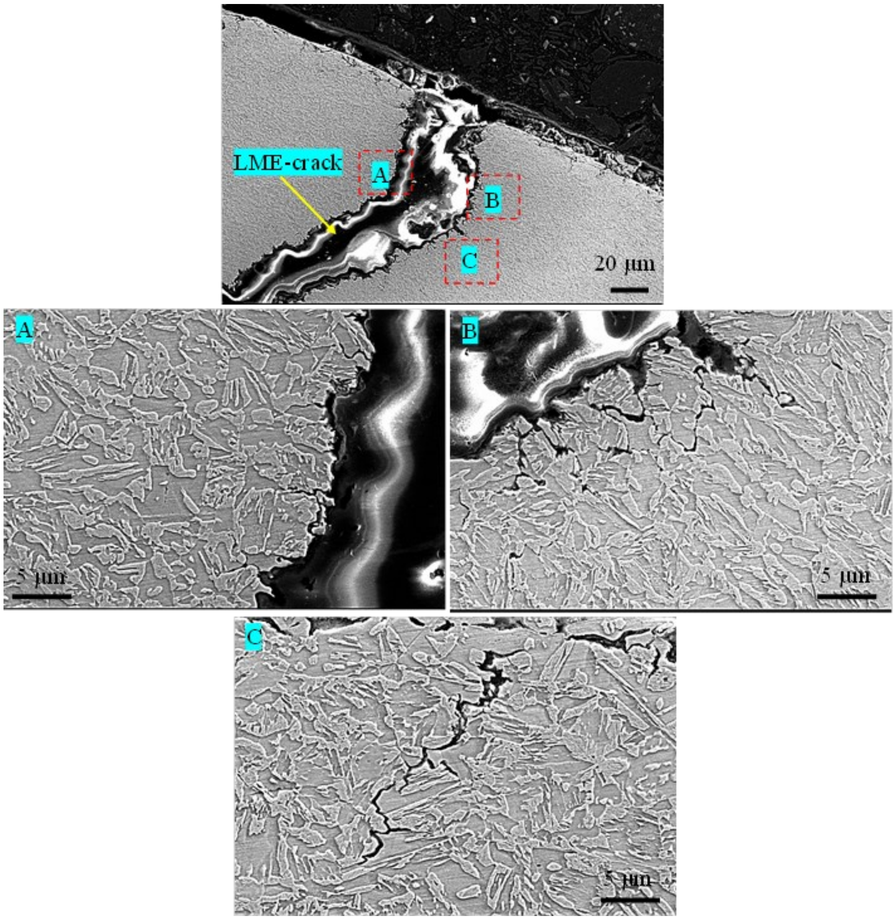

Figure 4-23 *SEM images of the microstructure near a sub-critical LME crack*

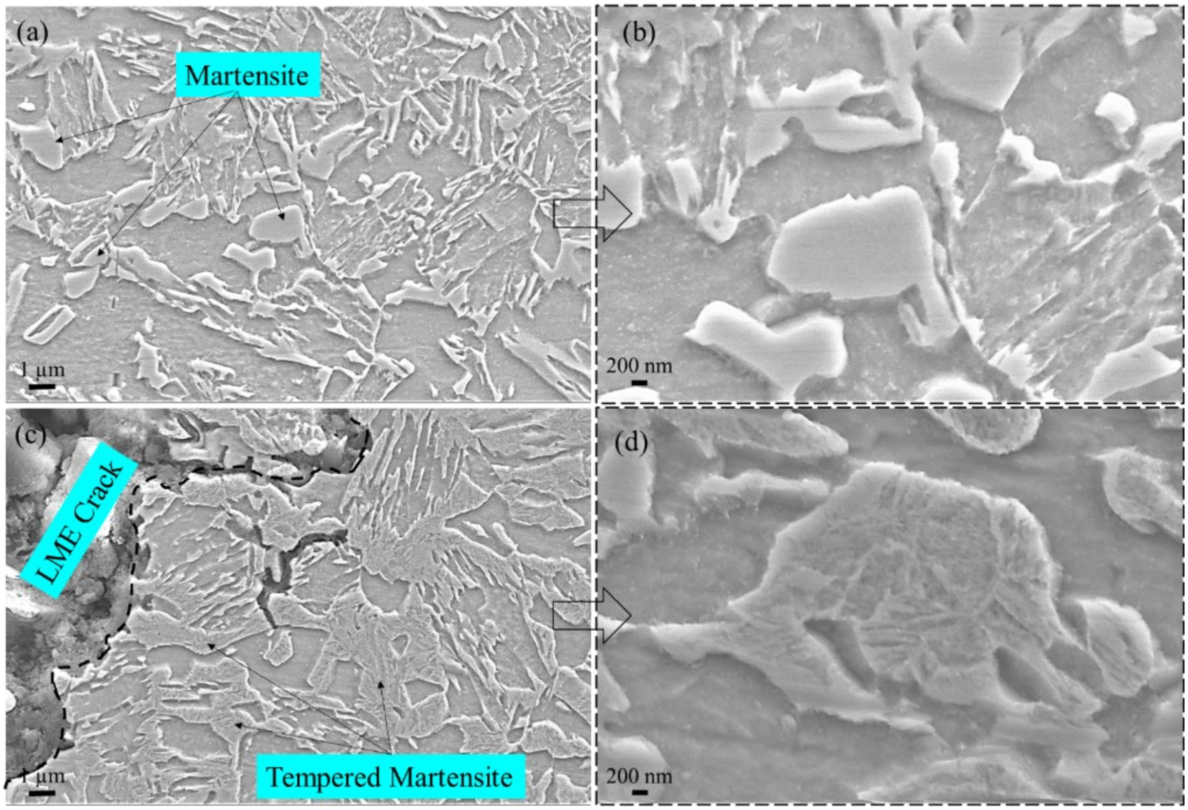

Figure 4-24 *SEM micrographs of the martensite islands in (a,b) base metal (BM) and (c,d) subcritical heat affected zone (SCHAZ) regions*

With the LME cracking established to occur in the SCHAZ, the determination of the Ac_1 temperature will uncover the upper limit for the temperature range that LME occurred. A dilation study of the material was carried out and the results are plotted in Fig. 2-24 (a). The results show that the Ac_1 transformation starts to occur at approximately 660°C, which was characterized using a method developed by Mesplont et al. [110]. Additionally, Fig. 2-25 (b) shows the transformation percentage as temperature increases according to the methodology by Mesplont et al., clearly indicating the temperature required for transformation. This upper limit temperature of the SCHAZ is below the reported temperature range for LME in AHSS as described in by both Beal et al. and Jung et al. The occurrence of LME not only in a ferritic structure but also at unusually low temperatures adds to the novel observations of this study.

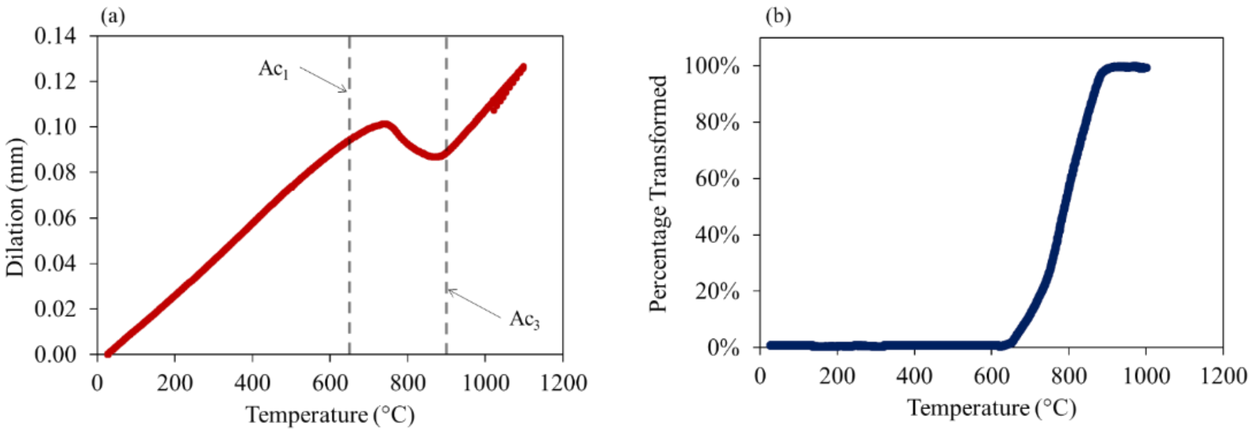

Figure 4-25 *Curves showing (a) TRIP1100 dilation and (b) percentage transformation during heating*

LME cracking in the SCHAZ and below 700°C has not been discussed extensively in the literature. Given the bending induced by the angled electrode, the results of this study show the minimum temperature for the onset of LME is dependent on mechanical factors. This notion has been discussed in earlier studies but results showing evidence of low temperature/SCHAZ LME cracking with mechanical assistance has been sparsely reported. Furthermore, in the case of the TRIP 1100 steel, it is possible for LME to occur outside the traditionally reported range.

LME Crack Formation and Timing

This chapter has revealed key insights into the formation of LME cracks and during which stage of RSW the LME cracks occur. Additionally, the observations from this chapter provide further insights into the observations in previous literature. This study established that Type B LME cracks occur as a result of mechanical collapse during the weld time segment. Therefore, only mitigation approaches that address this mechanism will result in reduced Type B cracking. When looking at the previous work by Choi et al. [69] and Wintjes et al. [73], their adjustments to the weld process caused reduced electrode indentation. Furthermore, the conclusions of Murugan et al. [79] which stated large radius electrodes LME cracks can be viewed with more depth as it is now clear the radius electrode creates consistent contact which lowers temperatures and avoids a sudden mechanical collapse. In the case of Type A cracks, the effects of longer hold times to withdraw heat were confirmed by targeting the same thermomechanical mechanism by different means. The use of a ramp down current to front load heating and allow early heat withdrawal resulted in reduced Type A cracks. A schematic summarizing the results from this study and previous literature is shown in Fig. 4-26.

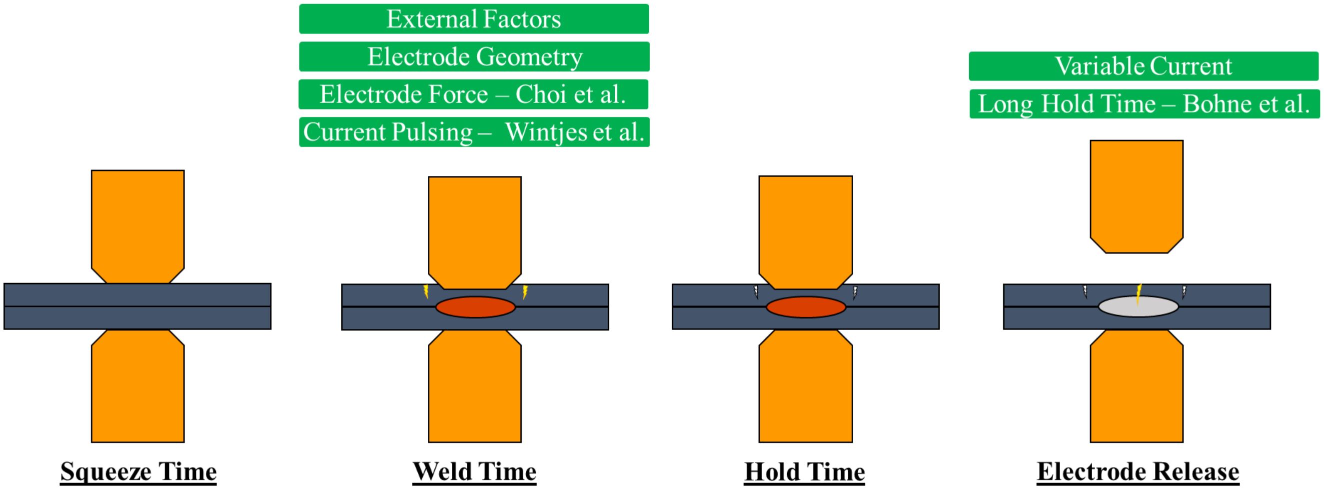

Figure 4-26 *Timing of LME crack formation in the shoulder and centre region with associated reduction techniques*

Another scenario investigated in this chapter was the effects of external factors such as angular misalignment. This was observed to worsen LME shoulder cracks but have no effect on centre cracks which further validates the thermal shock at release as their thermomechanical source. The distortion at the shoulder from the angular misalignment led to LME cracks only in that location. Given the distinct thermomechanical mechanisms responsible for LME, it has become clear that reduction techniques need to be specifically developed for distinct crack types. Techniques that target the thermal shock phenomenon will not address Type B cracks. As shown in Chapter 3, LME crack location is a characteristic that can lead to strength loss, so this new insight provides key knowledge for RSW process solutions to LME cracking. The formation mechanism of critically located cracks (shoulder and periphery) must be targeted specifically by addressing the issues of electrode collapse.

4.5 Summary

This chapter studied the occurrence of LME during RSW and revealed new insights into the crack formation mechanisms, timing, and necessary conditions for cracking. The following conclusions were drawn:

(a) LME centre cracks (Type A) are formed due to the thermal shock at electrode release. By front loading the heat generation with a ramp down weld schedule these cracks were mitigated, and the proposed mechanism was validated.

(b) The mechanical collapse and RSW electrode indentation were observed to be responsible for the formation of shoulder cracks (Type B). As the water-cooled electrode presses into the hot sheet, the sudden material shrinkage leads to tensile stresses. This finding provided insight into previous literature on LME crack reduction and also has set a foundation for further mitigation of Type B cracks are known to be detrimental to crack performance.

(c) Angular misalignment beyond 2° was observed to worsen LME cracks. Specifically, LME cracks worsened in the distorted region. However, due to increased pressure and thermal contact of the RSW electrode, the LME cracks were observed in the SCHAZ meaning they formed at lower than usual temperatures and the austenite phase is not necessary.

(d) Temperature and tensile stress were identified as the two critical factors leading to LME cracking during RSW. However, as demonstrated in the SCHAZ LME, there appears to be a co-dependence of temperature and stress for the onset mechanism of LME.

Chapter 5

LME Critical Stress and Transport Mechanism

5.1 Overview

Temperature and stress play a key role in the formation of LME cracks during RSW. Elevated temperatures and stresses from the electrode mechanical collapse were observed to cause LME cracking in detrimental regions. However, the exact role temperature and stress plays in the LME mechanism still needs to be determined. This chapter took a detailed look at the temperature and stresses required for LME through elevated temperature tensile testing. Furthermore, the co-dependence of LME on temperature and stress were revealed. By using interrupted elevated temperature tensile testing, the role stress plays in the LME onset mechanism was revealed to be diffusion-based. The LME transport mechanism was identified as stress-assisted diffusion using both experimental observations and mathematical modeling. The findings from this chapter explain why LME cracking is so prevalent in the RSW process, as the elevated temperature and stresses of the process enhance the diffusion process leading to LME crack formation.

5.2 Background

From the conclusions of Chapter 4, it is clear that the presence of elevated temperatures and stress during the RSW process are fundamental to the occurrence of LME. However, with the complex nature of the RSW process it can be difficult to isolate the effect of secondary process variables such as temperature and stress since they are not directly controlled by input process parameters.

Elevated temperature tensile testing has become a popular method to observe the LME phenomenon in the Fe/Zn system without the complexity of the RSW process. Beal et al. [42,44,111] conducted extensive thermomechanical uniaxial tension testing on Zn coated high Mn TWIP steel. The experimental investigation revealed an LME dependency on temperature as LME was only observed in the 700 °C – 900 °C range. The upper bound temperature clearly lines up with the Zn vaporization temperature (906 °C), meaning after this point there would be no available liquid Zn for LME. However, the lower bound temperature is perplexing since it is well above the Zn melting temperature (419 °C). Beal et al. suggested that a critical stress was needed for the onset of LME, which at low temperatures exceeded the material tensile strength and could not be reached. In a study by Kang et al. [31], a similar temperature range for LME was observed for the Fe/Zn couple. However, Kang et al. noted the lack of Zn penetration at low temperatures in materials that could not reach high stress levels. The authors pointed towards the possibility that high stresses were needed to trigger LME. Similar to the work by Beal et al., the threshold or critical stress discussed by Kang et al. explains the lack of LME below 700°C. Similar findings were reported by both Jung et al. [15] and Bhattacharya et al. [43] who also carried out thermomechanical testing. This further supports the notion of a critical stress (which appears temperature dependent) for the onset of LME.

The presence of tensile stress is stated to be required for LME. However, due to the lack of understanding on LME formation, the precise role of stress remains unclear. As stated in 2.2.2 and 2.2.3, literature has shown evidence for both liquid penetration and grain boundary diffusion as the Zn transport mechanism leading to LME formation. This contradiction on the LME transport mechanism has made it impossible to provide a detailed description of LME formation and why factors (such as stress) affect the occurrence. Gordan and An [24] postulated that a diffusion penetration zone ahead of the crack tip was required for LME. They observed the formation of LME cracks (and therefore the penetration zone) was dependent on both temperature and stress. In the grain boundary diffusion theory, scholars have pointed towards a stress diffusion flux to assist the diffusion process since the flux from a concentration gradient is usually insufficient to facilitate LME [24,25,32]. This theory proposed an LME transport mechanism but lacked detailed experimental observation of LME formation to draw conclusions and settle the dispute in literature. To fully understand occurrence of LME, the fundamental transport mechanism needs to be uncovered.

5.3 Methodology

Thermomechanical Testing

Elevated temperature tensile testing for LME observation was completed using a Gleeble 3500 on the TRIP 1100 material. Testing was carried out using the sample geometry in Fig. 5-1(a) on temperatures ranging from 600 °C – 900 °C. Testing until fracture was completed for both coated and uncoated samples to observe the effects of LME on load carrying and ductility. The specimen was heated at a rate of 1000 °C/s and a strain rate of 1 /s was used to for mechanical loading. The test cases and parameters are summarized in Table 5-1.

***Table 5-1** Test cases for thermomechanical testing of the TRIP 1100*

Test Case	Test Temperature	Heating Rate	Strain Rate
A	600 °C	1000 °C/s	1 /s
B	700 °C		
C	800 °C		
D	900 °C		

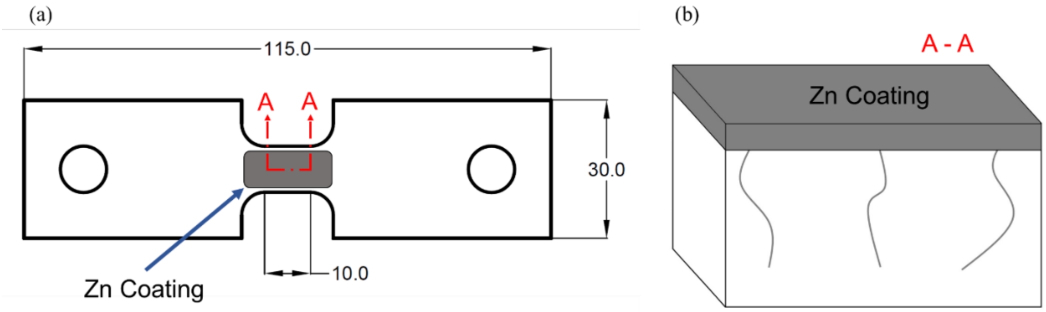

***Figure 5-1** Schematic of (a) elevated temperature uniaxial tension sample geometry (b) cross-section for Zn characterization*

Interrupted elevated temperature tensile testing was also carried out to observe the formation of LME cracks with increasing applied stress. An unloaded case and three distinct stress cases as summarized in Table 5-2 were selected to observe the effects of stress on the Zn diffusion. Samples were heated to a test temperature of 600 °C and isothermally held. All samples were held at the designed thermomechanical state for 1 s then unloaded and quenched as shown schematically in Fig. 5-2.

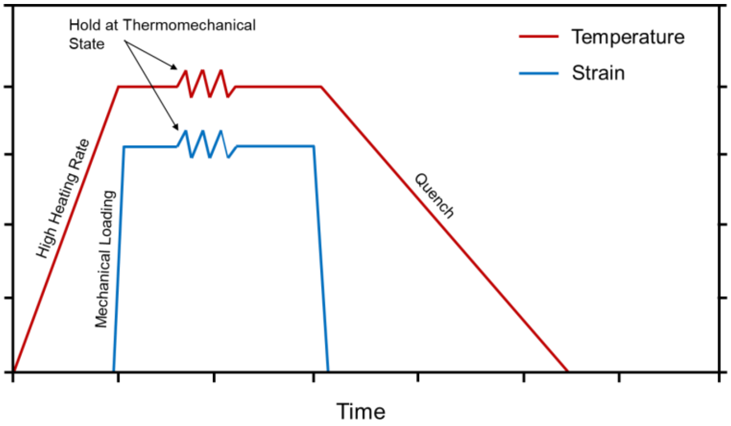

***Figure 5-2** Schematic representation of heating and loading cycle of interrupted test cases*

***Table 5-2** Interrupted test cases at a test temperature of 600 °C*

	No Stress	**Case 1**	**Case 2**	**Case 3**
Applied Stress	0 MPa	190 MPa	305 MPa	420 MPa

After thermomechanical testing, the fracture surface was examined by SEM using similar methodology to Chapter 3.2. The gauge area of the interrupted testing samples was cross-sectioned and inspected for Zn diffusion into the grain boundaries as shown in Fig. 5-1(b). Zn concentration was characterized using electron probe micro-analyzer for elemental mapping and the thin slice method [57] with line scans was used to construct the diffusion depth profile.

Diffusion Model

A model for stress-assisted grain boundary diffusion was set-up using a semi-infinite bicrystal under external tensile stress as shown in Fig. 5-3. In the schematic, the Zn coating is treated as a thin film constant source (c_o) on the free surface and the grain boundary is oriented perpendicular to the free surface with a thickness of δ. In addition to the classic grain boundary diffusion fluxes caused by a concentration gradient, the application of the external load σ_o causes an additional diffusion flux driven by a chemical potential gradient [57,58].

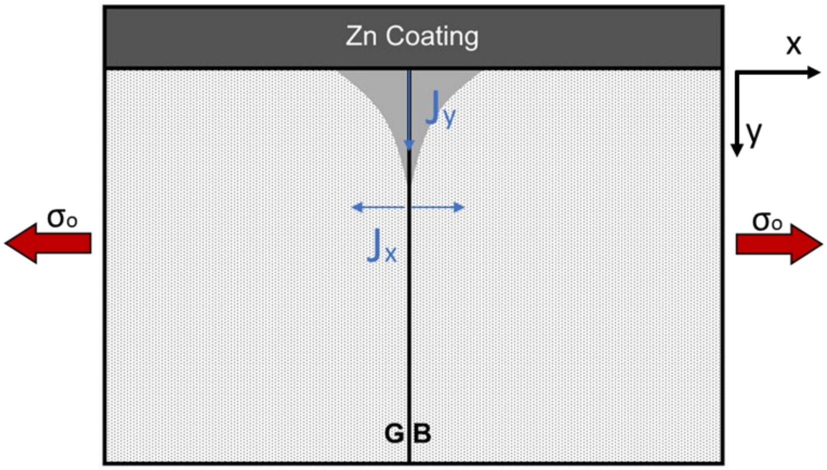

Figure 5-3 *Schematic representation of semi-infinite bicrystal under external stress*

The diffusion fluxes of the grain boundary can be represented as the sum of the two contributions associated with concentration and stress and the flux into the bulk grain:

$$J_y = -D_b\left(\frac{\partial c_{gb}}{\partial y} - \frac{c_{gb}\Omega}{kT}\frac{d\sigma}{dy}\right) \tag{5 − 1}$$

$$J_x = -D\frac{\partial c}{\partial x} \tag{5 − 2}$$

Where D_b and D are the diffusion coefficients (used as constants since it is an isothermal condition) for the grain boundary and bulk respectively, c_{gb} and c are the concentrations for the grain boundary and bulk respectively, Ω is the atomic volume of the diffusant, and σ is the stress function acting on the grain boundary. In accordance to Fisher's [49] description of grain boundary diffusion, Eq. 5-1 represents the diffusion flux along the grain boundary while Eq. 5-2 represents the diffusion flux out of the grain boundary and into the bulk material. It is important to note that the stress flux term does not appear in Eq. 5-2 since there is no stress gradient in the x-direction. The established diffusion flux equations can now be applied in the conservation of mass:

$$\frac{\partial c_{gb}}{\partial t} = \frac{-\partial J_y}{\partial y} - \frac{2}{\delta}J_x \tag{5 − 3}$$

Substituting Eq. 5-1 and Eq. 5-2 into Eq. 5-3 gives the generalized governing equation for stress-assisted grain boundary diffusion as:

$$\frac{\partial c_{gb}}{\partial t} = D_b\frac{\partial}{\partial y}\left[\frac{\partial c_{gb}}{\partial y} - \frac{c_{gb}\Omega}{kT}\frac{\partial\sigma}{\partial y}\right] + \frac{2D}{\delta}\frac{\partial c}{\partial x} \tag{5 − 4}$$

Given the test temperature is low relative to the material's melting temperature, the diffusion to the bulk is minimal according to Harrison's [53] classification of grain boundary diffusion kinetics. Therefore, the second term in Eq. 5-4 can be neglected and Eq. 5-4 modified to the form:

$$\frac{\partial c_{gb}}{\partial t} = D_b \frac{\partial}{\partial y}\left[\frac{\partial c_{gb}}{\partial y} - \frac{c_{gb}\Omega}{kT}\frac{\partial \sigma}{\partial y}\right] \qquad (5-4a)$$

In Eq. 5-4a, the first term in the brackets represents the diffusion caused by the concentration gradient while the second term describes the stress diffusion. The boundary conditions and initial conditions from the system illustrated in Fig. 5-3 can be mathematically described as:

$$c_{gb}(0,t) = c_o \qquad (5-5a)$$

$$\frac{\partial c_{gb}(y_{end},t)}{\partial y} = 0 \qquad (5-5b)$$

$$c_{gb}(y > 0, 0) = 0 \qquad (5-5c)$$

Notably, when no stress diffusion is present, the system takes the classic form of an infinite source diffusion equation. Lastly, the stress function proposed in Klinger's model was adapted into the present work, which produces:

$$\frac{\partial c_{gb}}{\partial t} = D_b \frac{\partial^2 c_{gb}}{\partial y^2} - D_b \frac{\Omega \sigma_o}{kT}\frac{\partial c_{gb}}{\partial y} Z'(s) \qquad (5-6)$$

Where σ_o is the applied stress and $Z'(s)$ (where $s = s(y,t)$) is the derivative of the shape function developed by Klinger to model the stress gradients produced by the grain boundary wedge formation. A detailed derivation and description of $Z'(s)$ is given in [25]. Constant values were taken from the experimental conditions or relevant literature and are summarized in Table 5-3. When the stress term in Eq. 5-6 is exceedingly small or 0 the grain boundary concentration follows a complementary error function distribution. However, in the general case of stress-assisted diffusion, Eq. 5-6 was solved numerically.

Table 5-3 *Summary of diffusion constants used to solve diffusion model*

Constant	Value
$\boldsymbol{D_b}$	6.89 x 10^{-13} m^2/s [112]
$\boldsymbol{\sigma_o}$	Values from Table 5-2
$\boldsymbol{T}$	600 °*C*

The finite difference method was used to numerically solve for the grain boundary concentration [54]. The final discretized equation is shown in Eqn. 5-7 where the *j* superscript is the time indices, and the *i* subscript is the space indices.

$$\frac{{c_{gb}}_i^{j+1} - {c_{gb}}_i^j}{\Delta t} = D_b \frac{{c_{gb}}_{i+1}^j - 2 * {c_{gb}}_i^j + {c_{gb}}_{i-1}^j}{\Delta x^2} - D_b \frac{\Omega \sigma_o}{kT} \frac{{c_{gb}}_i^j - {c_{gb}}_{i-1}^j}{\Delta x} Z'(s) \qquad (5-7)$$

To reach the converged solution, a spatial step size of $\Delta x = 0.1$ was used. The finite difference equation showed consistency with the partial differential equation since the truncation error approached zero as $\Delta x \to 0$ and $\Delta t \to 0$. The time step was determined using the minimum step size required for stability [113] as is shown in Eq. 5-8. Details on the consistency and stability analysis of the finite difference equation is provided in Appendix A and B, respectively. A $\Delta t = 0.005$ time step was used.

$$\Delta t < \frac{\Delta x^2}{\left(2D_b + \Delta x \frac{\Omega \sigma_o}{kT} Z' D_b\right)} \qquad (5-8)$$

5.4 Results and Discussion

Thermomechanical Testing

Results of the thermomechanical testing showed the occurrence of LME in the Zn coated samples. Compared to the uncoated counter part, the coated samples failed prematurely as shown in Fig. 5-4. Initially, both sample conditions behave similarly until LME starts to occur, at which point the coated sample shows a loss in ductility and load carrying. From the elevated temperature tensile testing curves in Fig. 5-4 is its clear LME had the most significant effect during the high temperature 800 °C case; the coated and uncoated conditions for the 600 °C appear more similar. Given the sparse reports of LME at temperatures below 700 °C and the similarly of the sample conditions, this case was explored in more detail.

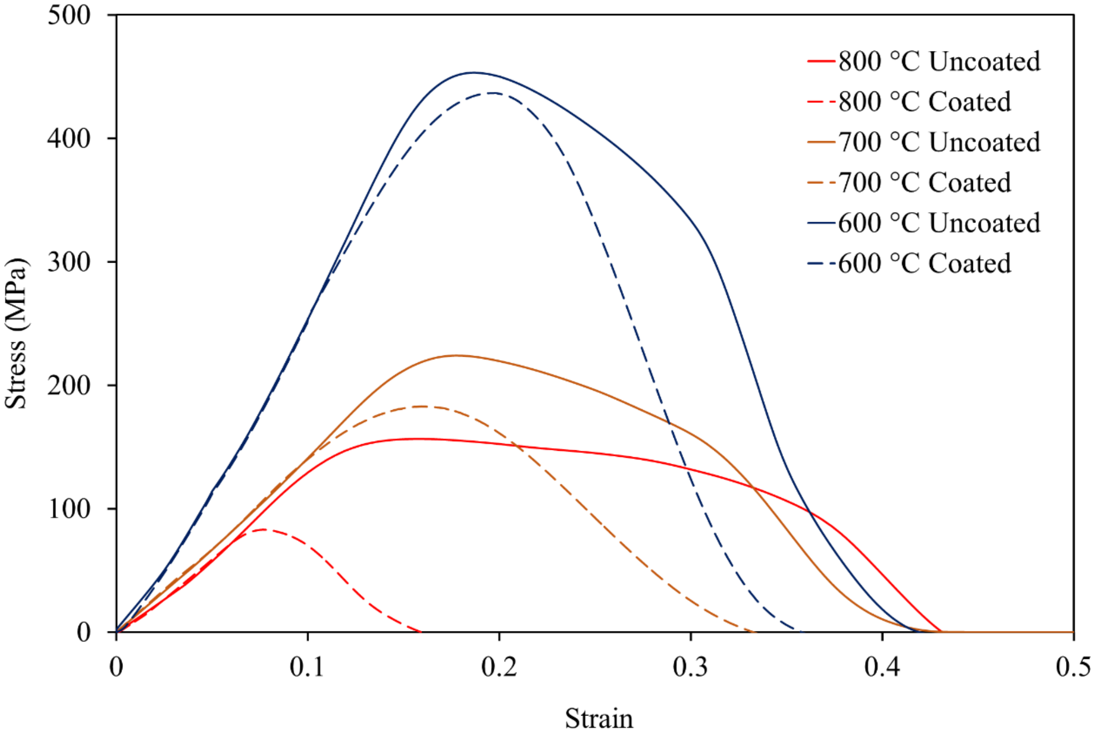

Figure 5-4 *Thermomechanical testing results of the coated and uncoated samples*

The fracture surface of the 600 °C sample was inspected to determine the occurrence of LME. The fracture surface in Fig. 5-5(a) shows a clear distinction in fracture between the top (Zn coated side) and bottom (bare steel side). Higher magnification images of the top region show the evidence of LME fracture such as the presence of Zn as well as an intergranular brittle morphology. Conversely, the bottom portion of the fracture exhibited ductile characteristics such as cup and cone features and dimples. Therefore, LME did occur during the thermomechanical tensile testing, but it did not fully dominate the failure mode. LME was initiated and propagated until the cross section of the material was sufficiently reduced that it could not bear of the load of testing leading to a ductile base material failure.

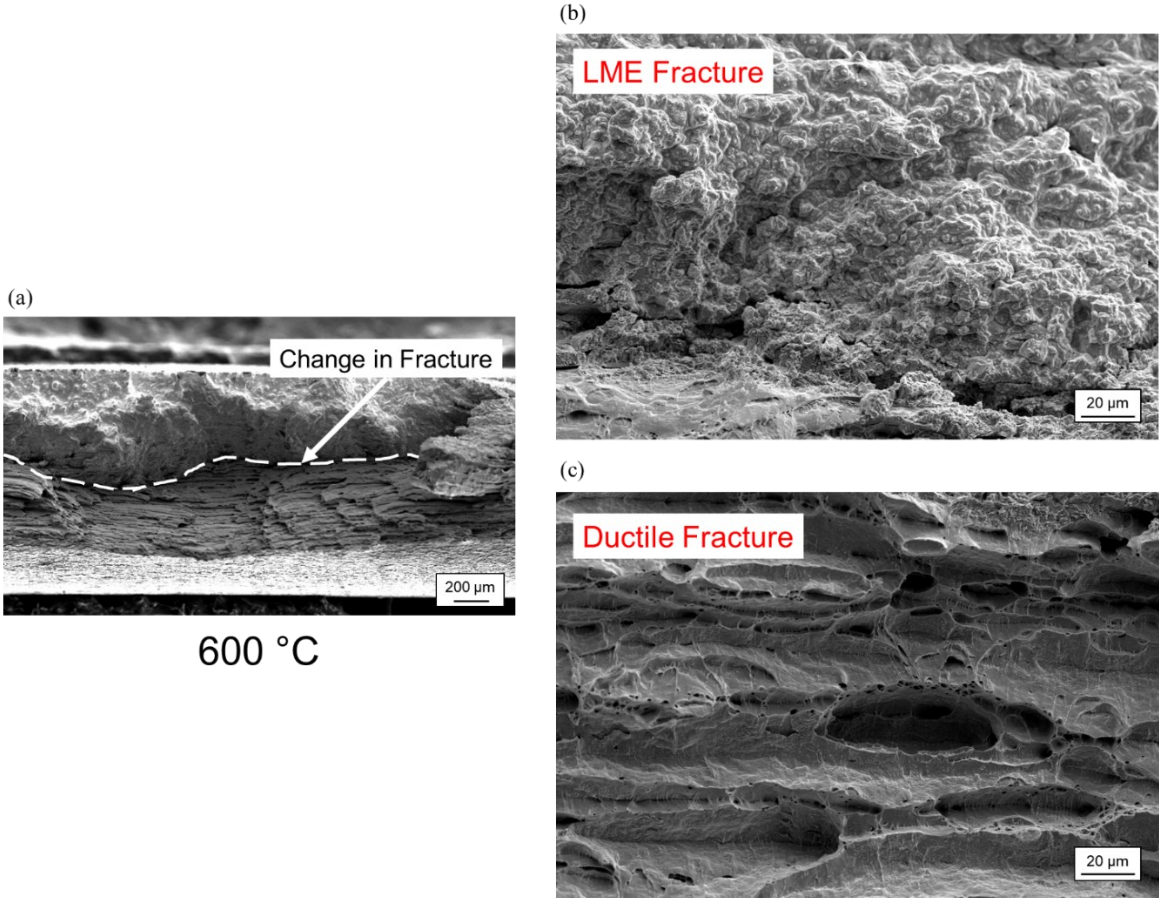

Figure 5-5 *(a) fracture surface of 600 °C case showing distinct fracture regions (b) LME fracture region (c) ductile fracture region*

A cross-section of the top fracture region was inspected to further confirm the occurrence of LME. From the cross-section images shown in Fig. 5-6, the Zn coating clearly extends onto the fracture surface. In a higher magnification image, LME cracks showing the typical jagged intergranular morphology are seen branching from the primary fracture surface. Additionally, secondary LME cracks were observed adjacent to the fracture. Clearly, from the results of the fractographic study LME occurred in the low temperature 600 °C case. However, it did not dominate the failure mode of the sample which explains the extended elongation of the 600 °C case relative to the high temperature cases, where LME is more dominant according to literature [15,31].

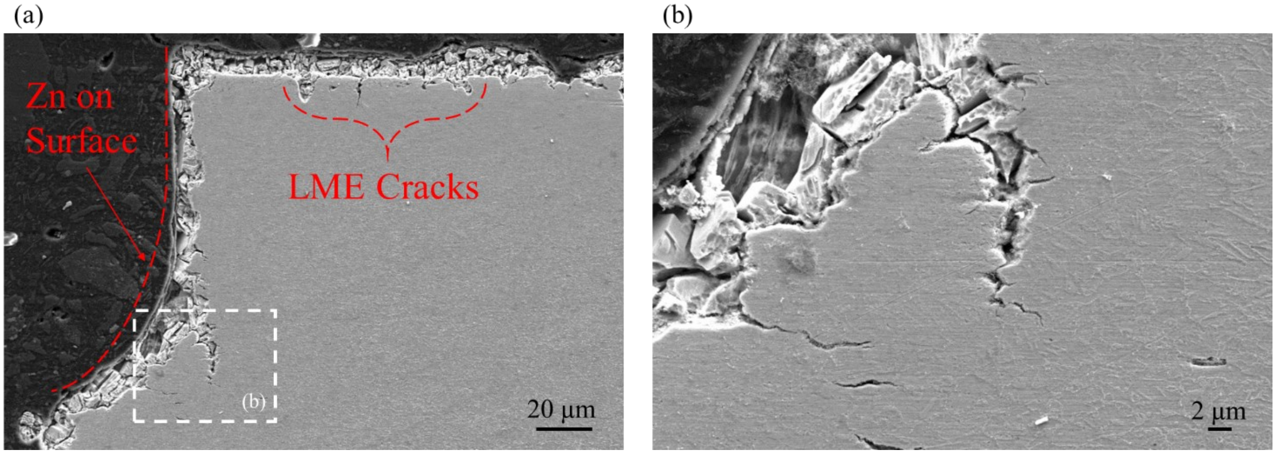

Figure 5-6 *(a) cross-section of 600 °C fracture surface showing Zn on the surface and secondary LME cracks (b) branding LME crack from primary fracture surface*

A comparison between the load carrying of the coated and uncoated samples at varying temperature reveals the thermomechanical window the occurrence of LME in this material. The elevated temperature tensile testing was extended to higher temperatures to provide a complete window. Plotting the critical stress of LME occurrence (maximum load of the coated samples) versus temperature in Fig. 5-7 shows the thermomechanical region where LME occurs. From Fig. 5-7, the critical stress clearly depends on temperature. At low temperatures, the stress required for the onset of LME is high but sharply decreases with increasing temperature. However, at temperatures over 800 °C the critical stress becomes stagnant until LME is observed not to occur over 900 °C. The decreasing critical stress with temperature indicates the dominate role of stress for the onset of LME at low temperatures, until it becomes relatively insignificant above 800 °C. The critical stress for LME at 900 °C is remarkably similar to the critical stress at 800 °C meaning LME will occur easily whereas at the low temperature 600 °C a significant amount of stress is required to induce the onset of LME.

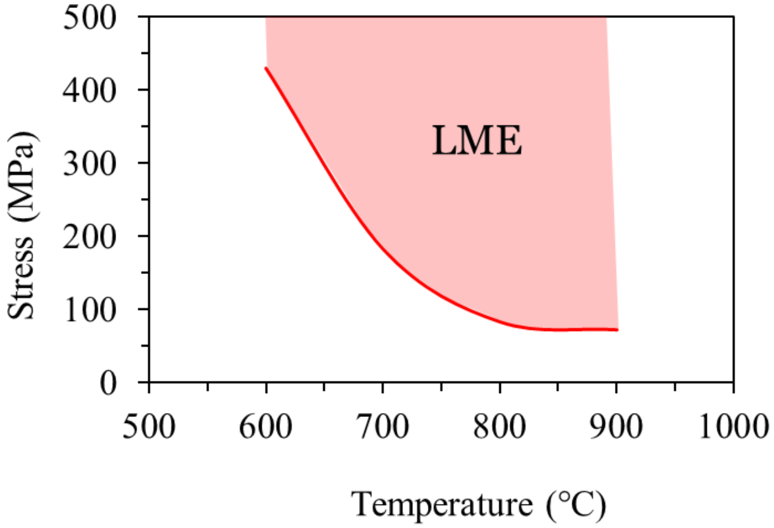

Figure 5-7 *Critical stress for the onset of LME and thermomechanical window*

The thermomechanical testing clearly showed the occurrence of LME to be co-dependent on stress and temperature. In low temperature conditions, a sufficient amount of stress is necessary to trigger LME. This observation explains the occurrence of LME in the SCHAZ from Chapter 4, where the electrode misalignment introduced mechanical distortion. These thermomechanical findings about the nature of the LME phenomenon are consistent with the previous work done by Beal et al. [36] and Gordon and An [24]. However, the critical stress still lacks a mechanistic description detailing its role in the onset of LME and the proposed diffusion mechanism. To examine the role of stress in detail, interrupted elevated tensile testing of the 600 °C case was carried out to observe the effects of applied stress on the Zn grain boundary diffusion and LME crack formation.

As stress is applied and increased, Zn grain boundary penetration is enhanced as shown in Fig. 5-8. In Fig. 5-8(a) the no stress condition is displayed, and it shows little Zn diffusion into the steel grain boundaries. However, as stress is introduced, the Zn concentration in the substrate increases, enabling an LME crack to form as shown in Fig. 5-8(e). Furthermore in Fig. 5-8(e), this process can be observed to be repeating, as liquid Zn penetrates the crack and a diffusion or penetration zone is seen to form ahead of the LME crack tip, which matches the LME microevents mechanism proposed by Razmpoosh et. al [35]. As stated in that description of LME, grain boundary diffusion precedes the formation of LME cracking. These observations confirm LME as a diffusion-based phenomenon and validate the Gordon-An model, which proposed a penetration zone before LME crack formation. Additionally, it is shown the application of external stress plays a critical role in Zn diffusion penetration and onset of LME. This observation further confirms the Gordon-An model which postulated the penetration zone (and thus LME crack) formation depends on both temperature and stress. In this instance, for the given test temperature, there is a minimum amount of stress required to facilitate the Zn diffusion and penetration.

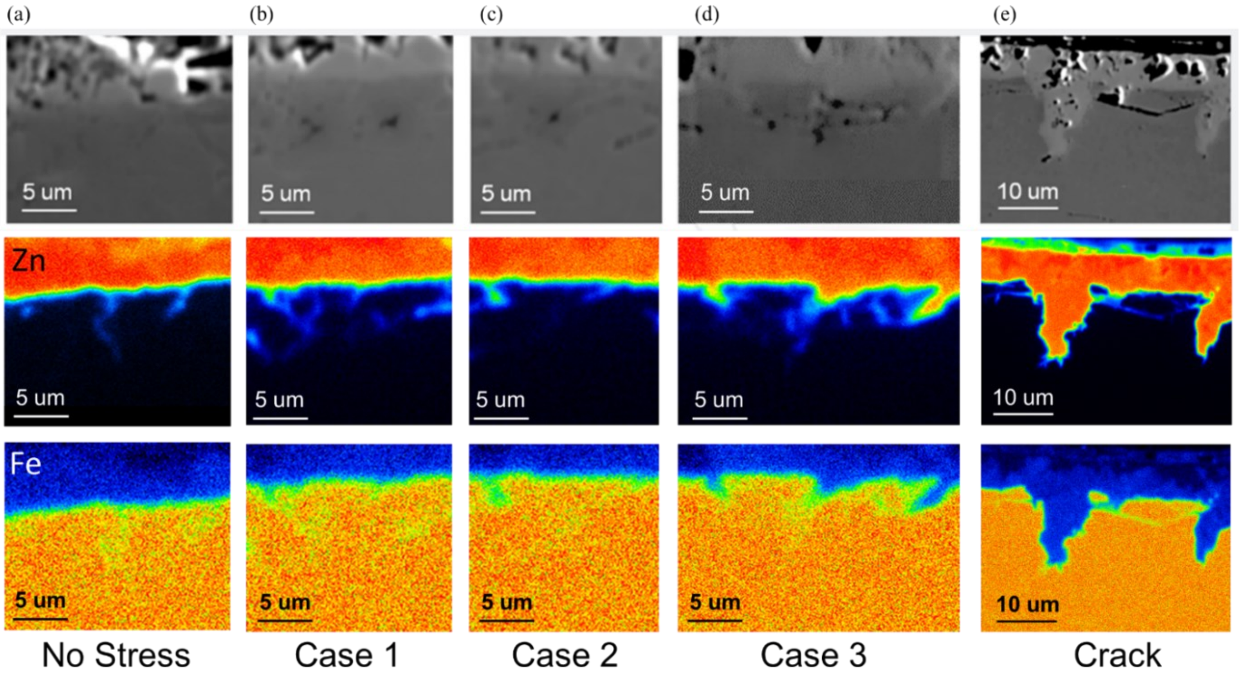

Figure 5-8 *SEM images and elemental EPMA maps showing concentration for Zn and Fe in (a) No Stress (b) Case 1 (c) Case 2 (d) Case 3 (e) LME crack formation*

Stress-assisted Diffusion Mechanism

To confirm the presence of an additional stress diffusion flux, the Zn concentration depth profile was analyzed. The experimental depth measurements were compared to the depth profile from the numerical results. The experimental measurements for the no stress condition matches the complementary error function distribution, as shown in Fig. 5-9(a). This observation is expected as the complementary error function is the solution to the diffusion governing equation [54]. However, as stress increases, the experimental distribution is no longer in the form of the error function and takes a sigmoidal shape. Since the complementary error function is no longer the experimental distribution, it can therefore be said that the governing equation has changed, thus indicating the addition of a stress flux term. To further investigate the nature of the experimentally confirmed stress flux, the numerical solution to Eq. 5-6 plotted against the normalized depth direction ($Y = y/y_o$ where y_o is the diffusion length $\sqrt{D_b t}$) is shown in Fig. 5-9(b). Once again, the no stress case is simply an complementary error function distribution, but as the stress diffusion term in Eq. 5-6 increases, the numerical solution deviates from the error function until a distinct sigmoidal function is formed. The shift in the numerical solution with the introduction of stress matches the behavior of the experimental solution and each case is directly compared in Fig. 5-9(c) – (f). The comparison between the experimental and numerical plots shows a high degree of agreement which confirms the inclusion of the stress diffusion flux and a stress-assisted diffusion mechanism for the onset of LME. As stress increased, the stress diffusion flux component of Eq. 5-6 became more dominant, and the solution deviated from the error function. Furthermore, since Klinger's model was used to describe the stress function, these results provide an experimental confirmation for his model. At the onset of LME, grain boundary wedging provides a stress gradient along the grain boundary which is integral to the development of the stress diffusion flux.

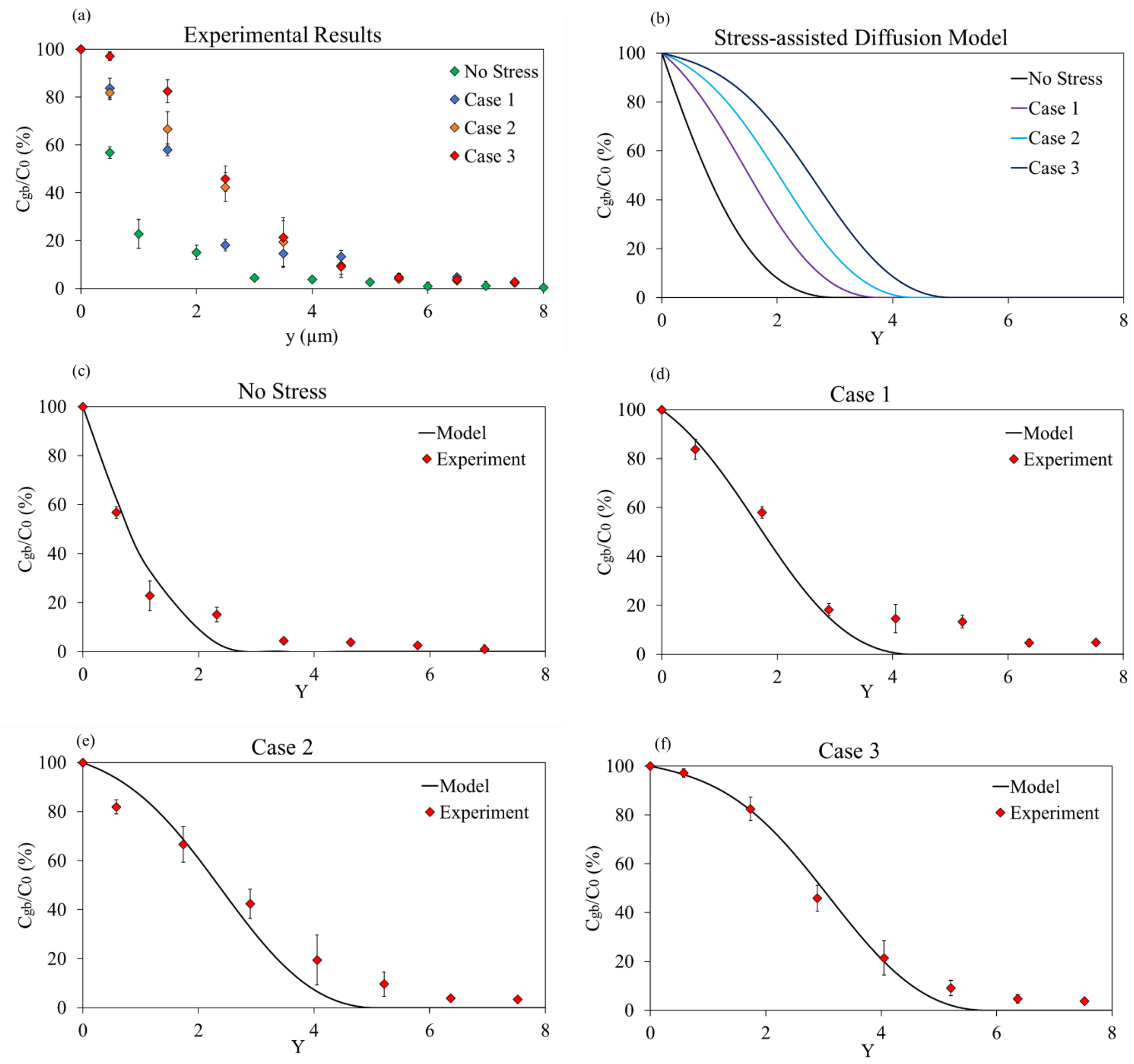

Figure 5-9 *Diffusion depth profiles for (a) experimental solution for all cases (b) numerical solution for all cases (c) numerical and experimental comparison for No Stress case (d) numerical and experimental comparison for Case 1 (e) numerical and experimental comparison for Case 2 (f) numerical and experimental comparison for Case 3*

From this work, new insights into the thermomechanical nature of the LME mechanism have been uncovered. Under the no stress condition, typical grain boundary diffusion behavior is observed but that is not sufficient to facilitate the required Gordon-An penetration zone for LME crack formation. With the application of external loading and formation of a stress gradient, a stress-assisted diffusion mechanism takes place until the penetration zone develops into an LME crack. This leaves an intergranular microcrack which is filled with the liquid embrittler. This mechanism is summarized graphically in Fig. 5-10. The shown mechanism also provides insight into studies replicating manufacturing conditions [114,115] that showed LME was triggered with increased external loading.

The results from this study establish LME as a diffusion-based phenomenon, but also explains observations of a liquid embrittler at the LME crack tip. From Fig. 5-8(d), a liquid phase forms at the grain boundary wedge, before opening to form a crack. This leaves the appearance of a liquid phase at the crack tip, which explains recent observations of liquid separation at the opening of LME cracks [33]. With diffusion identified as the primary transport mechanism, further insights can be given to recent experimental studies on LME susceptibility. Razmpoosh et. al [116] showed that grain boundaries with high misorientation angle are highly susceptible to LME while low angle boundaries are resistant, which follows LME as diffusion based since previous work studying grain boundaries have shown high angle boundaries to have higher diffusivity [117,118]. Furthermore, observations showing austenite grains to be more susceptible to LME are also consistent with a diffusion-based mechanism. Literature has shown that not only does austenite have a higher grain boundary diffusivity than ferrite, but also has a lower bulk diffusivity [119]. This means that at high temperatures the lateral diffusion into the bulk is still relatively small, leading to further grain boundary penetration. Finally, in a recent study, Boron was identified as an effective alloying element to suppress LME [120] due to its effect on suppressing grain boundary diffusion [121,122].

The findings from this work confirm the LME transport mechanism as stress-assisted diffusion and build on previous fundamental descriptions of LME. Several aspects of the Gordon-An model were observed and confirmed in this work including the observation of a penetration zone before LME crack formation. The presence of an additional stress diffusion flux as the LME transport mechanism was observed experimentally and confirmed with the numerical model. Additionally, Klinger's proposed model of grain boundary stress gradient was validated for LME in the Fe/Zn system. The results from this study uncover the role of thermomechanical state for the LME onset mechanism and provide insights which are critical for thermomechanical material processing of susceptible LME couples.

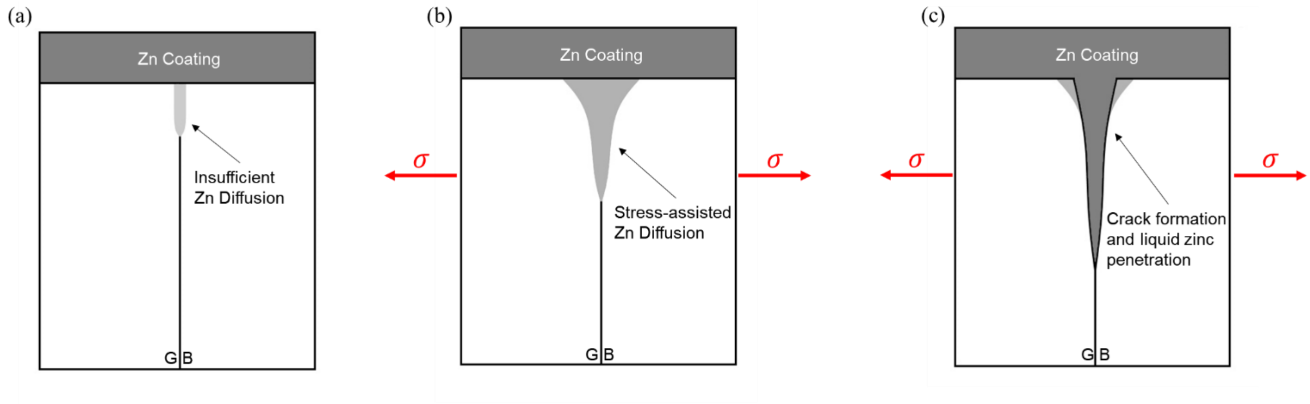

Figure 5-10 *Conceptual model for the role of stress in the onset of LME (a) Zn diffusion is insufficient to cause LME (b) stress is added to enhance the diffusion process and facilitate Zn penetration (c) The LME crack is formed*

The thermomechanical state is critical to LME formation since it controls the fundamental diffusion process that leads to LME. The stress-assisted diffusion LME transport mechanism determined by this work demonstrates the significance of both temperature and stress for Zn penetration and crack formation. The fundamental findings of this study show that to control the occurrence of LME, the diffusion kinetics must be controlled. The traditional thought of static susceptible temperature ranges for LME is not accurate, as additional factors such as stress or activation energy are interconnected to affect the diffusion kinetics.

Comprehensive Overview of LME in RSW

The results of this study showed that stress enhances the embrittler penetration in the LME phenomenon. Additionally, LME was confirmed as a stress-assisted diffusion mechanism. These novel and impactful insights are significant to the fundamental research of LME, however their relation to the occurrence of LME during the RSW process is of practical interest. The LME critical stress plot in Fig. 5-7 showed the thermomechanical window for the onset of LME. In the RSW process LME will occur when the material at the Zn coating interface meets this thermomechanical state. For example, the peak temperature and stress values from the Sysweld® simulation in Fig. 4-12 are superimposed on the critical stress plot in Fig. 5-11:

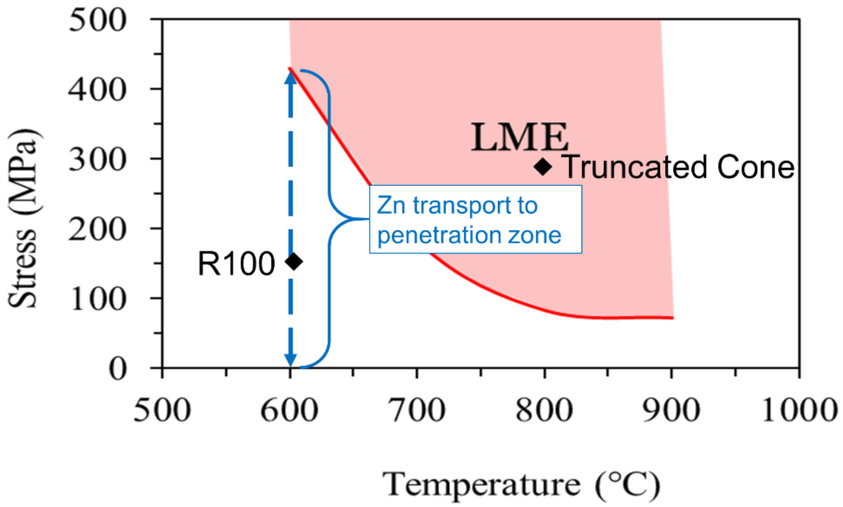

Figure 5-11 *Predicted radius and truncated cone thermomechanical state from Chapter 4 Fig. 4-12 superimposed on the critical stress plot*

Clearly, it can be seen that the truncated cone exceeds the thermomechanical state for LME and thus LME cracks were observed in the welds. However, in the case of the radius electrode the stress was not sufficient at the given temperature for the formation of LME cracks. The lack of stress led to insufficient diffusion of Zn and thus was stuck in region below the critical stress line where the penetration zone is forming. This behaviour would be akin to the Zn penetration in Fig. 5-8(b) where Zn penetration was enhanced with the presence of some stress, but not enough for an LME crack to form. In Chapter 4, LME cracks were observed to occur in instances of elevated temperature and stress. However, in the case of angular misalignment welding, LME was observed at relatively low temperature in a highly distorted region. Based of the results from this chapter, a reasonable conclusion is the stress associated with the distortion enhanced the Zn penetration leading to LME at low temperatures. Typically, at SCHAZ temperatures the stresses provided exclusively by the RSW process are not high enough to meet the requirements for LME. This is similar to regions that are at elevated temperatures during the RSW process, but do not experience stress so the Zn diffusion is insufficient for LME to occur. A schematic explaining the formation of LME cracks during RSW is shown in Fig. 5-12.

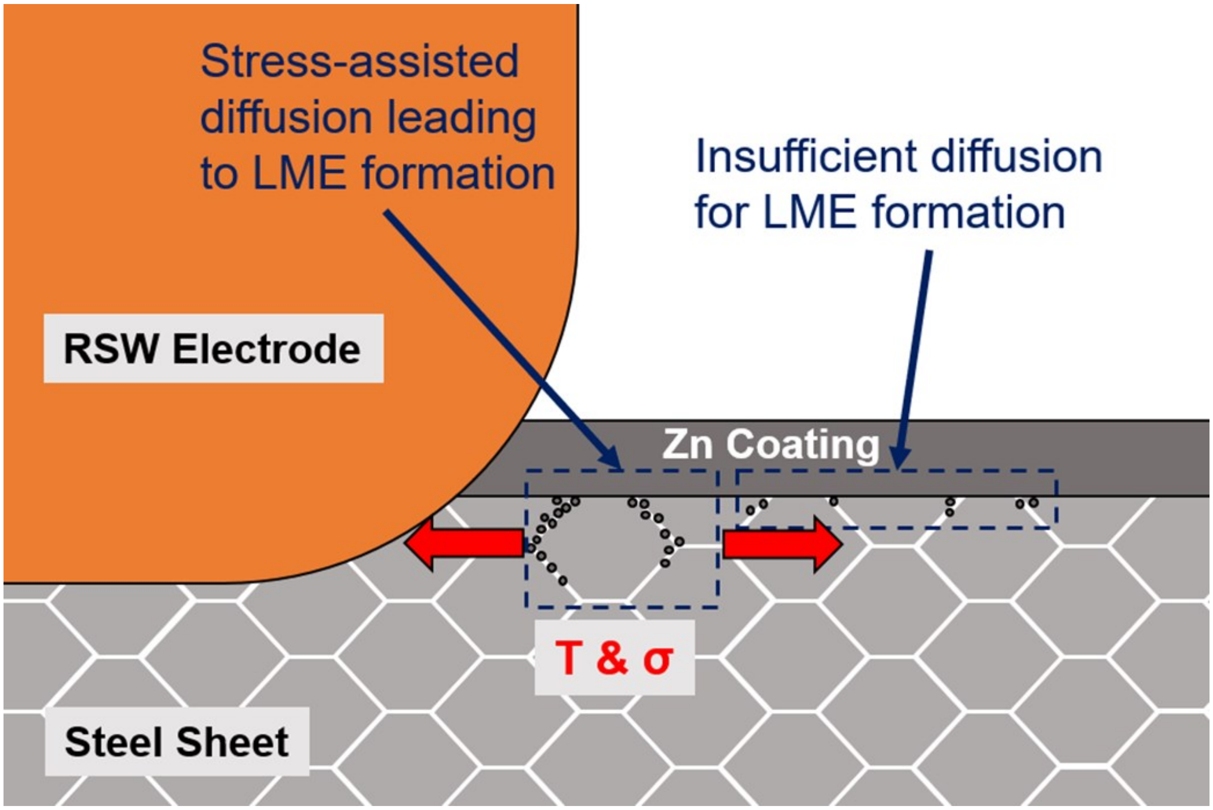

Figure 5-12 *conceptual model for the occurrence of LME in RSW showing the significance of temperature and stress for the grain boundary diffusion mechanism leading to LME cracks*

Fig. 5-12 shows that LME occurs in the RSW process when stresses along with the temperatures of the process lead to stress-assisted diffusion, and thus the formation of LME cracks. Due to the high operating temperatures of the RSW process and the associated stress mechanisms identified in Chapter 4, the diffusion process leading to LME is strongly enhanced, making the process highly susceptible to the occurrence of LME resulting in detrimental cracking.

With a fundamental understanding of the occurrence of LME in the RSW, mitigation techniques from a process perspective can be developed to target the exact mechanisms of formation. The methods in Chapter 4 showed, in general, lowering temperature and stress at the electrode-sheet interface will prevent LME cracks. It is now clear this is due to the slowing of the diffusion kinetics and thus lack of embrittler penetration.

5.5 Summary

This chapter presented novel and insightful findings to the field of LME in RSW as well as the area of LME fundamentals. The conclusions from this chapter can be summarized as:

(a) A critical stress exists for the occurrence of LME in the Fe/Zn system which is dependent on temperature. Therefore, the onset of LME is co-dependent on stress and temperature, meaning the susceptible temperature range for LME is not static as previously thought

(b) Interrupted elevated temperature testing showed stress enhanced the Zn grain boundary penetration, indicating that stress plays a key role in the transport mechanism leading to LME

(c) The fundamental transport mechanism for the onset of LME was identified to stress-assisted diffusion. For the first time, this theory was observed experimentally and described in detail through mathematical diffusion modeling

(d) RSW is a highly susceptible LME process due to the high operating temperatures and stresses at the electrode-sheet interface leading to enhanced diffusion of the Zn embrittler and the formation of LME cracks

Chapter 6

Conclusions and Future Research

6.1 Conclusions

The present study revealed new insights into the onset mechanism for the LME phenomenon. For the first time, the fundamental embrittler transport mechanism was concluded to be stress-assisted grain boundary diffusion. This fundamental contribution to LME research was used to explain the high LME susceptibility in RSW. The high temperatures and stresses associated with the RSW process led to enhanced embrittler diffusion resulting in the occurrence of LME cracking. Thermal stresses associated with electrode collapse and electrode release resulted in the formation of LME shoulder cracks and centre cracks, respectively. Mitigation techniques to manage these thermomechanical mechanisms were developed for LME crack reduction. Detrimental LME cracks defined according to their depth and location can now be targeted effectively. Overall, the present study provided novel and applicable findings on the occurrence of LME cracks in RSW, and the major conclusions are described in detail below:

1. LME cracks were observed to affect the joint tensile shear strength. LME cracks located in the loaded region and of considerable size (>400 μm) were identified to lead to a detrimental effect on joint strength. Using these crack parameters, detrimental cracks were defined and can now be targeted for reduction.

2. Electrode collapse into the AHSS creates sudden cooling leading to thermal stresses in the weld shoulder leading to the formation of LME cracks. Conversely, the formation of centre cracks was determined to be caused by thermal shock at the electrode release. Both mechanisms reveal the significance of thermomechanical state for the onset of LME.
3. Distinct formation mechanisms were found for shoulder and centre LME cracks. Therefore, the reduction of a shoulder cracks will only occur by addressing the stresses associated with the electrode collapse, whereas centre cracks require mitigation of the thermal shock at electrode release.
4. Radius RSW electrodes were observed to significantly reduce detrimental LME cracks due to the consistent contact of the electrode. The consistent contact sustained a low temperature and prevented tensile stresses from electrode collapse. Furthermore, a variable input current was successful at withdrawing heat from the weld prior to electrode release, eliminating the thermal shock mechanism and reducing centre cracks. However, in the case of large angular electrode misalignment, LME cracks were still observed in sub-critical temperatures. In largely distorted regions, the low temperature was not sufficient to suppress the onset of LME. Overall, the temperature and stress of the RSW process was manipulated to reduce the occurrence of LME.
5. Temperature and stress for the onset of LME were observed to be co-dependent. The stress required for the onset of LME was found to decrease with increasing temperature. Through interrupted elevated temperature tensile testing, the formation of LME was observed in detail which revealed Zn penetration increased with increasing stress. The fundamental transport mechanism was identified as stress-assisted grain boundary diffusion, as confirmed by numerical modeling and experimental observations. Examining the kinetics

and governing equations for stress-assisted grain boundary diffusion revealed the role of stress and temperature is to enhance the embrittler penetration into the AHSS sheet.

6.2 Areas of Future Research

The results and conclusions of this study provide several pathways to future LME research. Although this study provided evidence for a stress-assisted grain boundary diffusion mechanism, the diffusion kinetics are complex and can benefit from further research. The stress along the grain boundary is a critical parameter for the diffusion kinetics. Progressing towards a further understanding of the stresses along the grain boundary would be beneficial to future LME research. A diffusion-mechanical model combining the microstructural stresses and diffusion kinetics would provide further insights and predictability for LME. Furthermore, the results from this study are insightful for the onset of LME, however the propagation remains unclear. After initial crack formation, the stress state of the microstructure changes significantly which would strongly influence the diffusion kinetics. The development of a diffusion-mechanical model coupled with experimental observations of LME crack growth is a feasible path for further understanding of the transport mechanism in LME crack propagation.

Another area for further research is RSW process monitoring for energy accumulation and the occurrence of LME. Literature has stated that a heat input threshold exists for the occurrence of LME. With the results from this work, the specific mechanisms leading to the necessary conditions for LME are uncovered but staying below a threshold energy level in the RSW system may mitigate these specific mechanisms, such as the electrode collapse event. Accompanying the process monitoring with in-situ high speed video would allow the detection of the exact instant of LME formation. Developing a standardized method to determine the energy thresholds for LME in specific material types and stack-ups would be practically important to industry as well as deliver insights to the manufacturing technology. This generalized methodology could be further expanded into standardized testing for LME susceptibility for given materials and material stack-ups.

As shown in the literature review, the knowledge surrounding the effects of LME crack on mechanical joint performance is insufficient. This study provided a novel yet introductory understanding of how LME cracks affect lap shear joint performance. For further industrial application, the effect on fatigue and high strain rate testing should be investigated. With the knowledge of LME crack formation determined from this study, LME cracks can be effectively targeted once the critical characteristics are identified for fatigue and high strain rate testing.

References

[1] M. Ghosh, K. Kumar, R.S. Mishra, Mater. Sci. Eng. A 528 (2011) 8111–8119.

[2] L. Mújica Roncery, S. Weber, W. Theisen, Scr. Mater. 66 (2012) 997–1001.

[3] S.S.Nayak, Y.Zhou, V.H.B. Hernandez, E.Biro, Trends Welding,Research,Proceedings 9th Int. Conf. (2012) 641–649.

[4] M. Xia, Z. Tian, L. Zhao, Y.N. Zhou, ISIJ Int. 48 (2008) 483–488.

[5] P. Lan, J. Zhang, Mater. Sci. Eng. A 707 (2017) 373–382.

[6] H. Liu, J. Liu, B. Wu, Y. Shen, Y. He, H. Ding, X. Su, Mater. Sci. Eng. A 708 (2017) 360–374.

[7] J.E. Jin, Y.K. Lee, Acta Mater. 60 (2012) 1680–1688.

[8] R. Ueji, N. Tsuchida, D. Terada, N. Tsuji, Y. Tanaka, A. Takemura, K. Kunishige, Scr. Mater. 59 (2008) 963–966.

[9] Z.H. Cai, H. Ding, R.D.K. Misra, Z.Y. Ying, Acta Mater. 84 (2015) 229–236.

[10] J. Han, Y.K. Lee, Acta Mater. 67 (2014) 354–361.

[11] H. Karbasian, A.E. Tekkaya, J. Mater. Process. Technol. 210 (2010) 2103–2118.

[12] M. Abbasi, M. Naderi, A. Saeed-Akbari, Mater. Des. 45 (2013) 1–5.

[13] E. Billur, T. Altan, Stamp. J. (2013).

[14] D. Bhattacharya, Mater. Sci. Technol. (United Kingdom) 34 (2018) 1809–1829.

[15] G. Jung, I.S. Woo, D.W. Suh, S.J. Kim, Met. Mater. Int. 22 (2016) 187–195.

[16] C. Beal, X. Kleber, D. Fabregue, M. Bouzekri, Mater. Sci. Eng. A 543 (2012) 76–83.

[17] W. Rostoker, J.M. McCaughey, H. Markus, Corp., New York (1960).

[18] N.S. Stoloff, T.L. Johnston, Acta Metall. 11 (1963) 251–256.

[19] A.R.C. Westwood, M.H. Kamdar, Philos. Mag. 8 (1963) 787–804.

[20] E.E. Glickman, Interface Sci. 11 (2003) 451–459.

[21] P.C. Hancock, M.B. Ives, Can. Metall. Q. 10 (1971) 207–211.

[22] S.P. Lynch, Acta Metall. 36 (1988) 2639–2661.

[23] 14 (1979) 365–370.

[24] P. Gordon, H.H. An, Metall. Trans. A 13 (1982) 457–472.

[25] L. Klinger, E. Rabkin, Acta Mater. 55 (2007) 4689–4698.

[26] W.M. Robertson, Trans. AIME 236 (1966) 1478–1482.

[27] E.E. Glickman, Metall. Mater. Trans. A 42A (2011) 250–266.

[28] E.E. Glickman, Zeitschrift Für Met. 96 (2005) 1204–1210.

[29] E.E. Glickman, Interface Sci. 11 (2003) 451–459.

[30] B. Joseph, M. Picat, F. Barbier, Eur. Phys. J. Appl. Phys. 5 (1999) 19–31.

[31] H. Kang, L. Cho, C. Lee, B.C. De Cooman, Metall. Mater. Trans. A Phys. Metall. Mater. Sci. 47 (2016) 2885–2905.

[32] M.H. Razmpoosh, A. Macwan, F. Goodwin, E. Biro, Y. Zhou, Metall. Mater. Trans. A

Phys. Metall. Mater. Sci. 51 (2020) 3938–3944.

[33] S.P. Murugan, J.B. Jeon, C. Ji, Y. Do Park, Weld. World 64 (2020) 1957–1969.

[34] M.A. Krishtal, Sov. Phys. Dokl. (1970).

[35] M.H. Razmpoosh, B. Langelier, E. Marzbanrad, H.S. Zurob, N. Zhou, E. Biro, Acta Mater. 204 (2021) 116519.

[36] C. Beal, X. Kleber, D. Fabregue, M. Bouzekri, Mater. Sci. Forum 706–709 (2012) 2041–2046.

[37] H. Lee, M.C. Jo, S.S. Sohn, S.H. Kim, T. Song, S.K. Kim, H.S. Kim, N.J. Kim, S. Lee, Mater. Charact. 147 (2019) 233–241.

[38] M.H. Razmpoosh, E. Biro, D.L. Chen, F. Goodwin, Y. Zhou, Mater. Charact. 145 (2018) 627–633.

[39] Z. Ling, M. Wang, L. Kong, K. Chen, Mater. Des. 195 (2020) 109055.

[40] C. Beal, Insa Lyon (2012).

[41] H. Kang, L. Cho, C. Lee, B.C. De Cooman, Metall. Mater. Trans. A 47 (2016) 2885–2905.

[42] C. Beal, X. Kleber, D. Fabregue, M. Bouzekri, Mater. Sci. Forum 706 (2012) 2041–2046.

[43] D. Bhattacharya, L. Cho, H. Ghassemi-armaki, E. Van Der Aa, A. Pichler, K.O. Findley, J.G. Speer, in: Sheet Met. Weld. Conf., 2018, pp. 1–10.

[44] C. Beal, (2011).

[45] H.H. Farrell, G.H. Gilmer, M. Suenaga, J. Appl. Phys. 45 (1974) 4025–4035.

[46] V. Janik, Y. Lan, P. Beentjes, D. Norman, G. Hensen, S. Sridhar, Metall. Mater. Trans. A Phys. Metall. Mater. Sci. 47 (2016) 400–411.

[47] J.E. Burke, in: Fifty-Seventh Annu. Meet. Am. Ceram. Soc., Cincinnati, Ohio, 1957, pp. 39–52.

[48] Y. Zhou, T.H. North, Acta Mater. 42 (1994) 1025–1029.

[49] J.C. Fisher, J. Appl. Phys. 22 (1951) 74–77.

[50] A. Fick, Philos. Mag. 10 (1855) 30–39.

[51] R.T.P. Whipple, London, Edinburgh, Dublin Philos. Mag. J. Sci. 45 (1954) 1225–1236.

[52] T. Suzuoka, Trans. JIM 2 (1961).

[53] L.G. Harrison, Trans. Faraday Soc. 57 (1961) 1191–1199.

[54] J. Crank, The Mathematics of Diffusion, Second, Oxford University Press, 1975.

[55] L. Benabou, Model. Simul. Mater. Sci. Eng. 27 (2019).

[56] E. Rabkin, Multiscale Phenomena in Plasticity, Springer, 2000.

[57] P. Shewmon, Diffusion in Solids, Springer, 2016.

[58] C. Herring, J. Appl. Phys. 21 (1950) 437–445.

[59] D. Bika, C.J. McMahon, Acta Metall. Mater. 43 (1995) 1909–1916.

[60] H. Gao, L. Zhang, W.D. Nix, C. V. Thompson, E. Arzt, Acta Mater. 47 (1999) 2865–2878.

[61] D. Bhattacharya, Mater. Sci. Technol. (United Kingdom) 34 (2018) 1809–1829.

[62] E. Biro, J.R. McDermid, J.D. Embury, Y. Zhou, Metall. Mater. Trans. A Phys. Metall.

Mater. Sci. 41 (2010) 2348–2356.

[63] V.H. Baltazar Hernandez, S.K. Panda, Y. Okita, N.Y. Zhou, J. Mater. Sci. 45 (2010) 1638–1647.

[64] B. Joseph, F. Barbier, G. Dagoury, M. Aucouturier, Scr. Mater. (1998).

[65] K. Ina, H. Koizumi, Mater. Sci. Eng. A (2004).

[66] L. He, C. DiGiovanni, X. Han, C. Mehling, E. Wintjes, E. Biro, N.Y. Zhou, Sci. Technol. Weld. Join. (2019).

[67] Y.G. Kim, I.J. Kim, J.S. Kim, Y. Il Chung, D.Y. Choi, Mater. Trans. 55 (2014) 171–175.

[68] D.R. Sigler, J.G. Schroth, W. Yang, X.Q. Gayden, C. Jiang, Y. Sang, P.J. Morin, in: Sheet Met. Weld. Conf. XIII, 2008.

[69] D.Y. Choi, A. Sharma, S.H. Uhm, J.P. Jung, Met. Mater. Int. (2018).

[70] C. DiGiovanni, E. Biro, N. Zhou, Sci. Technol. Weld. Join. (2018).

[71] D.-Y. Choi, S.-H. Uhm, C.M. Enloe, H. Lee, G. Kim, C. Horvath, in: Mater. Sci. Technol., 2017, pp. 454–462.

[72] R. Ashiri, M.A. Haque, C.W. Ji, M. Shamanian, H.R. Salimijazi, Y. Do Park, Scr. Mater. 109 (2015) 6–10.

[73] E. Wintjes, C. DiGiovanni, L. He, S. Bag, F. Goodwin, E. Biro, Y. Zhou, J. Manuf. Sci. Eng. 141 (2019) 1–9.

[74] C. DiGiovanni, S. Bag, C. Mehling, K.W. Choi, A. Macwan, E. Biro, N.Y. Zhou, Weld. World 63 (2019) 1583–1591.

[75] D.Y. Choi, A. Sharma, S.H. Uhm, J.P. Jung, Met. Mater. Int. 25 (2019) 219–228.

[76] C. Böhne, G. Meschut, M. Biegler, J. Frei, M. Rethmeier, Sci. Technol. Weld. Join. 0 (2019) 1–8.

[77] D.-Y. Choi, A. Sharma, J.P. Jung, Sheet Met. Weld. Conf. XVIII (2018) 1–9.

[78] J. Barthelmie, A. Schram, V. Wesling, IOP Conf. Ser. Mater. Sci. Eng. 118 (2016).

[79] S. Murugan, K. Mahmud, Y.-D. Park, in: Int. Insititute Weld. Annu. Meet., Bali, Indonesia, 2018, pp. III-1876–18.

[80] Y. Benlatreche, M. Duchet, T. Dupuy, G. Cornette, in: 5th Int. Conf. Steels Cars Truck., Amsterdam, 2017.

[81] C. Jiang, a. K. Thompson, M.F. Shi, S. Agashe, J. Zhang, H. Zhang, AWS Prof. Progr. (2003) 9A.

[82] Y. Benlatreche, H. Ghassemi-Armaki, M. Duchet, T. Dupuy, D. Cornette, G. Carollo, P. Dietsch, Int. Automot. Body Congr. (2017).

[83] P. Marashi, M. Pouranvari, S.M.H. Sanaee, A. Abedi, S.H. Abootalebi, M. Goodarzi, Mater. Sci. Technol. 24 (2008) 1506–1512.

[84] H. Zhang, X. Qiu, F. Xing, J. Bai, J. Chen, Mater. Des. 55 (2014) 366–372.

[85] P. Russo Spena, M. De Maddis, G. D'Antonio, F. Lombardi, Metals (Basel). 6 (2016) 270.

[86] M.I. Khan, M.L. Kuntz, Y. Zhou, Sci. Technol. Weld. Join. 13 (2008) 294–304.

[87] Y.J. Chao, J. Eng. Mater. Technol. 125 (2003) 125.

[88] Y.J. Chao, Sci. Technol. Weld. Join. 8 (2003) 62–68.

[89] M. Pouranvari, Mater. Sci. Technol. (United Kingdom) 33 (2017) 1705–1712.

[90] Y. Benlatreche, H. Ghassemi-Armaki, M. Duchet, T. Dupuy, G. Cornette, P. Dietsch, in: Int. Automot. Body Congr. (IABC 2017 Dearborn), 2017, pp. 9–18.

[91] American Welding Society, (2012) 1–107.

[92] L. Boriwal, R.M. Sarviya, M.M. Mahapatra, Mater. Today Proc. 4 (2017) 3672–3677.

[93] C. DiGiovanni, L. He, C. Hawkins, N.Y. Zhou, E. Biro, SN Appl. Sci. 3 (2021).

[94] M. Zhou, S. Hu, H. Zhang, Weld. J. 78 (1999) 305S-313S.

[95] K. Seo, J. Kim, H. Lee, J.H. Kim, B. Kim, (2017) 1–13.

[96] N. Moës, J. Dolbow, T. Belytschko, Int. J. Numer. Methods Eng. 46 (1999) 131–150.

[97] R. Ashiri, M. Shamanian, H.R. Salimijazi, M.A. Haque, C.W. Ji, Y. Do Park, Scr. Mater. 112 (2016) 156.

[98] L. Cho, H. Kang, C. Lee, B.C. De Cooman, Scr. Mater. 90 (2014) 25–28.

[99] D. Choi, A. Sharma, J.P. Jung, in: Sheet Met. Weld. Conf. XVIII, American Welding Society, Livonia, MI, 2018, pp. 1–9.

[100] C. Böhne, G. Meschut, M. Biegler, M. Rethmeier, Sci. Technol. Weld. Join. 0 (2020) 1–8.

[101] R. Sierlinger, M. Gruber, A Cracking Good Story of Liquid Metal Embrittlement during Spot Welding of Advanced High Strength Steels, 2016.

[102] E. Wintjes, C. DiGiovanni, L. He, E. Biro, N.Y. Zhou, Weld. World Submitted (n.d.).

[103] Auto/Steel Partnership, (2014) 1.

[104] D.W. Dickinson, J.E. Frankling, A. Stanya, Weld. J. (1980).

[105] A. Wang, J. Zhao, Sci. China Technol. Sci. 53 (2010) 1798–1808.

[106] R. Ashiri, M. Shamanian, H. Reza, A. Haque, J. Bae, C. Ji, K. Chin, Y. Park, Scr. Mater. 114 (2016) 41–47.

[107] T. Furuhara, K. Kobayashi, T. Maki, ISIJ Int. 44 (2004) 1937–1944.

[108] G. Jung, Liquid Metal Embrittlement of High Mn TWIP Steel, Pohang University of Science and Technology, 2015.

[109] Z. Ling, T. Chen, L. Kong, M. Wang, H. Pan, M. Lei, Metall. Mater. Trans. A 50 (2019) 5128–5142.

[110] C. Mesplont, J.Z. Zhao, S. Vandeputte, B.C. De Cooman, Mater. Technol. 72 (2001) 263–270.

[111] C. Beal, X. Kleber, D. Fabregue, M. Bouzekri, Scr. Mater. 66 (2012) 1030–1033.

[112] J.S. Dohie, J.R. Cahoon, W.F. Caley, J. Phase Equilibria Diffus. 28 (2007) 322–327.

[113] J. Noye, in: J. Noye (Ed.), Conf. Numer. Solut. Partial Differ. Equations, North-Holland Publishing Company, Melbourne, 1981, pp. 9–35.

[114] J. Frei, M. Rethmeier, Weld. World 62 (2018) 1031–1037.

[115] M.H. Razmpoosh, A. Macwan, E. Biro, D.L. Chen, Y. Peng, F. Goodwin, Y. Zhou, Mater. Des. 155 (2018) 375–383.

[116] M.H. Razmpoosh, A. Macwan, F. Goodwin, E. Biro, Y. Zhou, Materialia 11 (2020).

[117] M. Jurisch, PhD Dissertation, Freiberg (Sachsen), 1969.

[118] I. Herbeuval, M. Biscondi, C. Goux, Mem Sci Rev Met. 70 (1973) 39–46.

[119] W. Gust, S. Mayer, A. Bogel, B. Predel, J. Phys. Colloq. 46 (1985) C4-537-C5-544.

[120] N. Shajan, K.S. Arora, M. Shome, P. Singh, V. Santhanagopalan, Sci. Technol. Weld. Join. (2020).

[121] V. Borisov, V. Golikov, G. Shcherbedinskii, Phys. Met. Metallogr. 17 (1964) 881–885.

[122] V. Levitin, Phys. Met. Metallogr. 10 (1960) 294.

Appendices

Appendix A: Consistency Analysis of the Finite Difference Approximation for the Stress-assisted Grain Boundary Diffusion Equation

The finite difference equation Eq. 5-7 can be rewritten in the form:

$$c_{gb}{}_i^{j+1} = c_{gb}{}_{i-1}^{j}(f_c + f_s) + c_{gb}{}_{i+1}^{j}(f_c) + c_{gb}{}_i^{j}(1 - 2f_c - f_s) \qquad (A-1)$$

Where:

$$f_c = \frac{\Delta t D_b}{\Delta x^2}$$

$$f_s = \frac{\Delta t D_b \Omega \sigma_o Z'}{(kT)\Delta x}$$

Using the Taylor series expansion, Eq. A-1 can be rewritten as:

$$\begin{aligned}
&\left[c_{gb}{}_i^j + \Delta t \frac{\partial c_{gb}{}_i^j}{\partial t} + \frac{\Delta t^2}{2!}\frac{\partial^2 c_{gb}{}_i^j}{\partial t^2} + \cdots\right] \\
&\quad = (f_c + f_s)\left[c_{gb}{}_i^j - \Delta x \frac{\partial c_{gb}{}_i^j}{\partial x} + \frac{\Delta x^2}{2!}\frac{\partial^2 c_{gb}{}_i^j}{\partial x^2} - \frac{\Delta x^3}{3!}\frac{\partial^3 c_{gb}{}_i^j}{\partial x^3} + \cdots\right] \qquad (A-2) \\
&\quad + (fc)\left[c_{gb}{}_i^j + \Delta x \frac{\partial c_{gb}{}_i^j}{\partial x} + \frac{\Delta x^2}{2!}\frac{\partial^2 c_{gb}{}_i^j}{\partial x^2} + \frac{\Delta x^3}{3!}\frac{\partial^3 c_{gb}{}_i^j}{\partial x^3}\right] \\
&\quad + c_{gb}{}_i^j(1 - 2f_c - f_s)
\end{aligned}$$

Eq. A-2 simplifies to:

$$\left[{c_{gb}}_i^j + \Delta t\frac{\partial {c_{gb}}_i^j}{\partial t} + \frac{\Delta t^2}{2!}\frac{\partial^2 {c_{gb}}_i^j}{\partial t^2} + \cdots\right]$$

$$= f_s\left(-\Delta x\frac{\partial {c_{gb}}_i^j}{\partial x} + \frac{\Delta x^2}{2!}\frac{\partial^2 {c_{gb}}_i^j}{\partial x^2} - \frac{\Delta x^3}{3!}\frac{\partial^3 {c_{gb}}_i^j}{\partial x^3} + \cdots\right)$$

$$+ f_c\left(\frac{\Delta x^2}{2!}\frac{\partial^2 {c_{gb}}_i^j}{\partial x^2} + \frac{\Delta x^4}{4!}\frac{\partial^4 {c_{gb}}_i^j}{\partial x^4} + \cdots)\right) + {c_{gb}}_i^j$$

Therefore, the equation takes the form:

$$\frac{\partial {c_{gb}}_i^j}{\partial t} = D_b\frac{\partial^2 {c_{gb}}_i^j}{\partial y^2} - D_b\frac{\Omega\sigma_o}{kT}\frac{\partial^2 {c_{gb}}_i^j}{\partial y^2}Z' + E_i^j \qquad (A-3)$$

Where:

$$E_i^j = -\frac{\Delta t}{2}\frac{\partial {c_{gb}}_i^j}{\partial t} + f_c\frac{\Delta x^4}{12}\frac{\partial^4 {c_{gb}}_i^j}{\partial x^4} + f_s\frac{\Delta x^2}{2}\frac{\partial^2 {c_{gb}}_i^j}{\partial y^2} + O\{(\Delta t^2)(\Delta x^2)\}$$

Eq. 5-7 is therefore consistent with the stress-assisted grain boundary diffusion Eq. 5-6 since the truncation error $E_i^j \to 0$ as $\Delta t \to 0$ and $\Delta x \to 0$.

Appendix B: Stability Analysis of the Finite Difference Approximation for the Stress-assisted Grain Boundary Diffusion Equation

The finite difference equation Eq. 5-7 can be rewritten in the form:

$$c_{gb}{}_i^{j+1} = c_{gb}{}_{i-1}^{j}(f_c + f_s) + c_{gb}{}_{i+1}^{j}(f_c) + c_{gb}{}_i^{j}(1 - 2f_c - f_s) \qquad (B-1)$$

Where:

$$f_c = \frac{\Delta t D_b}{\Delta x^2}$$

$$f_s = \frac{\Delta t D_b \Omega \sigma_o Z'}{(kT)\Delta x}$$

According to the perturbation analysis outlined in [113] the initial set of round off errors at the first time level will propagate through the numerical values. New round off errors will be added to this error with each time step calculation if the numerical solution is not stable. It can be expected that after many times steps that errors at any time level will be approximately the same in magnitude, either having the same or an alternating sign along that time distribution [113]. Additionally, it has been shown for linear finite difference equations that the corresponding error terms satisfy the same homogenous finite difference equation as c_{gb} [113]. Therefore, if the error signs are the same along the time distribution it follows:

$$\varepsilon^{j+1} = \varepsilon(f_c + f_s) + \varepsilon(f_c) + \varepsilon(1 - 2f_c - f_s) \qquad (B-2)$$

$$\varepsilon^{j+1} = \varepsilon - 2f_s\varepsilon$$

$$\varepsilon^{j+1} = \varepsilon(1 - 2f_s)$$

In order for the error to not propagate and the finite difference equation to be stable:

$$|1 - 2f_s| < 1 \qquad (B-3)$$

Therefore, for stability of the finite difference equation requires:

$$\Delta t < \frac{\Delta x}{D_b \frac{\Omega\sigma_o}{kT} Z'_{max}} \qquad (B-4)$$

Applying the alternating error sign along the time distribution, it follows:

$$\varepsilon^{j+1} = -\varepsilon(f_c + f_s) + \varepsilon(f_c) - \varepsilon(1 - 2f_c - f_s) \qquad (B-5)$$

$$\varepsilon^{j+1} = -4f_c\varepsilon - 2f_s\varepsilon + \varepsilon$$

$$\varepsilon^{j+1} = \varepsilon(1 - 4f_c - 2f_s)$$

Similar to Eq. B-3, for the error to not propagate and the difference equation be stable:

$$|1 - 4f_c - 2f_s| < 1 \qquad (B-6)$$

Therefore, for stability the finite difference equation also requires:

$$\Delta t < \frac{\Delta x^2}{(2D_b + \Delta x \frac{\Omega\sigma_o}{kT} Z' D_b)} \qquad (B-7)$$

Given that Eq. B-7 is the more conservative of the limitations on Δt, that was the criteria used to determine the time step for calculation.